HYDROGEN STORAGE IN Ti-BASED COATINGS AND Ti6Al4V ALLOY

Sive Mazwi

A thesis submitted in partial fulfillment of the requirements for the degree of Magister Scientiae in the Department of Physics

University of the Western Cape

Supervisor: Dr Miroslava Topic

Co Supervisor(s): Dr Sylvain Halindintwali

Dr Schadrack Nsengiyumva

February 2016

Keywords

Hydrogen storage in Ti based coatings and Ti6Al4V alloy

Hydrogen

Hydrogen storage

Metal hydrides

Titanium

Palladium

Ti6Al4V alloy

Thin film coatings

Elastic recoil detection analysis

Rutherford Backscattering spectrometry

Phase transformation

Abstract

Hydrogen has been regarded as an ideal energy carrier for future, it can be stored as a liquid in cryogenic tanks, a gas in high pressure cylinders and as solid in metal hydrides. Hydrogen storage in metal hydrides is of research interest because hydrides often have high energy density than gas or liquid hydrogen and are relatively safe. Ti and Ti alloys are promising hydrogen storage material because they have high affinity for hydrogen, light in weight and react reversibly with hydrogen. This work aims to investigate the hydrogen storage capacity of CP- Ti and Ti6Al4V alloy and Pd/Ti6Al4V alloy, where Pd was deposited on Ti6Al4V alloy. Samples were hydrogenated from room temperature to 650 °C at atmospheric pressure in the vacuum furnace under the 15%H/Ar atmosphere.

Hydrogenation was carried out for a period of 3 hours for all samples. Sample composition and layer thickness were determined using Rutherford backscattering spectrometry. The microstructure and phase transformation were investigated using optical microscopy and X-ray diffraction technique. Hydrogen storage capacity was determined using elastic recoil detection analysis and gravimetric method. It was found that hydrogenation temperature has an effect on hydrogen absorption, microstructure and phase transformation. Maximum hydrogen concentration was obtained at hydrogenation temperatures of 550 °C for all materials with 45.57 at.% in CP-Ti, 34.77 at.% in Ti6Al4V alloy and 39 at.% H in Pd/Ti6Al4V coated system. In CP-Ti it was found that hydrogen absorption begins at 550 °C and decreases at hydrogenation temperature of 650 °C and that hydrogenation at both temperatures leads to formation of titanium hydrides and needle-like microstructure. At temperatures below 550 °C no hydrides were formed. For Ti6Al4V alloy ERDA results showed that no significant hydrogen absorption occurred at temperatures below 550 °C and at hydrogenation temperature of 650 °C, hydrogen absorption decreased drastically. The δ- titanium hydride was detected in the sample hydrogenated at 550 °C. Fine needle like microstructure was observed in the sample hydrogenated at 550 °C, and at higher temperature (650 °C) coarse needles were formed. Pd coatings on Ti6Al4V alloy was found to increase the absorption of hydrogen, and allowing hydrogen to be absorbed at low temperatures.

Dedication

This work is dedicated to the following people:

My mother Thea Ntombebhongo Siqoko, my late grandmother Irene Nontsikelelo Siqoko, my later uncle Vuyani Eric Siqoko and my siblings.

Declaration

I declare that

Hydrogen storage in Ti based coatings and Ti6Al4V alloy

is my own work, that it has not been submitted for any degree or examination in any other university, and that all the sources I have used or quoted have been indicated and acknowledged by complete references.

UNIVERSITY *of the*
WESTERN CAPE

Sive Mazwi   **February 2016**

Signature : ....

Acknowledgments

First and foremost I would like to thank God for giving me strength to do this project and for his guidance throughout my life.

I would like to thanks the following people for their contribution in this work, this thesis would not have been possible without them:

My supervisor, Dr Miroslava Topic (Material Research Deaprtment, iThemba LABS) for the opportunity to carry out this project, and for her tireless effort, patience, support, critical comments and guidance during this project.

Dr Sylvain Halindintwali (Department of Physics, University of the Western Cape) my co-supervisor for support, suggestions, corrections, and assistance with ERDA and RBS analysis.

Dr Schadrack Nsengiyumva (Department of Physics, Rhodes University) also my co-supervisor, for support, and corrections of this thesis.

Students and staff of Material Research Department at iThemba LABS for support and encouragement during the course of this study.

The staff of the Physics Department, University of the Western Cape, for their support.

The center for Materials Engineering at University of Cape Town for giving me the opportunity to perform hydrogenation experiments and sample preparation using their facilities.

Miss Velile Vilane (Center for Materials Engineering, UCT) for her assistance with hydrogenation experiments.

Abbreviations

Elastic recoil detection analysis : ERDA

Rutherford backscattering spectrometry: RBS

Commercially pure Titanium : CP-Ti

Palladium: Pd

Platinum: Pt

Silicon: Si

X-ray diffraction: XRD

High resolution scanning electron microscopy: HRSEM

Hydrogen: H

List of Tables

List of figures

Contents

Chapter 1

Introduction

1.1 Background

Energy is one of the most important aspects of our daily lives. As the world population continues to grow, there is a high demand for energy. Since the year 2012, the annual gross production of electricity reached approximately 22,2000 Tw h. Global society has become highly dependent on the use of fossil fuels to produce energy, fossil fuels contribute to around 70% of global electricity generation [1.1]. The problem with depending on fossil fuels is that, they are depleting rapidly. Fossil fuel reserves that are presently available can support a maximum of 40 years for petroleum, 60 years for natural gas and 156 years for coal [1.2]. It is expected that these fuels will become unavailable and expensive in the near future. Fossil fuel depletion and increase in energy consumption threatens the energy and economic security problem worldwide. In addition, fossil fuels are not environmentally friendly. Combustion of fossil fuels generate carbon dioxide which is the major contributor to global warming [1.3]. Global warming is a critical issues worldwide. In 2009 (Figure 1.1) approximately 30 billion tons of carbon dioxide were generated from fossil fuels, this number is twice that of CO_2 generated in 1971. The worldwide carbon dioxide emission needs to be reduced. To achieve the target of reducing CO_2, an environmentally clean and more sustainable energy source as an alternative to fossil fuels is needed.
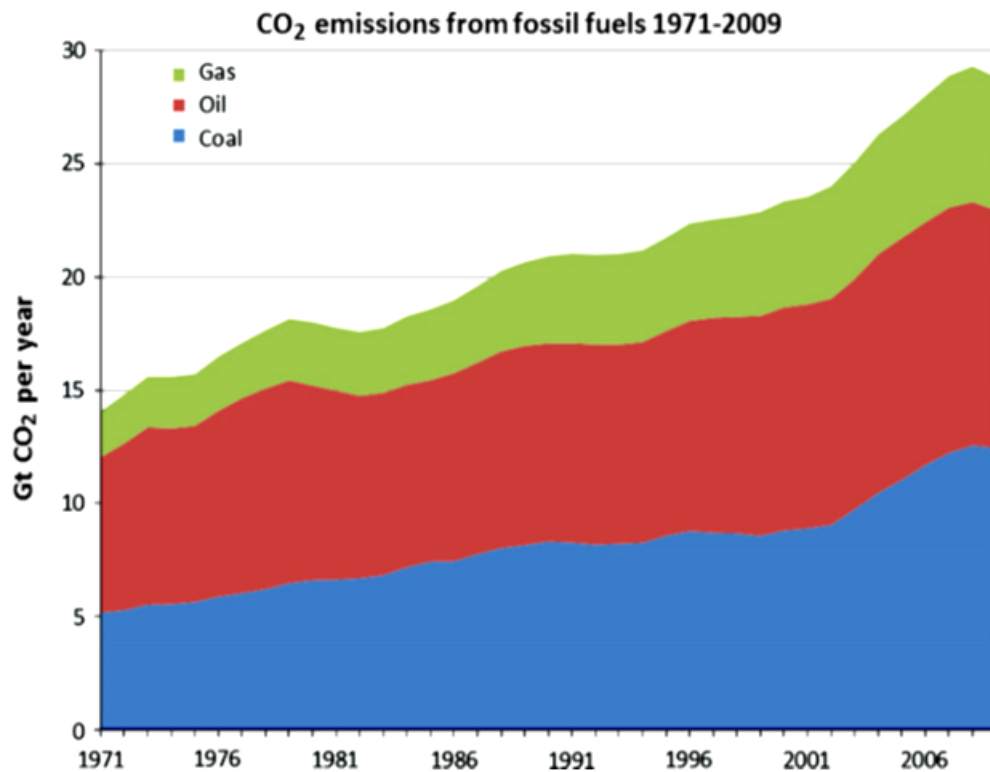
Figure 1.1: Carbon dioxide emission from fossil fuels: [1.4].

Hydrogen energy was proposed over 4 decades ago as a solution to the interrelated global problems of depletion of fossil fuels and environmental problems [1.5]. Hydrogen is an ideal energy carrier due to the following reasons:

1. It is the most abundant element in the universe (makes up more than 90% of all atoms).

2. It is environmentally compatible. Water vapor is the only byproduct that results from combustion of hydrogen unlike fossils fuels which generate carbon dioxide.

3. As a fuel of choice, it has high chemical energy per unit mass (39.4 kWh/kg) as compared to other fuels. For example its energy density is three times greater than that of liquid hydrocarbons (13.1 kWh/kg) [1.6].

4. Hydrogen is a renewable energy source, a diagram of how hydrogen cycle might look like is shown in Figure 1.2. Energy from sunlight is converted into electricity by photovoltaic cells, this electricity is then used to dissociate water into hydrogen and oxygen. Hydrogen is then stored and distributed. Lastly hydrogen with oxygen is combusted to form water and energy is released as water vapor is released into the atmosphere.

2
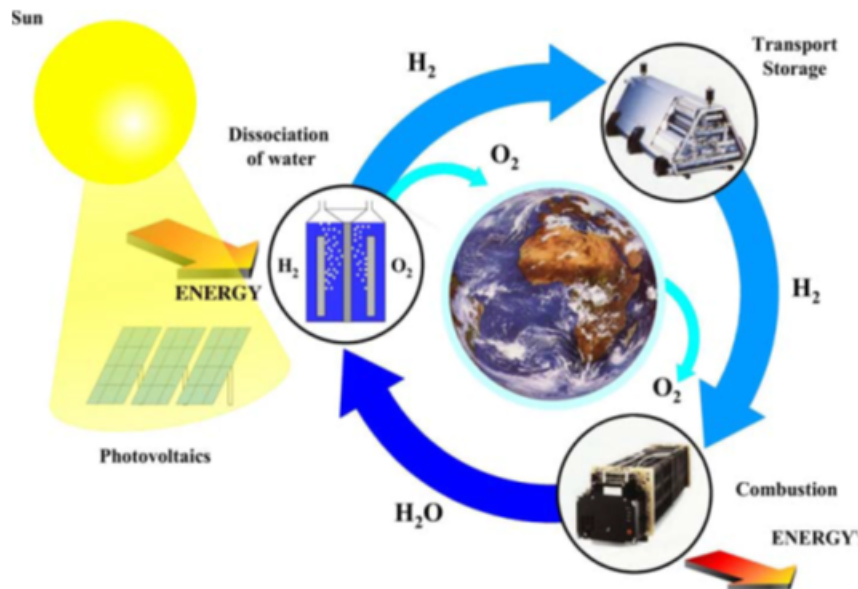
Figure 1.2: Hydrogen cycle: hydrogen is produced from water by electricity, then stored and distributed and finally combusted with oxygen to form water [1.6].

Even though hydrogen is one of the most abundant element it is not available in free form; it must be produced from other molecules containing hydrogen such as water and natural gas. After production it must be stored. Hydrogen storage is one of the key challenges in realizing hydrogen economy. As an ideal energy carrier hydrogen needs to be stored safely and effectively. This project will focus on the storage of hydrogen. Formulation of a safe, economical and efficient hydrogen storage method is a big challenge.

1.2   Hydrogen storage overview

Hydrogen molecule H_2 can be found in liquid, solid, or gaseous form depending on temperature and pressure as shown in phase diagram in Figure 1.3

Hydrogen is a solid at low temperatures less than the melting temperature $(-259\,°C)$ with density of 70.6 kg/m^3, and hydrogen is a gas at high temperatures with a density of 0.09 kg/m^3 at $0\,°C$ and pressure of 1 bar. Hydrogen is a liquid in the region from triple point to critical point with density of 70.8 kg/m^3 at $-253\,°C$. At room temperature (298 K) hydrogen gas can be described

3
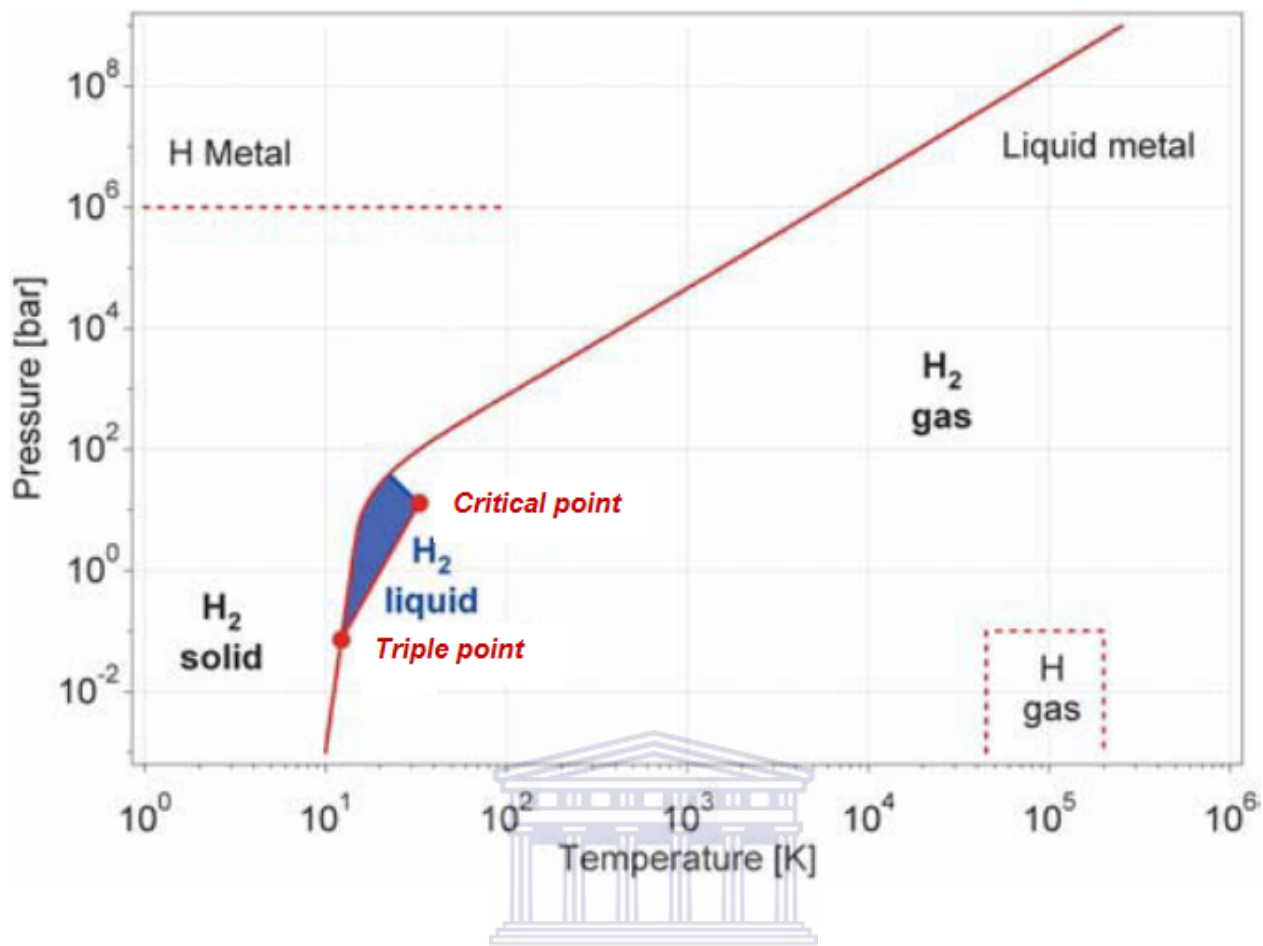
Figure 1.3: Pressure-Temperature phase diagram for hydrogen [1.6].

by Van der Waals equation.

$$P(V) = \frac{nRT}{V - nb} - a\frac{n^2}{V^2} \tag{1.1}$$

where P is the gas pressure, V is the volume, T is the absolute temperature, n is the number of moles, R is the gas constant, a is the dipole interaction or repulsion constant and b is the volume occupied by the hydrogen molecule.

1.2.1 Hydrogen storage methods

Even though hydrogen is an attractive alternative to fossil fuels, its storage is a challenging task because it has low density by volume ($0.09 \, \text{kg/m}^3$) in gaseous state and low boiling point ($-253\,°\text{C}$). To increase the density hydrogen can be either be compressed to high pressures, liquefied at cryogenic temperatures or stored as a solid in metal hydrides [1.7].

4

High pressure gas cylinders

Since 1880's hydrogen has been stored as a compressed gas high pressure cylinders [1.5]. This is the simplest and most commonly used method. In these cylinders hydrogen is usually compressed to pressures ranging from 200 up to 800 bar. A volumetric density of 26.3 kg/m^3 and gravimetric density of 5.5 wt % can be reached when hydrogen is compressed at pressure of 700 bar. At this pressure, the volumetric density remains lower than that of other methods. Low volumetric density and safety problems associated with the use of high pressure tanks limits the use of this method [1.8, 1.9].

Liquid hydrogen

Hydrogen volumetric density can be increased by liquefying it. Volumetric density of liquid hydrogen is 70.8 kg/m^3, it is higher than that of compressed hydrogen gas [1.6]. Volumetric density of hydrogen can be increased from 2.5 MJ/L for liquid hydrogen to 8 MJ/L for compressed hydrogen at pressures of 700 bar. Two major concerns in this method are the efficiency of liquefaction process and the boil-off of the liquid. Hydrogen does not liquify until a temperature of $-253\,°C$ is reached, so a large amount of energy is required for liquifaction process. In this storage method at least 35% of the fuel energy content is used during the liquefaction process [1.8,1.9]. Heat flowing from environment leads to evaporation of hydrogen and liquid hydrogen evaporates quickly during delivery and refueling. Moreover the cost of cryogenic tanks is high. The relatively large amount of energy necessary for liquefaction and the continuous boil-off of liquid limit the hydrogen storage efficiency using the liquefaction method.

Metal hydrides

Hydrogen is a high reactive element, it reacts with most metals and metal alloy and form metal hydrides. The electropositive elements such as lanthanides, actinides and members of titanium and vanadium group are the most reactive elements that readily form hydrides. Hydrides are classified according to the nature of the bonding of hydrogen to the host lattice. They fall into four different categories: covalent, saline, ionic and metallic. This classification is not always descriptive, for example rare earth metals are usually classified as metallic but also exhibit some characteristics similar to those of saline hydrides such as high heat formation. Metallic hydrides have high thermal conductivity, high electrical resistivity and unlike metals they are usually brittle [1.10]. TiH$_2$ is an example of a metallic hydride.

Intermetallic hydrides can also be formed. Intermetallic compounds consist of more than one metal, for example $LaNi_5$ and FeTi. They are usually designed by alloying a metal that easily form a stable hydride with another element which does not form a stable hydride. Intermetallic hydrides can absorb and desorbs hydrogen at ambient temperature and pressure. Table 1.1 shows several families of intermetallic hydrides that are interesting for hydrogen storage, where A represents an element with high affinity A, and element B with low hydrogen affinity.

Intermetallic compounds	Prototype
AB_5	LaN_5
AB_2	ZrV_2 , $ZrMn_2$, $TiMn_2$
AB_3	$CeNi_3$, YFe_3
A_2B_7	Y_2Ni_7, Th_2Fe_7
A_6B_{23}	Y_6Fe_{23}
AB	TiFe, ZrN i
A_2B	Mg_2Ni, Ti_2Ni

Table 1.1: Intermetallic compounds for hydrogen storage [1.11].

Intermetallic hydrides have high volumetric capacity but the main drawback is that most of them have low gravimetric capacity, limited to less than 3 wt%. The gravimetric and volumetric density of some of the metal and intermetallic hydrides is shown in Figure 1.4. $LaNi_5H_6$ is one of the few hydrides that is commercially available with a volumetric capacity of 5.5×10^{22} atoms/cm^3 and a low gravimetric capacity of 1.37 wt%.
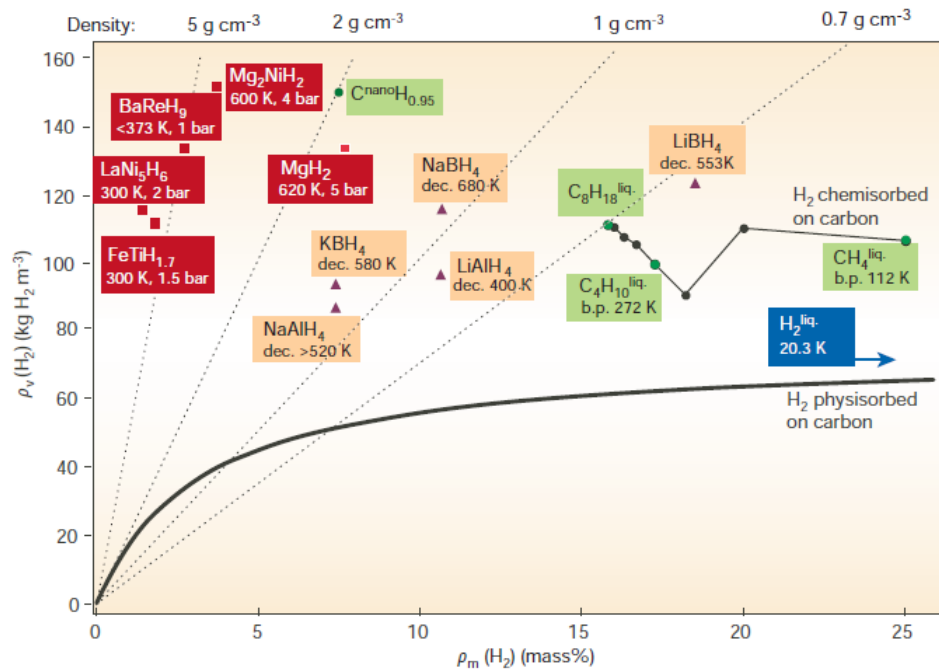
Figure 1.4: Volumetric and gravimetric concentration of metal hydrides [1.12].

Metal hydrides are a promising way to safely and efficiently store hydrogen. Hydrogen energy density in metal hydrides is often higher than the density in its liquid or gas phase [1.13,1.14].

1.3   Aim and Objectives

Metal hydrides are a key enabling technology for the extensive use of hydrogen as an ideal energy carrier. Ti and Ti6Al4V alloy have been considered as potential hydrogen storage materials. The investigation of hydrogen storage capacity in CP-Ti, Ti6Al4V alloy and Pd/Ti6Al4V alloy is of our main focus in this project. The objectives of this research are to:

1. Investigate the effect of temperature on hydrogen absorption in CP-Ti, Ti6Al4V alloy and Pd coated Ti6Al4V.

2. Investigate the effect of hydrogen on phase transformation and microstructural evolution of hydrogenated CP-Ti and Ti6Al4V alloy.

3. Study the effect of Pd coatings on hydrogen absorption in Ti6Al4V alloy at different hydrogenation temperatures.

1.4   Scope of the work

CP-Ti and Ti6Al4V alloy and Pd coated Ti alloys were used in this study. These materials were hydrogenated at different temperatures and atmospheric pressure under 15% H/Ar atmosphere. Hydrogen concentration was determined using elastic recoil detection analysis and gravimetric method. The microstructure, morphology and phase transformation were investigated using optical microscopy, scanning electron microscopy and X-ray diffraction technique, respectively. Surface composition and film thickness were investigated using Rutherford backscattering spectroscopy.

1.5   Thesis outline

This thesis consists of five chapters. Chapter 2 describes the properties of Ti and Ti6Al4V alloy, followed by fundamentals of hydrogen absorption in metals with the main emphasis on Ti and its alloys. Sample description, preparation, thin film deposition and hydrogenation process are given in chapter 3. Theory on analytical techniques and measurement details used in this study are given in chapter 3. The results obtained are presented and discussed in chapter 4. Conclusions and recommendations are presented in chapter 5.
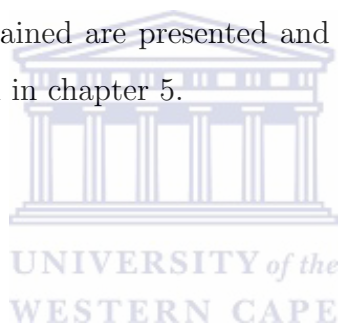
References

[1.1] X, Luo, J. Wang, M. Dooner, and J. Clarke, Overview of current development in electrical energy storage technologies and the application potential in power system operation, *Applied Energy*, **137**, 511-536 (2015).

[1.2] A. Midilli, M. Ay, I. Dincer, and M.A. Rosen, Hydrogen and hydrogen energy strategies I: current status and needs, *Renewable and Sustainable Energy Reviews*, **9**, 255-271 (2005).

[1.3] L. Chiari, A. Zecca, Constraints of fossil fuels depletion on global warming projections, *Energy Policy*, **39**, 5026-5034 (2011).

[1.4] M. Hook, X. Tang, Depletion of fossil fuels and anthropogenic climate change—A review, *Energy Policy*, **52**, 797–809 (2003).

[1.5] S.A. Sherif, Y.D. Goswami, E.K. Stefanakos, A. Steinfeld, editors, *Handbook of hydrogen energy*, Taylor and Francis Group (2014).

[1.6] A. Zuttel, Hydrogen storage and distribution systems, *Mitigation and Adaptation Strategies for Global Change*, **12**, 243- 365 (2007).

[1.7] U. Eberle, M. Felderhoff, F. Schuth, Chemical and Physical Solutions for Hydrogen Storage, *Angewandte Chemie-International Edition*, **48**, 6608-6630 (2009).

[1.8] B.P. Tarasov, M.V. Lototskii, V.A.Yartysc, Problem of Hydrogen Storage and Prospective Uses of Hydrides for Hydrogen Accumulation, *Russian Journal of General Chemistry*, **77**, 649 - 711 (2007).

[1.9] D.J. Durbin, C. Malardier-Jugroot, Review of hydrogen storage techniques for on board vehicle applications, *International Journal of Hydrogen Energy*, **38**, 14595 - 14617 (2013).

[1.10] W.M. Mueller, J.P. Blackledge, G.G. Libowitz, editors, *Metal hydrides*, Academic Press (1968).

[1.11] A. Zuttel, Materials for hydrogen storage, *Materials today*, **6**, 24- 33 (2003).

[1.12] L. Schlapbach, A. Züttel, Hydrogen-storage materials for mobile applications, *Nature*, **414**, 353-358 (2001).

[1.13] I.P. Jain and Y.K. Vijay, L.K. Malhotra, K.S.Uppadhyay, Hydrogen storage in thin film metal hydride-a review, *International Journal of Hydrogen Energy*, **13**, 15-23 (1988).

[1.14] J. Yang, A. Sudik, C. Wolvertonb, D.J. Siegelwa, High capacity hydrogen storage materials: attributes for automotive applications and techniques for materials discovery, *Chemical Society Reviews*, **39**, 656-675 (2010).

Chapter 2

Literature Review

2.1 Hydrogen absorption in metals

2.1.1 Hydrogen absorption process

Hydrogen reacts with most metals and form metal hydrides. The reaction of hydrogen with most metals is reversible and can be described by the following reaction

$$Me + \frac{x}{2}H_2 \leftrightarrow MeH_x + Q \tag{2.1}$$

where Me is a metal, a solid solution or an intermetallic compound, MeH_x is the hydride and x the ratio of hydrogen to metal, Q is the heat reaction [2.1]. Hydrogen can be introduced into the metal by using molecular hydrogen gas or implantation of hydrogen atoms [2.2]. If a metal is hydrogenated using hydrogen gas, several reactions must take place in order for hydrogen to diffuse in the metal and forms a hydride. Hydrogen absorption process can be explained by one dimensional curve shown in Figure 2.1. Firstly hydrogen molecule is adsorbed into the surface of the metal by the weak van der Waals forces, leading to a physisorption state. Energy for physisorption is of the order E = 6 kJ/mol H_2. Closer to the surface hydrogen has to overcome activation barrier for dissociation of hydrogen molecules into two hydrogen atoms and then chemical bonding of hydrogen with the surface (chemisorption). Chemisorption energy is typically in the range of E = 20 - 150 kJ/mol H_2. After chemisorption hydrogen atoms may diffuse into a bulk in an endothermic or exothermic process and form a solid solution, the α- phase. With increase of hydrogen concentration nucleation and growth of metal hydride phase occurs. The hydrogen atoms occupy interstitial sites (octahedral or tetrahedral sites) in a metal, the interstitial hydrogen atoms contribute with their electrons to the band structure of the metal.

11
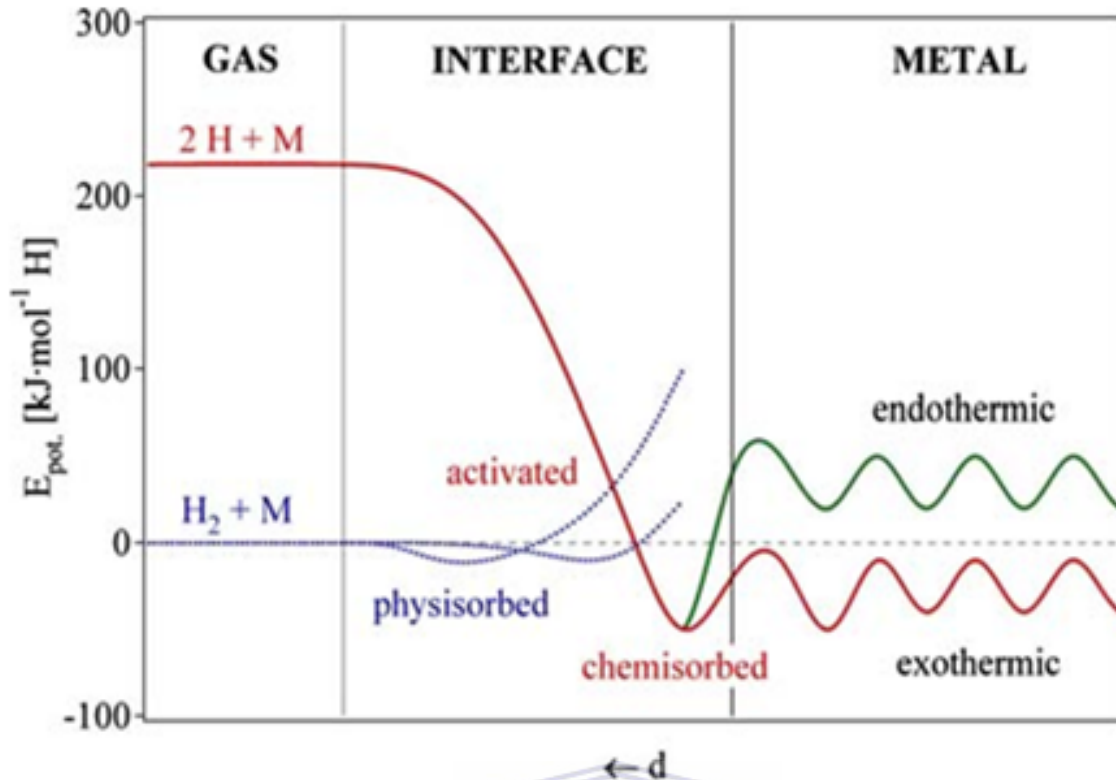
Figure 2.1: One dimensional curve: Hydrogen absorption process [2.3,2.4].

2.1.2 Thermodynamics in metal-hydrogen system

Thermodynamics properties of the metal-hydrogen system from gaseous hydrogen is described by means of pressure-composition isotherms presented in Figure 2.2. At low hydrogen concentration the hydrogen atom diffuse into the metal host lattice and form a solid solution of hydrogen. As the hydrogen pressure increases the concentration of hydrogen also increases. At greater hydrogen concentration in the metal lattice a strong H-H interaction caused by lattice expansion becomes significant and hydride phase starts to form. The α-phase represents the solution of hydrogen in the metal phase, which has the same structure the host metal [2.5]. The β-phase represents the solution of hydrogen in hydride phase. The region where the α and β-phase coexist shows a flat plateau. As the temperature is increased the plateau pressure increases, thus reducing the length of plateau. Above critical temperature T_c the α-phase transforms continuously into a β- phase. For hydrogen storage application the length and slope of plateau are of great importance; the length of plateau determines reversible hydrogen storage capacity of a metal hydride [2.6]. The change in enthalpy is used to measure the metal-hydrogen bond strength. Entropy change ΔS is the same for all metal hydrides with a value of -130J/K mol H_2.

The equilibrium pressure as a function of temperature is related to the enthalpy H and entropy S by Van't Hoff equation:

$$\ln\frac{P(H_2)}{P^0} = \frac{\Delta H}{RT} - \frac{\Delta S}{R} \tag{2.2}$$

where $P(H_2)$ is the equilibrium pressure, P^0 is the standard pressure, ΔH is the enthalpy change, ΔS is the entropy change, T is the absolute temperature and R is the gas constant.

Van't Hoff plot (ln P vs 1/T) is used to represent the stability of a metal hydride according to equation 2.2. For every temperature T, the plateau pressure reflects one point on Van't Hoff plot (Figure 2.2 b). Pressure vs reciprocal temperature is linear to negative slope and is related to heat of reflection.
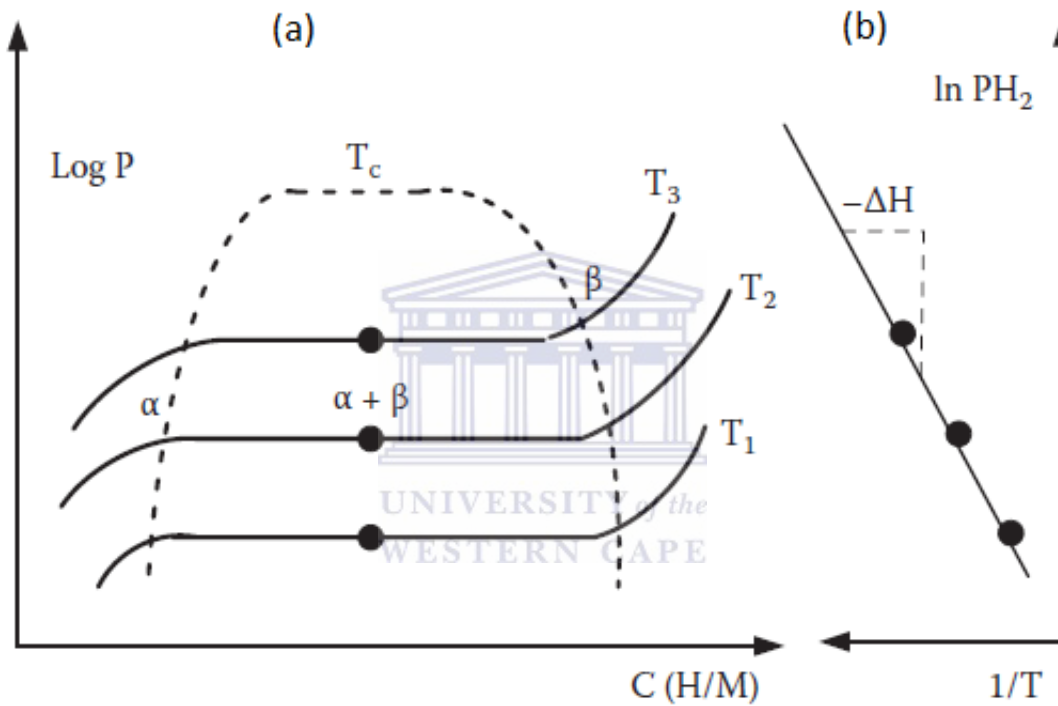
Figure 2.2: (a) Pressure composition isotherms for the hydrogen absorption in a metal on the left-hand side and (b) Van't Hoff plot [2.6].

2.2 Hydrogen absorption in Ti and Titanium alloy

Titanium is the fourth most abundant structural metal following Al, Fe and Mg [2.7]. It has an atomic number 22, a low density of 4.5 g/cm^3 and a molar mass of 47.87 g/mol. Ti and Titanium alloy have high strength to weight ratio and good corrosion resistance, as a result they are widely used in areas such as aerospace industry, automobiles and medical engineering [2.8]. Commercially pure (CP) titanium has a hexagonal close packed (hcp) structure, the α-phase stable at room temperature. At temperatures higher than 883 °C pure titanium transforms into body centered cubic (bcc) structure, the β-phase. Ti6Al4V alloy has two phases, the α and β-phases. It consists of 6% of aluminum (α stabilizing element) and 4% of vanadium (β stabilizing element). The atomic unit cell of the α-Ti phase is shown in Figure 2.3 (a) with three mostly densely packed planes, basal plane (0002), prismatic plane (10$\bar{1}$0) and pyramidal plane ($\bar{1}$011). The crystal structure of the β-phase is shown in Figure 2.3 (b) with lattice parameter a = 0.322 nm.
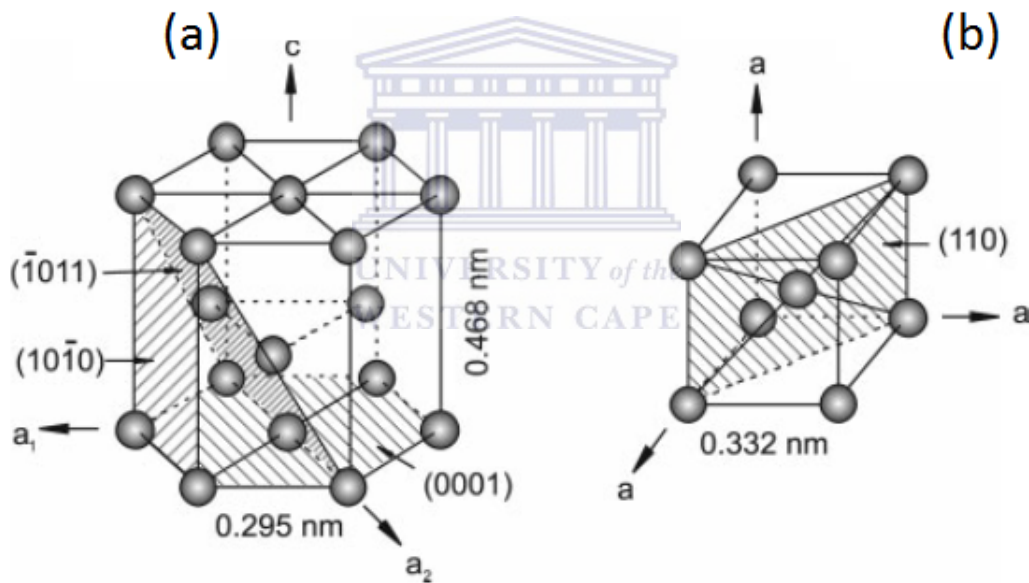
Figure 2.3: (a) α-hcp crystal structure (b) β-bcc crystal structure [2.8].

Titanium and its alloy have high affinity for hydrogen and react reversibly with hydrogen and form metal hydrides. The low molecular weight and high affinity for hydrogen make titanium and its alloy a unique hydrogen storage material [2.9- 2.12]. Ti and Ti alloy can absorb up to 50 at.% of hydrogen at 500 °C, and even higher hydrogen amount can be absorbed at lower temperatures [2.13]. The solubility of hydrogen in Ti depends on hydrogenation experimental parameters

such as temperature, time, pressure and gas concentration. Hydrogen dissolves easily in Ti at temperatures above 500 °C [2.14]. Lopez- Suarez et al. [2.9] found that hydrogen was not absorbed in Ti and Ti6Al4V alloy until temperature of 500 °C was reached. Gas concentration in the system also plays an important role in the amount of hydrogen that a metal can absorb, hydrogen concentration of hydrogen in Ti increases with increasing gas concentration [2.15, 2.16].

Hydrogen atoms in titanium occupy octahedral or tetrahedral sites. Theoretical calculations showed that hydrogen atoms prefer octahedral sites at low hydrogen concentration and tetrahedral sites at high hydrogen concentrations in α-Ti [2.17]. In β-phase hydrogen atoms occupy tetrahedral sites [2.18].

2.3   Phase transformation in Ti and Ti6Al4V alloy

Hydrogen absorption in titanium can lead to formation of different phases depending on the amount of hydrogen absorbed and temperature. Ti-H and Ti6Al4V-H phase diagram are discussed in this section.

2.3.1   Titanium- Hydrogen binary system

Three different hydrides have been reported in literature: δ, γ, and ϵ hydride. Figure 2.4 shows the phase diagram of the titanium-hydrogen system. Hydrogen forms interstitial solid solutions in the α - Ti and β - Ti phases at low hydrogen concentration and hydride phases at high hydrogen concentration. Solubility of hydrogen in α - Ti at room temperature is 0.12 at % H and it increases with increasing temperature up to 7.9 at% H at temperature of 300 °C and remains constant up to 600 °C. Above 600 °C the solubility of hydrogen in α-phase decreases. Hydrogen is a β-stabilizing element in Ti, it decreases the β-transus temperature from 883 °C to 300 °C.

The metastable hydride (γ) precipitates in the α - Ti(H) solid solution in the hydrogen concentration range of 1 to 3 at.% . The δ-hydride has a face centered cubic structure and can exist as a mixture in α - δ or β - δ. At room temperature it forms a single phase material if the concentration of hydrogen is between 60 and 66 at % H. The ϵ-hydride with a tetragonally distorted fcc structure is formed at higher hydrogen concentration greater than 66 at.% H [2.13, 2.19].
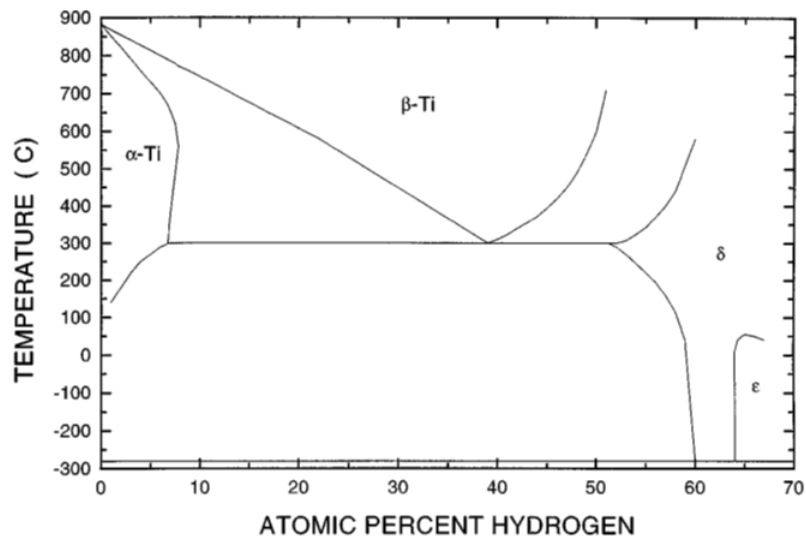
Figure 2.4: Ti - H equilibrium phase diagram [2.13].

2.3.2 Ti6Al4V- H system

The effect of hydrogen on phase transformation in Ti6Al4V alloy was studied by several authors and they proposed temperature-hydrogen concentration phase diagrams (Figure 2.5). Kerr et al [2.20] published the first phase Ti6Al4V-H phase diagram, Figure 2.5 (a). Hydrogen is a beta stabilizing element in Ti6Al4V alloy. The β-transus temperature decreases from $1000\,^{\circ}$C to $800\,^{\circ}$C with addition of 20 at.% of hydrogen. Researchers published different results on temperature of hydride formation. According to Kerr et al [2.20], titanium hydride (δ) is formed at hydrogen concentration greater than 15 at.% and is stable up to $800\,^{\circ}$C. Ilyin et al. [2.21] found that hydride formation occurs at a temperature of around $250\,^{\circ}$C in the alloy containing hydrogen concentration greater than 13 at %. Their phase diagram is shown in Figure 2.5 (b).

Qazi et al [2.22] proposed the phase diagram shown in Figure 2.5 (c). It agrees and extends the results obtained by Kerr et al [2.20], it was shown that hydride phase is formed above 15 at.% of hydrogen and in addition to Kerr's results there also exists a beta + hydride phase ($\beta + \delta$) which is stable above $815\,^{\circ}$C.
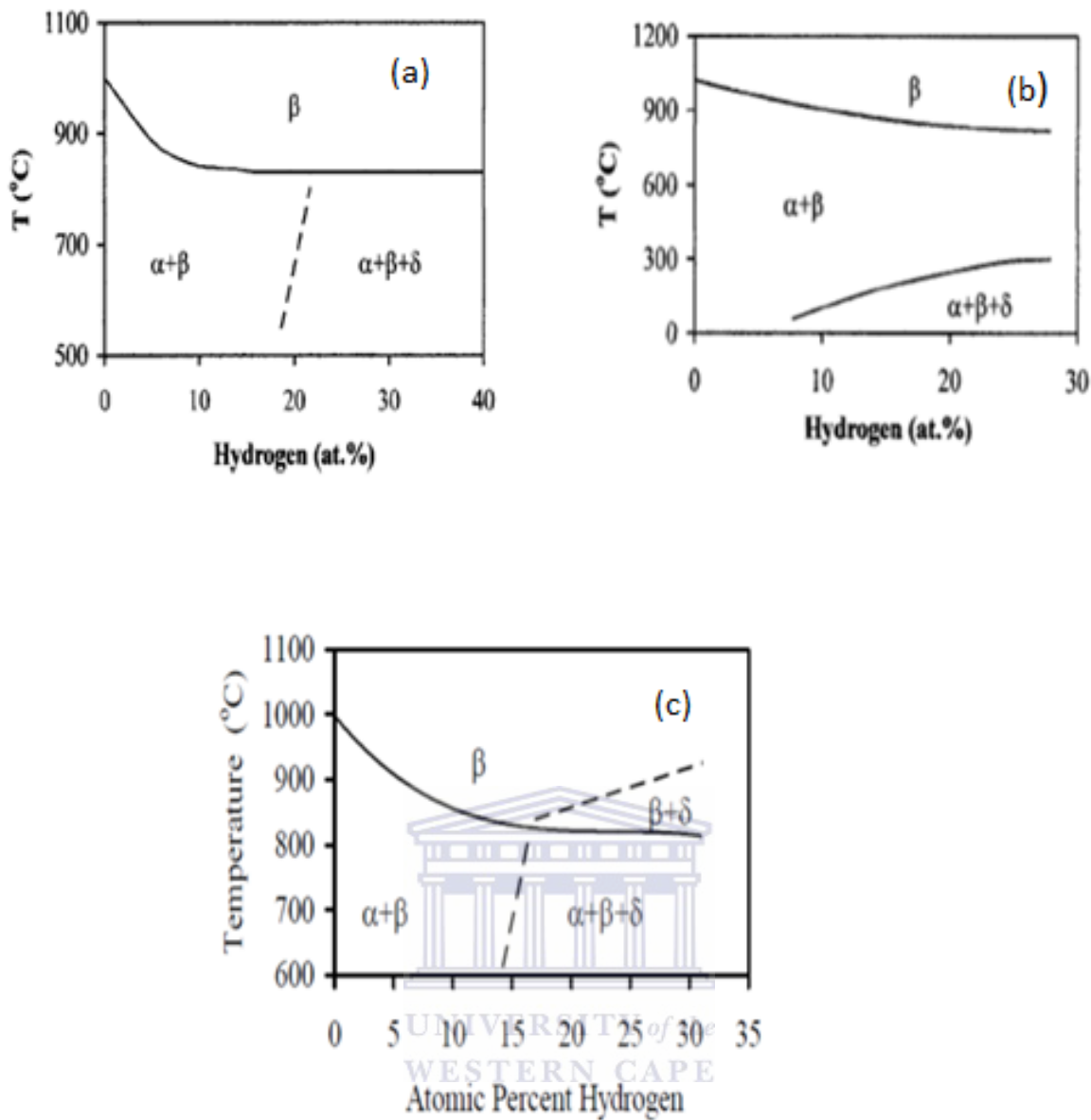
Figure 2.5: Phase boundaries in Ti6Al4V-H system as defined by : (a) Kerr et al. [2.20], (b) Ilyin et al. [2.21], (c) Qazi et al. [2.22].

2.4   Effect of hydrogen on the microstructure of Ti and Ti6Al4V alloy

Ti6Al4V alloy exists in different types of microstructure depending on the volume fractions and arrangements of the α and β-phases. For many years hydrogen has been considered as a harmful element in Ti, however a recent understanding in titanium metallurgy has demonstrated that hydrogen can be used as a temporary alloying to modify the microstructure of titanium and Ti6Al4V alloy [2.23, 2.24]. The effect of hydrogen on the microstructure of Ti and Ti6l4V alloy has been

reported in various studies [2.25, 2.31]. It was shown that absorption of hydrogen in CP-T and Ti6Al4V alloy can lead to formation of martensites as well as titanium hydrides. Figure 2.6 shows the change in microstructure of Ti6Al4V alloy in the samples containing different hydrogen content. Before hydrogenation the microstructure consists of the $\alpha+\beta$ dual phase, as seen in Figure 2.6 (a). With increase in hydrogen content the needle α-phase is formed, Figure 2.6 (b). A further increase in hydrogen content leads to formation of α-lath structure and fine needles α martensite, as shown in Figure 2.6 (c) and (d).
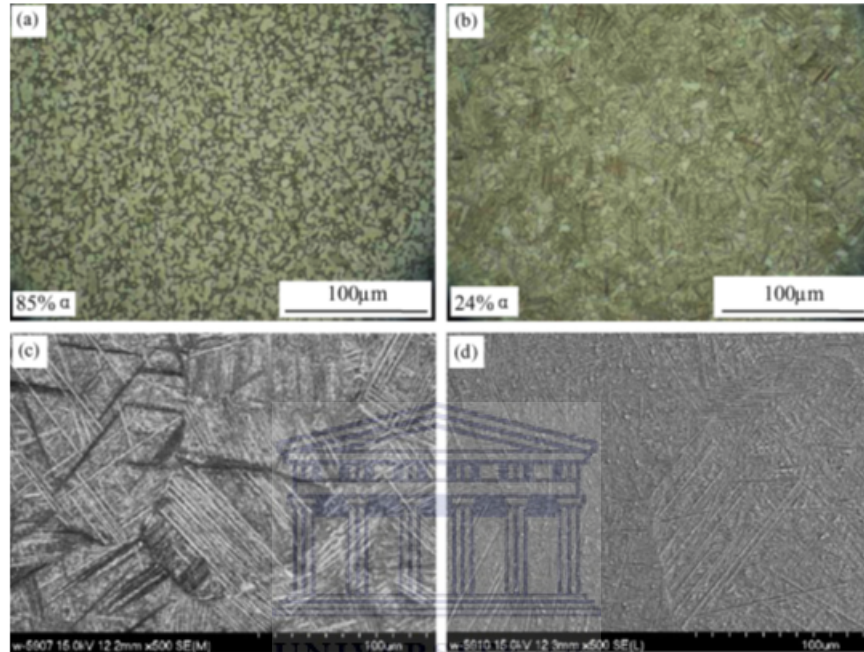
Figure 2.6: Microstructure of the Ti6Al4V: (a) before hydrogenation; (b) hydrogenated 0.2 wt.%; (c) hydrogenated 0.3 wt.%; (d) hydrogenated 0.5 wt.% [2.28].

The above experimental results show clearly that hydrogen can be used to modify the microstructure of Ti and Ti alloys.

2.5 Effect of thin film coating on hydrogen storage

2.5.1 Introduction

Most hydride forming metals and alloys are normally covered with a surface passivation layer which consists of metal oxides, hydroxides, carbon-oxygen compounds and water. This layer prevents hydrogen diffusion into the metal [2.32]. Hydrogen storage materials require some form of activation before they can absorb hydrogen. The activation can be done by hydrogenating metals

at high pressure and temperature or by coating the material with a catalytic layer. Platinum group metals are well known as catalysts for dissociation of molecular hydrogen in metal hydrides [2.33, 2.34].

2.5.2   Surface coatings on Ti and Titanium alloy

Titanium forms an oxide layer (TiO_2) at room temperature [2.35]. This oxide layer is a barrier for the transport of hydrogen atoms, and causes slow kinetics [2.36].

Palladium (Pd) has the ability to absorb large volumetric quantities of hydrogen at room temperature and atmospheric pressure, as a result it has been used as a hydrogen sensor and hydrogen selective membrane for hydrogen purification [2.37-2.39]. It acts as a catalyst for attracting hydrogen on Ti and diffusion through the TiO_2 layer [2.40]. It can be also used to prevent surface oxidation in Ti and Ti alloys [2.41]. Pd alloying or coating has been used to promote absorption of hydrogen on bulk of Ti and Titanium alloy [2.42, 2.43]. Cabrera et al [2.44] studied hydrogen absorption in titanium thin films at low pressure and room temperature. These films did not absorb hydrogen before Pd coating. However when coated with a thin layer of palladium hydrogen absorption occurred. Zaluski et al [2.42] also reported on the effect of Pd on hydrogen absorption in FeTi alloy. It was shown that the Pd modified FeTi alloy was able to absorb hydrogen at low temperature and pressure without any activation prior to hydrogenation. It was also observed that hydrogen concentration was increased after palladium coating. Catalytic layer deposited on materials to be hydrogenated accelerates hydrogen absorption kinetics by promoting the dissociation of hydrogen atoms. The dissociation mechanism is known as the spillover mechanism. The schematic of a spillover mechanism is shown in Figure 2.7. Deposition of the catalytic layer on the surface of the material to be hydrogenated changes hydrogen absorption mechanism. Since the catalyst has high affinity for hydrogen, hydrogen molecule prefer to adsorb and dissociate into hydrogen atoms on the surface of the catalytic layer and then diffuse through the particles of the catalytic material and penetrate into the material to be hydrogenated, where hydrogen is said to spill-over and interact directly with the material [2.38, 2.45].
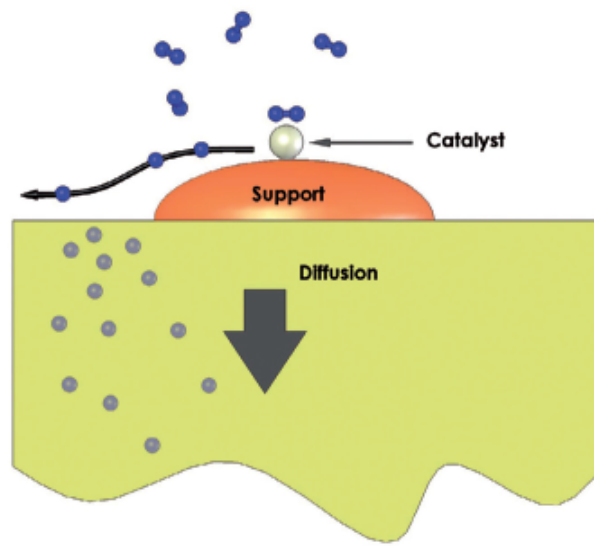
Figure 2.7: Spillover mechanism [2.38].

2.6   Summary of literature review

The literature review conducted in this study showed that :

- A suitable material for hydrogen storage is a key requirement for a possible hydrogen economy.

- Hydrogen storage capacity of a material depends on experimental conditions (time, temperature, gas concentration and pressure).

- Hydrogen can be used as an alloying element to refine the microstructure of Ti and Ti alloys,

- Hydrogen can be stored in Ti to form a metal hydride.

- Deposition of platinum group metals on the surface of hydrogen storage materials can improve hydrogen absorption properties.

References

[2.1] G. Sandrock, A panoramic overview of hydrogen storage alloys from a gas reaction point of view, *Journal of Alloys and Compounds*, **293-295**, 877-888 (1999).

[2.2] T.Wang, F. Eichhor, D. Grambole, R. Grotzschel, F. Herrmann, U. Kreissi and W. Moller, A new Ti/H phase transformation in the H_2^+ titanium alloy studied by X-ray diffraction, nuclear reaction analysis, elastic recoil detection analysis and scanning electron microscopy, *Journal of Physics: Condensed Matter*, **14**, 11605–11614 (2002).

[2.3] J.E. Lennard-Jones, Processes of adsorption and diffusion on solid surfaces, *Transaction of the Faraday Society*, **23**, 333-359 (1932).

[2.4] M. Dorheim, *Thermodynamics of metal hydrides: tailoring reaction enthalpies of hydrogen storage materials*, *InTech*, http://www.intechopen.com/books/thermodynamics-interaction-studies-solids-liquids-and-gases/thermodynamics-of-metal-hydrides-tailoring-reaction-enthalpies-of-hydrogen-storage-materials (2011).

[2.5] M. Hirscher, *Handbook of hydrogen storage new materials for future energy storage*, Wiley-VCH (2010).

[2.6] S.A. Sherif, Y.D. Goswami, E.K. Stefanakos, A. Steinfeld, editors, *Handbook of hydrogen energy*, Taylor and Francis (2014).

[2.7] G. Lütjering, J.C. Williams, *Titanium*, Springer Science and Business Media (2007).

[2.8] C. Leyens, M. Peters, *Titanium and Titanium alloys: Fundamentals and Applications*, WILEY-VCH (2003).

[2.9] A. Lopez-Suarez, J. Rickards, R.Trejo-Luna, Analysis of hydrogen absorption by Ti and Ti-6Al-4V using the ERDA technique, *International Journal of Hydrogen Energy*, **28**, 1107-1113 (2003).

[2.10] Y. Furuya, A. Takasaki, K. Mizuno, T. Yoshiie, Hydrogen desorption from pure titanium with different concentration levels of hydrogen, *Journal of Alloys and Compunds*, **446 - 447**, 447 - 450 (2007).

[2.11] J.L. Blackburn, P.A. Parilla, T. Gennett, K.E. Hurst, A.C. Dillion, M.J. Heben, Measuremrnt of the reversible hydrogen storage capacity of milligram Ti-6Al-4V alloy samples with temperature programmed desorption and volumetric techniques , *Journal of alloy compounds*, **454**, 483-490 (2008).

[2.12] E. Tal-Gutelmacher, R. Gema, A. Pundt, R. Kirchheim, Hydrogen behaviour in nanocrystalline titanium thin films, *Acta Materialia*, **58**, 3042-3049 (2010).

[2.13] A. San-Martin, F.D. Manchester, The H-Ti (Hydrogen-Titanium) system, *Bulletin of Alloy Phase Diagrams*, **8**, 30-42 (1987).

[2.14] N.A Braga, N.G. Ferreira, M.R. Baldan, Hydrogen effect on the morphology and structure of 3D titanium in the HFCVD-diamond growth environment, *Materials Characterization*, **62**, 995-999 (2011).

[2.15] M.G. Olayo, G.J. Cruz, T. Martines, L. Melendez, R. Valencia, E. Chavez, A. Flores, R. Lopez, Sorption of hydrogen in titanium plates at low pressure, *International Journal of Hydrogen Energy*, **23**, 15-18 (1998).

[2.16] L.A. Matthews, R.D. Knusten, Microstructure evolution in Ti-6Al-4V alloy during hydrogen dosing at elevated temperatures, *The Journal of The South African Institute of Mining and Metallurgy*, **111**, 155-158 (2011).

[2.17] Q. Xu, A. Van der Ven, First-principles investigation of metal-hydride phase stability: The Ti-H system, *Physical Review B*, **76**, 1-12 (2007).

[2.18] D.V. Schur, S.Yu. Zaginaichenko, V.M. Adejev, V.B. Voitovich, A.A. Lyashenko, V.I. Trefilo, Phase transformations in titanium hydrides, *International Journal of Hydrogen Energy*, **21**, 1121-1124 (1996).

[2.19] R. Checchetto, P. Scardi, Structural characterization of deuterated titanium thin films, *Journal of Materials Research*, **14**, 1969 - 1976 (1999).

[2.20] W.R, Kerr, The Effect of Hydrogen as a Temporary Alloying Element on the Microstructure and Tensile Properties of Ti-6AI-4V, *Metallurgical Transactions A*, **16A**, 1077 - 1078 (1995).

[2.21] A.A. Ilyin, B.A. Kolachev, A.M. Mamonov, Phase and structure transformations in titanium alloys under thermohydrogenous treatment, *Titanium*, **92**, 941–947 (1992).

[2.22] J.I. Qazi, and O.N. Senkov, F.H. Froes, Phase transformations in the Ti-6Al-4V-H system, *The Journal of The Minerals, Metals and Materials Society* , **54**, 68 - 71 (2002).

[2.23] D. Eliezer, N. Eliaz, O.N. Senkov, F.H. Froes, Positive effects of hydrogen in metals, *Materials Science and Engineering* , **A280**, 220-224 (2000).

[2.24] F.H. Froes, O.N. Senkov, J.I Qazi, Hydrogen as a temporary alloying element in titanium alloys : thermohydrogen processing, *International Materials Review*, **49**, 227-245 (2004).,

[2.25] Y. Zhang, S.Q. Zhang, Hydrogenation Characteristics of Ti-6Al4V cast alloy and its microstructural modification by hydrogen treatment, *International Journal of Hydrogen Energy*, **22**, 161-168 (1997).

[2.26] L. Luo, Y. Su, J. Guo, H. Fu, Formation of titanium hydride in Ti-6Al-4V alloy, *Journal of Alloys and Compounds*, **425**, 140-144 (2006).

[2.27] H.J. Liu, L. Zhou, P. Liu, Q.W. Liu, Microstructural evolution and hydride precipitation mechanism in hydrogenated Ti–6Al–4V alloy, *International Journal of Hydrogen Energy*, **34**, 9596 – 9602 (2009).

[2.28] D.B. Shan, Y.Y. Zong, T.F. Lu, Y. Lv, Microstructural evolution and formation mechanism of FCC titanium hydride in Ti–6Al–4V–xH alloys , *Journal of Alloys and Compounds*, **427**, 229-234 (2007).

[2.29] A. Czerwinskia, R. Lapovoka, D. Tomusa, Y. Estrina, A. Vinogradovc, The influence of temporary hydrogenation on ECAP formability and low cycle fatigue life of CP titanium, *Journal of Alloys and Compounds*, **509**, 2709-2715 (2011).

[2.30] L.Miaoquan, Z. Weifu, Z. Tangkui, H. Hongliang, Li. Zhiqiang, Effect of hydrogen on microstructure of Ti-6Al-4V alloy, *Rare metal materials and engineering*, **30**, 1-5 (2010).

[2.31] J. Zhao, H. Ding, Y. Zhong, C.S. Lee, Effect of thermo-hydrogen treatment on lattice defects and microstructure refinement of Ti6Al4V alloy, *International Journal of Hydrogen Energy*, **35**, 6448-6454 (2010).

[2.32] J. Bloch, M.H. Mintz, Kinetics and mechanisms of metal hydrides formation—a review, *Journal of Alloys and Compounds*, **253-254**, 529-541 (1997).

[2.33] M. Williams, M.V. Lototsky, V.M. Linkov, A.N. Nechaev, J.K. Solberg, V.A. Yartys, Nanostructured surface coatings for the improvement of AB5-type hydrogen storage intermetallics, *International Journal of Energy Research*, **33**, 1171-1179 (2009).

[2.34] Xi. Shan, J.H. Payer, W.D. Jennings, Mechanism of increased performance and durability of Pd- treated metal hydriding alloys , *International Journal of Hydrogen Energy*, **34**, 363 - 369 (2009).

[2.35] E. Gemelli, N.H.A. Camargo, Oxidation kinetics of commercially pure titanium, *Revista Matéria*, **12**, 525-531 (2007).

[2.36] I.N. Filimonova, V.V. Yuschenkoa, A.V. Smirnova, S.N. Nesterenkoa, I.V. Dobryakovaa, I.I. Ivanovaa, E.N. Lubninb, L. Galperinc, R.H. Jensenc, Deactivation of titanium during temperature-induced hydrogen absorption–desorption cycling I. Effects of water, oxygen and nitrogen traces, *Journal of Alloys and Compounds*, **390**, 144-154 (2005).

[2.37] Y. Ling, Y. Cheng, Hydrogen diffusion and solubility in palladium thin films, *International Journal of Hydrogen Energy*, **21**, 281-291 (1996).

[2.38] B.D. Adams, A. Chen, The role of palladium in a hydrogen economy , *Materials Today*, **37**, 282-289 (2011).

[2.39] S. Ramos de Debiaggi, E.A. Crespo, F.U. Braschi, E.M. Bringa, M.L. Ali, M. Ruda, Hydrogen absorption in Pd thin-films, *International Journal of Hydrogen Energy*, **39**, 1-6 (2014).

[2.40] K. Drogowska, S. Flege, C. Schmitt, D. Rogalla, H-W. Becker, Nhu-TH. Kim-Ngan, A. Brudnik, Z. Tarnawski, K. Zakrzewska, M. Marszałek, A.G. Balogh, Hydrogen Charging Effects in Pd/Ti/TiO 2/Ti Thin Films Deposited on Si (111) Studied by Ion Beam Analysis Methods, *Advances in Materials Science and Engineering*, **2012**, 1-8 (2011).

[2.41] E.M.B. Heller, J.F. Suyver, A.M. Vredenberg, D.O. Boerma, Oxidation and annealing of thin FeTi layers covered with Pd, *Applied Surface Science*, **150**, 227-234 (1999).

[2.42] L. Zaluski, A. Zaluska, P. Tessier, J.O. Ström-Olsen, R. Schulz, Catalytic effect of Pd on hydrogen absorption in mechanically alloyed Mg2Ni, LaNi5 and FeTi, *Journal of Alloys and Compounds*, **217**, 295-300 (1995).

[2.43] H.J. Christ, M. SchuÈtz, S. Zeitler, Thermogravimetric study of the hydrogen uptake of the metastable β-titanium alloy Ti 38-6-44, *Materials and Corrosion*, **49**, 13-17 (2006).

[2.44] A.L. Cabrera, J.I. Avila, D. Lederman, Hydrogen absorption by metallic thin films detected by optical transmittance measurements, *International Journal of Hydrogen Energy*, **35**, 10613–10619 (1994).

[2.45] X. Xu, C. Song, Improving hydrogen storage/release properties of magnesium with nano-sized metal catalysts as measured by tapered element oscillating microbalance, *Applied Catalysis A: General*, **300**, 130-138 (2006).

Chapter 3

Materials and Methods

3.1 Introduction

In this chapter sample preparation, hydrogenation process and characterization techniques used to carry out the investigation will be described.

3.2 Sample description

Three sets of materials were used in this study: commercially pure titanium and Ti6Al4V alloy and palladium (Pd). Bulk CP-Ti with 99.6% purity and Ti6Al4V alloy were supplied by Goodfellow Ltd company in an half annealed condition. Ti6Al4V alloy consists of 6 wt% Al, 4 wt%V and 90 wt% Ti. The samples of Ti6Al4V alloy were cut into cubes of $10 \times 10 \times 2$ mm and CP-Ti samples were cut into round disks with diameter of 16 mm and thickness 2 mm. Pd coatings were deposited on Ti6Al4V substrate.

3.3 Sample preparation

3.3.1 Hot mounting

Samples were mounted on Struers Labopress-3 machine using acrylic resin. During the mounting the temperature was set to $180\,^{\circ}$C and time of 18 minutes (9 minutes for heating the resin and 9 minutes cooling). At the temperature of $180\,^{\circ}$C the acrylic resin melts and upon cooling it solidifies into the sample. A force of 20 kN is applied during mounting process.

3.3.2 Polishing

Mounted samples were afterwards polished using Struers Tegrapol-11 machine. The polishing steps were as follows:

In the first polishing step, samples were grinded using 800 μm and 1200 μm SiC paper respectively to obtain a flat sample and to eliminate asperities left from machining and previous grinding processes. After each grinding step the samples were rinsed with water to remove previous grinding media. Diamond paste with 9 μm grain size and MD DUR pad were used to polish the samples. In the last step a mixture of OP-S (collodial silica suspension) 25 ml and 5 ml H_2O_2 were used to produce a scratch-free mirror finish surface.

3.3.3 Cleaning

After polishing the samples were cleaned to remove contaminants on the surface. Samples were cleaned in the ultrasonic bath following the standard procedure given in Table 3.1. After cleaning samples were dried using liquid nitrogen.

Cleaning agent	Time (min)
Methanol	10
Acetone	10
Trichlorothylene	10
Acetone	10
Ethanol	5

Table 3.1: Cleaning procedure.

3.3.4 Etching

In order to reveal the microstructure the samples were etched through selective chemical attack. 1 to 2 drops of the etching reagent were poured on the surface of the material. Ti6Al4V alloy was etched between 8 and 10 seconds, whereas the commercially pure titanium was etched between 3 and 5 seconds. After etching, samples were immediately rinsed with water and wiped with cotton wool, then dried in hot air. CP-Ti and Ti6Al4V alloy were etched using Keller's and Kroll's reagents respectively. The composition of Keller's and Kroll's reagent are shown in Table 3.2 and Table 3.3

Composition	volume (ml)
H_2O	95
HNO_3	2.5
HF	1
HCl	1.5

Table 3.2: Keller's reagent [3.1].

Composition	volume (ml)
H_2O	100
HNO_3	4
HF	2

Table 3.3: Kroll's reagent [3.1].

Etching is a controlled corrosion process resulting from electrolytic actions between surface areas of different potential in a material. In pure metals, a potential is produced between grains of different orientations, grain boundaries and interiors, between impurity phases and the matrix. In a two phase alloy, potential differences are produced between phases of different compositions [3.1]. The etchants reveal the microstructure of the material by preferentially attacking grain boundaries or by preferential etching of grains of different orientations.

3.3.5 Thin film deposition

Titanium was coated with 200 nm palladium layer using electron beam evaporation system at iThemba LABS. The deposition process was carried out at room temperature.

The schematic of electron beam evaporation technique is shown in Figure 3.1. The target material (Pd) was placed into the copper crucible, Ti substrate was placed on the sample holder and inserted into the vacuum chamber. A voltage of 5 kV was applied across the tungsten filament, thus causing electrons to be emitted. Electrons emitted from cathode are focused by electromagnets onto the target material which acts as an anode. The kinetic energy of the electrons is converted into thermal energy, melting and vaporizing the target material. The vaporized material forms a coating on the substrate. The base vacuum pressure was 0.01 Pa. The deposition rate was varied between 0.08 - 0.16 $\mathring{A}$/s and current between 90 and 100 mA was applied. The thin film thickness

was set to 200 nm and was monitored using a quartz crystal monitor.
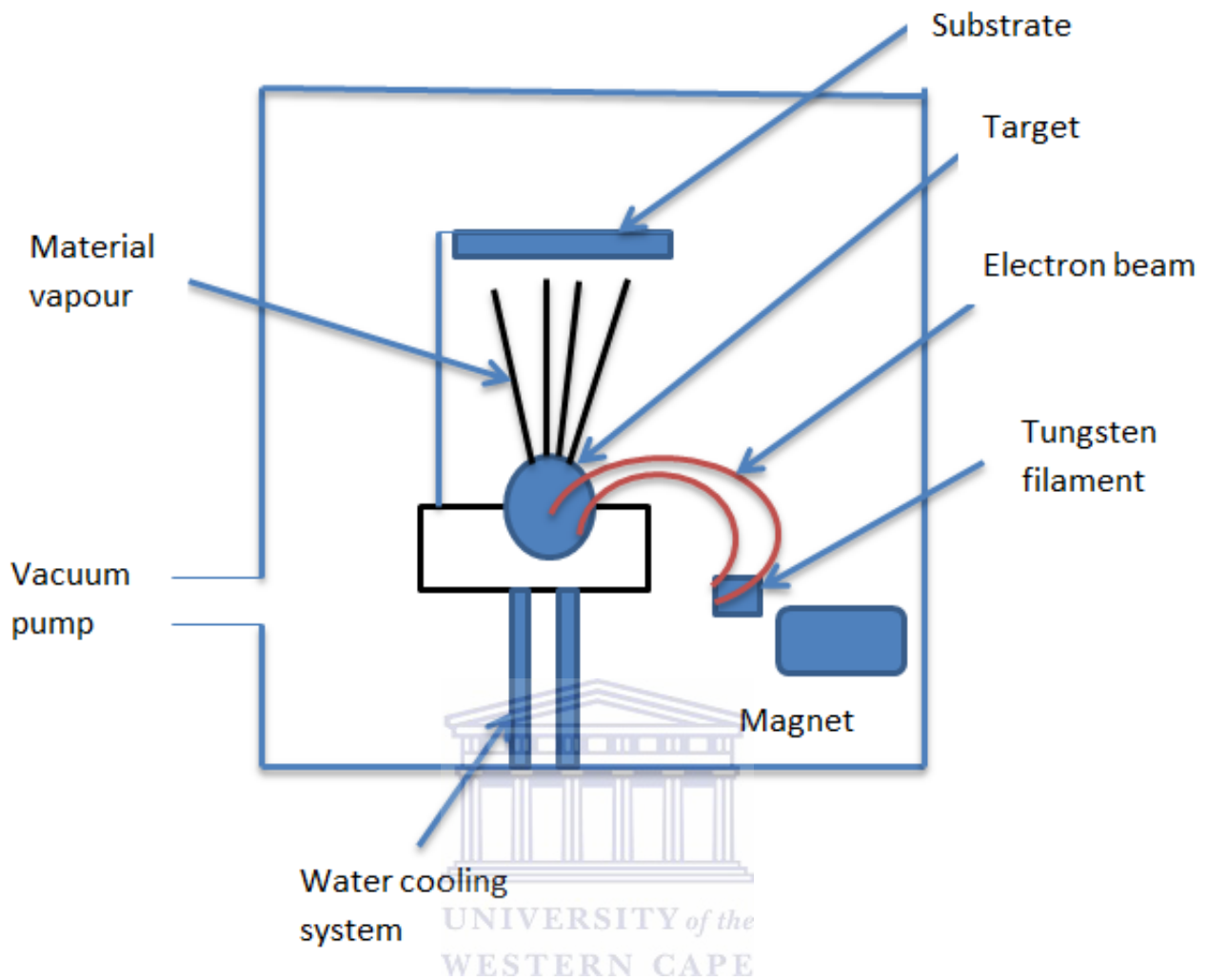
Figure 3.1: Schematic representation of electron beam evaporation system.

3.4   Hydrogenation

Hydrogenation was carried out at the University of Cape Town to investigate the effect of tempera-
ture on hydrogen absorption using vacuum furnace shown in Figure 3.2. Samples were hydro-
genated at room temperature, $450\,°C$, $550\,°C$ and $650\,°C$ and each sample was hydrogenated for
a period of 3 hours at atmospheric pressure. Samples were placed in the vacuum furnace using
the specimen holder and were heated up to desired hydrogenation temperature and cooled under
vacuum to room temperature, at a rate $5\,°C/min$. Turbo molecular pump (E) was used to create
vacuum in the system, a vacuum of about 0.001 Pa was achieved. Hydrogen gas mixture of 85% Ar
and 15% H was introduced into the system. The pressure inside the furnace was kept at constant

(10 kPa) above atmospheric pressure. The cracker valve (I) is used to make sure that the gas flows out of the furnace through the gas extractor (H) and it was set to release gas at 110 kPa to maintain a constant positive pressure of 10 kPa in the furnace. Pressure gauge (A) was used to monitor pressure in the system during measurements.
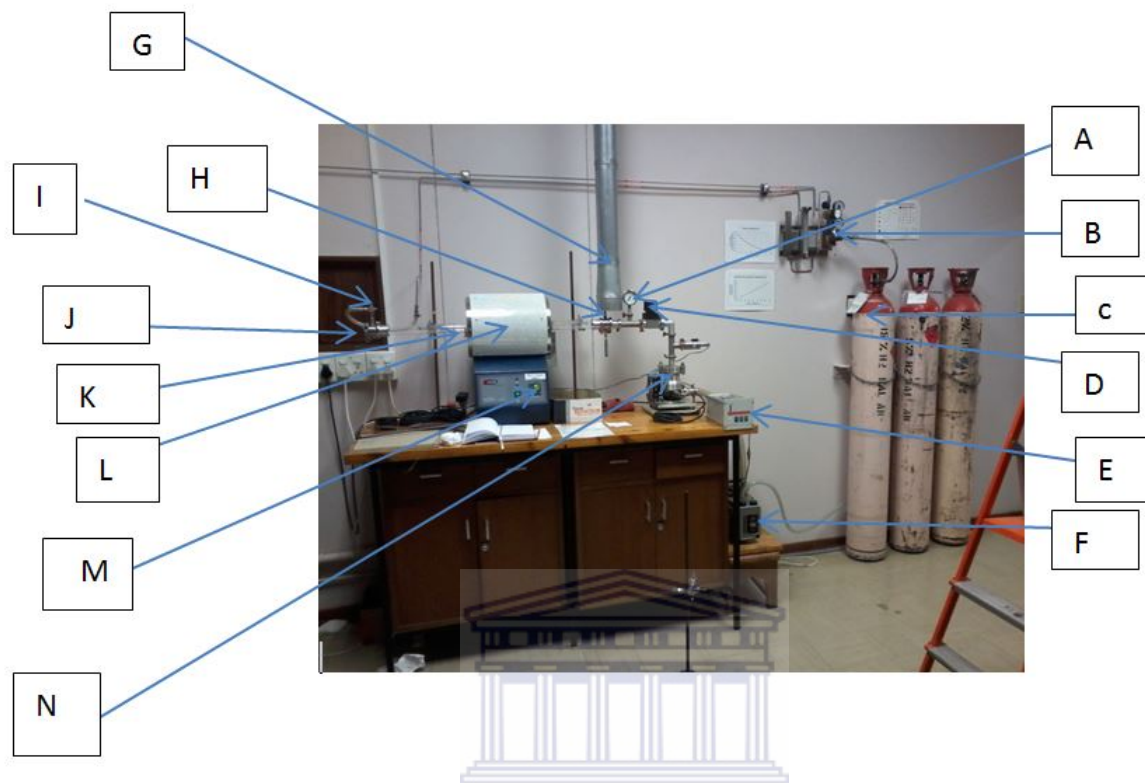
Figure 3.2: Experimental setup for hydrogenation

A) pressure gauge

B) gas regulator

C) gas cylinder mixture

D) isolation valve

E) turbo molecular pump

F) vacuum pump

G) gas extractor chamber

H) crack valve

 I) gas inlet valve

J) end cap

K) silica glass (quartz tube)

L) furnace

M) furnace temperature display

N) air cooling system

To prevent hydrogen diffusion out of samples when taken out of furnace, the samples were stored in liquid nitrogen immediately after hydrogenation.

Because of the danger associated with hydrogen, safety protocols need to be followed when handling hydrogen gas. It is very important for the person working with hydrogen to first understand the properties of hydrogen. Hydrogen is a colorless,odorless and a highly flammable gas. High-pressure leaks can ignite spontaneously and burn with a colorless flame.

Before starting the hydrogenation experiment, the user must ensure that all hydrogen gas cylinder knobs are closed, correct cylinder gas is used, make sure that there are no leaks in the gas cylinders and vacuum by performing a leak detection test. Ensure that power switches are initially off. As with laboratory safety in general the user must be sure to wear safety goggles, laboratory coats and gloves. If hydrogen is leaking, the gas supply has to be cut off by closing the valves.

3.5   Analytical techniques

The hydrogenated samples were then characterized by several techniques including elastic recoil detection analysis (ERDA), Rutherford backscattering spectrometry (RBS), X-ray diffraction, optical microscopy and high resolution scanning electron microscopy (HRSEM), which will be described in this section.

3.5.1   Elastic Recoil Detection Analysis

ERDA is an ion beam analysis fast and nondestructive technique in which MeV ions are used to kinematically recoil target atoms and for depth profiling of light elements with atomic number $1 < Z < 8$ [3.2]. ERDA was used to determine the concentration and depth profiling of hydrogen.

Theory

Target sample is irradiated by high energy ion beam. The collision between the accelerated ion and the atomic nucleus is governed by the coulomb repulsive force and can be described as an elastic collision. Geometric representation of two particles with mass M_1 and M_2 colliding is shown in Figure 3.3, where θ is the scattering angle and ϕ the recoil angle. Energies of the scattered particle E_1 and recoil particle E_2 can be determined by laws of conservation of energy and momentum and are given by the following equations :

$$E_1 = K_s E_0 \tag{3.1}$$

$$E_2 = K_r E_0 \tag{3.2}$$

where K_s is the kinematic factor of the projectile when scattered at an angle θ given by

$$K_s = \left(\frac{(M_2^2 - M_1^2 \sin^2 \theta)^{\frac{1}{2}} + M_1 \cos \theta}{M_2 + M_1} \right)^2 \tag{3.3}$$

and K_r is the kinematic factor of the recoiled atom given by

$$K_r = \frac{4 M_1 M_2 \cos^2 \phi}{(M_1 + M_2)^2} \tag{3.4}$$

The kinematic factor depends only of the mass ratio $\frac{M_1}{M_2}$ and the scattering angle θ.
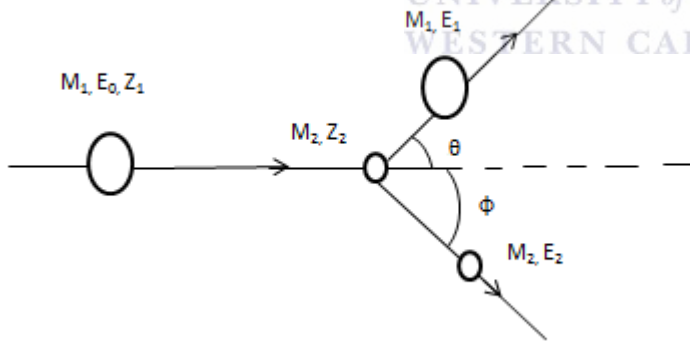
Figure 3.3: Elastic collision between a projectile of mass M_1, atomic number Z_1, and energy E_0 and a target of mass M_2, atomic number Z_2 initially at rest.

The probability of one particle from an ion beam to eject a recoil element is defined by the well known Rutherford differential cross section $\frac{d\sigma}{d\Omega}$

$$\frac{d\sigma}{d\Omega} = \left(\frac{Z_1 Z_2 e^2}{2 E_1} \right)^2 \frac{(1 + \frac{M_2}{M_1})^2}{\cos^3 \phi} \tag{3.5}$$

where Z_1 and Z_2 is the atomic number of the incident beam and target material respectively [3.3]. The total yield of the Y_r of the scattered or recoil for a specific element is given by

$$Y = N_r Q \Omega \sigma_r \qquad (3.6)$$

where N_r is the number of target atoms per unit area, Q is the total number of projectiles, Ω is the solid angle of the detector and σ is the cross section. In practice the solid angle Ω is often calibrated from the height of hydrogen profile obtained from a standard with a known quantity. In this study a Kapton foil was used as a standard for calibration of the experiment with a known thickness and concentration of hydrogen.
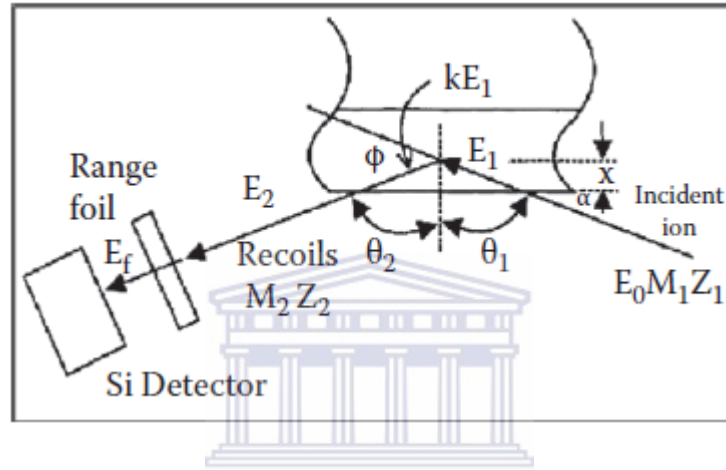
Figure 3.4: Geometry of ERD setup: E_0 is the energy of the incident beam, KE_1 is the energy of the recoiled atoms at depth x, E_2 is the energy of the recoiled atoms after leaving the target material [3.4].

The geometry of ERD setup is presented in Figure 3.4. As the incident ion with energy E_0 penetrates into the target material it undergoes a series of elastic collisions. During the collisions it looses energy $\triangle E_1$ before reaching the depth of x. The energy loss of the incident particle is given by

$$\triangle E_1 = E_0 - E_1 = S_1 \frac{x}{\sin \alpha} \qquad (3.7)$$

where S_1 is the stopping power of ingoing particle into the target. After elastic collision at depth of x, the recoiled atom has an energy KE_1. After leaving the sample the energy of the recoiled atoms is E_2. Therefore the energy loss of the outgoing particle is given by

$$\triangle E_0 = KE_1 - E_2 = S_2 \frac{x}{\sin(\phi - \alpha)} \qquad (3.8)$$

33

where S_2 is the stopping power of the ejected particle from the target material. Using equation 3.7 and 3.8 change in energy between particle recoiled from the surface and that recoiled below the surface at a depth of x can be defined as:

$$\triangle E = KE_0 - E_2 \tag{3.9}$$

$$\triangle E = \frac{KS_1}{\sin \alpha} + \frac{S_2}{\sin(\phi - \alpha)} x \tag{3.10}$$

$$\triangle E = \{S\}x \tag{3.11}$$

where $\{S\} = \frac{KS_1}{\sin \alpha} + \frac{S_2}{\sin(\phi - \alpha)}$ is the combined stopping factor. From equation 3.11 a correlation between depth and energy can be determined. For a good depth resolution, a good energy resolution and a well defined energy of particles is required. A depth resolution is also affected by the spread in energy loss in the target atoms. This energy spread is called energy straggling. Energy straggling is given by the following expression which was derived by Bohr in 1915 [3.4].

$$\sigma_B^2 = 4\pi Z_1^2 e^4 N Z_2 \Delta t \tag{3.12}$$

where Δt is the thickness of the target material, N is the atomic density of the target material.

Energy straggling is proportional to the the square root of thickness of the material, therefore straggling will increase with increasing depth thus depth resolution will deteriorate with increasing depth.
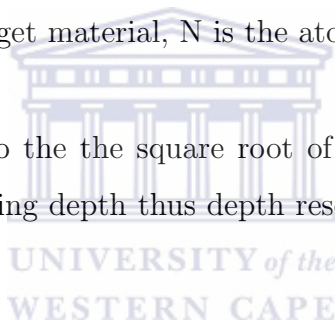
Experimental setup

The samples were irradiated with 1 mm collimated 3 MeV α-particles. Van de Graff accelerator was used to accelerate the α-particles. An accelerating voltage of 50 kV was used. Samples were mounted on the sample holder and loaded into the vacuum chamber evacuated to pressures $>$ 10^{-5} mbar. Samples were tilted to an angle of $15\,^{\circ}$ (incident angle α) with respect to the incident ion beam. Recoiled hydrogen atoms were collected by a surface silicon barrier detector positioned at an angle of $30\,^{\circ}$ (scattering angle θ) with respect to an incident ion beam. A 15 μm mylar foil was placed in front of a detector to allow only hydrogen particles to pass through while blocking other scattered ions. A total charge of 20 μC was collected at a current of 30 nA. A schematic diagram of ERDA setup is shown in Figure 3.5.
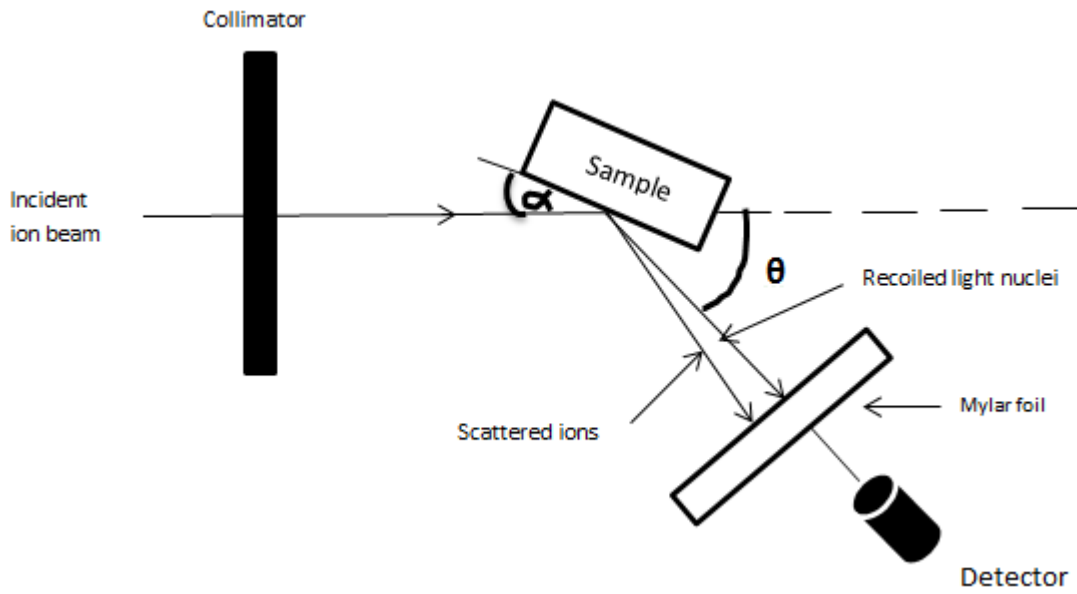
Figure 3.5: Schematic setup of ERDA showing an incident angle α and scattering angle θ.

Energy calibration

For energy calibration purpose a 125 μm kapton foil was irradiated with 2, 2.5 and 3 MeV He++ beam. Current was set to 30 nA. To obtain a correlation between the energy and channel, the following linear equation was used:

$$E(keV) = A + B \times \text{channel number} \tag{3.13}$$

where E is the detected energy, A is the calibration offset, B is energy per channel.

Table 3.4: Data for energy calibration

Energy (keV)	Channel	E_0 (keV)	E_{loss} (keV)	$E_{detected}(keV)$
3000	438	1446.30	431.519	1014.781
2500	298	1205.25	513.945	691.305
2000	119	964.20	677.081	287.119

The simulated spectra of the kapton is shown in Figure 3.7 and was used to obtain the actual energy per channel ratio with calibration offset. Data obtained from the simulation is presented in Table 3.5. The concentration of hydrogen was found as 25.64 at.% as calculated from the simulation.
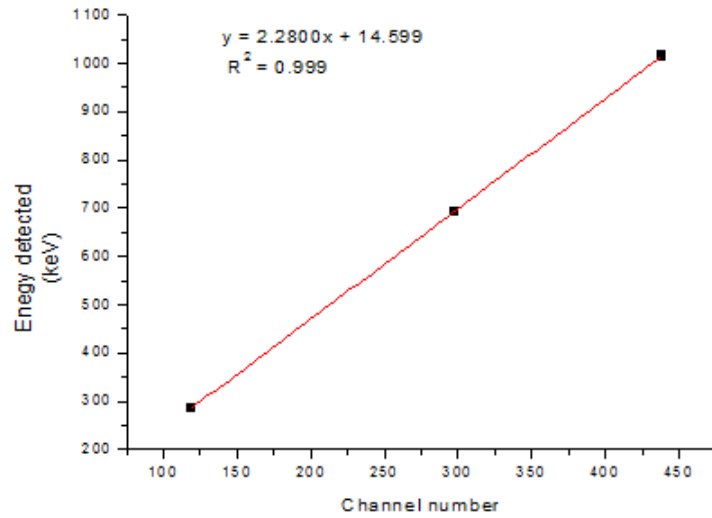
Figure 3.6: Energy channel calibration curve; The three points correspond to detected energies of recoiled hydrogen ions.
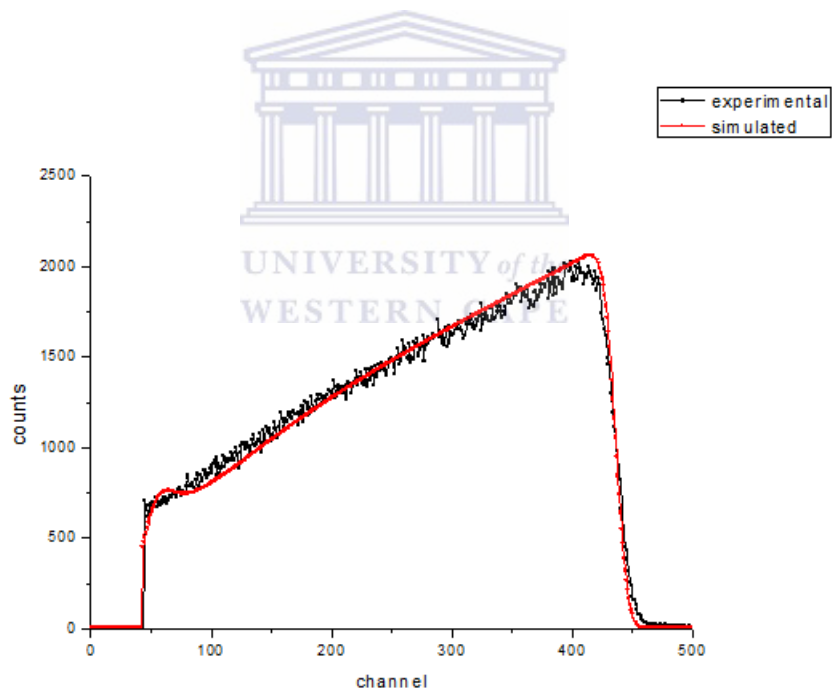
Figure 3.7: Simulated ERD spectrum showing hydrogen profile in Kapton foil bombarded with He ions at 3 MeV

Data Analysis

ERDA spectra were simulated using SIMNRA software [3.5]. The ERDA spectra were converted into hydrogen depth profile and average hydrogen concentration throughout the sample is calcu-

Table 3.5: Composition of Kapton foil obtained from the simulated spectrum (Figure 3.7) using SIMNRA software

Element	concentration (at.%)
C	54.41
H	25.64
N	51.300
O	12.82

lated as follows

$$\sum_{i=1}^{n} \frac{H_i t_i}{T} \tag{3.14}$$

where H is the hydrogen concentration at a specific layer in at.%, t is the thickness at that specific layer in monolayers (1×10^{15} atoms/cm^2), T is the total thickness, i is the order number of the layers in the sample.

3.5.2 Rutherford Backscattering Spectrometry

Introduction

RBS is a non destructive technique used for identification and depth profiling of heavy elements in the near surface region of bulk materials and thin films [3.4]. It is less sensitive to light elements and is instead highly sensitive to heavy elements. RBS analysed depth is typically about 2 μm for incident He-ions and has a good depth resolution of order of several nm. The accuracy of RBS depends strongly on the stopping powers. ERDA and RBS are similar techniques but the main difference between these two techniques is that in RBS the detected particles are the incident ions backscattered from the target sample, whereas in ERDA the detected particles are those ejected from the target sample by the incident ion in the forward direction [3.6].

The physical concepts, i.e. kinematic factor, scattering cross section, stopping power and energy straggling, governing ERDA and RBS are identical. Therefore the theory developed for ERDA remains valid for RBS. Because heavy elements cannot be detected using ERDA, RBS was used in this experiment to determine the thickness, stoichiometry of the possible formed oxide layer before and after hydrogenation as well as thickness of Pd layer deposited on Ti6Al4V samples.

Experimental setup

Figure 3.8 shows the experimental setup for RBS. A 1 mm collimated beam of 2 MeV α-particles is irradiated on the target sample. If the sample is thick, only particles backscattered by angles of more than $90\,^\circ$ can be detected. RBS was performed using same experimental chamber as that of ERDA, but for RBS, samples were tilted by an angle (α) of $10\,^\circ$ and the backscattering detector was mounted at a scattering angle (θ) of $165\,^\circ$ and voltage of 100 V was applied.
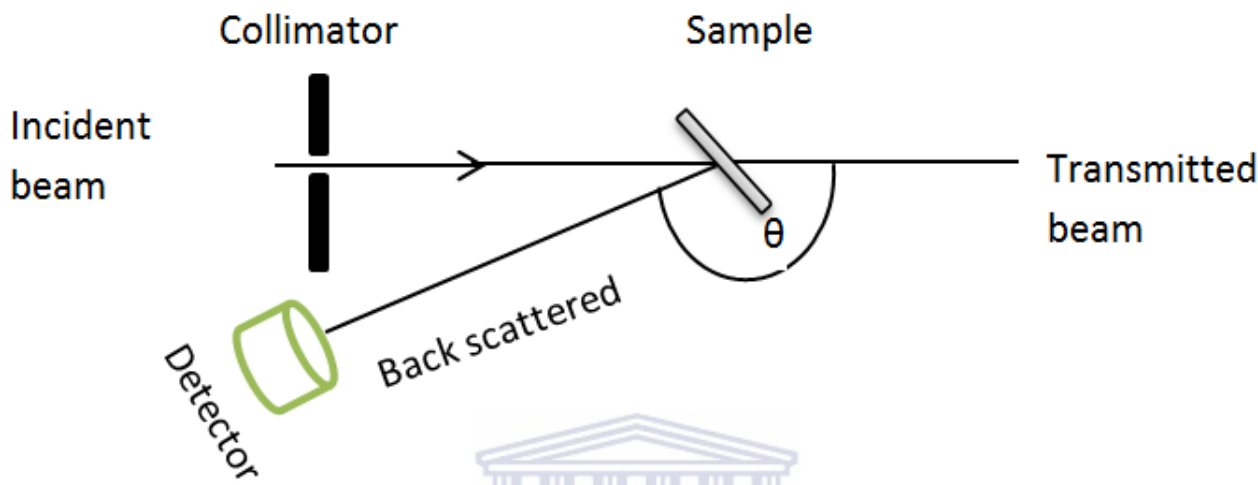
Figure 3.8: Schematic setup of RBS, θ is the scattering angle.

Energy calibration

For energy calibration four standard samples were irradiated with 2 MeV alpha particles, namely Pt, Pd, Ti and Si. These standards were used to determine the energy per channel ratio and calibration offset. Figure 3.9 shows the simulated spectrum of Pd standard deposited on Si substrate. The simulations were performed using the SIMNRA software. The thickness of Pd layer and Si substrate are known. The blue arrows indicate Pd and Si edges corresponding to the energies at which Pd and Si signals are detected.

The width of the peak is related to film thickness, the intensity and position of the peak determine concentration and elemental composition in the sample.
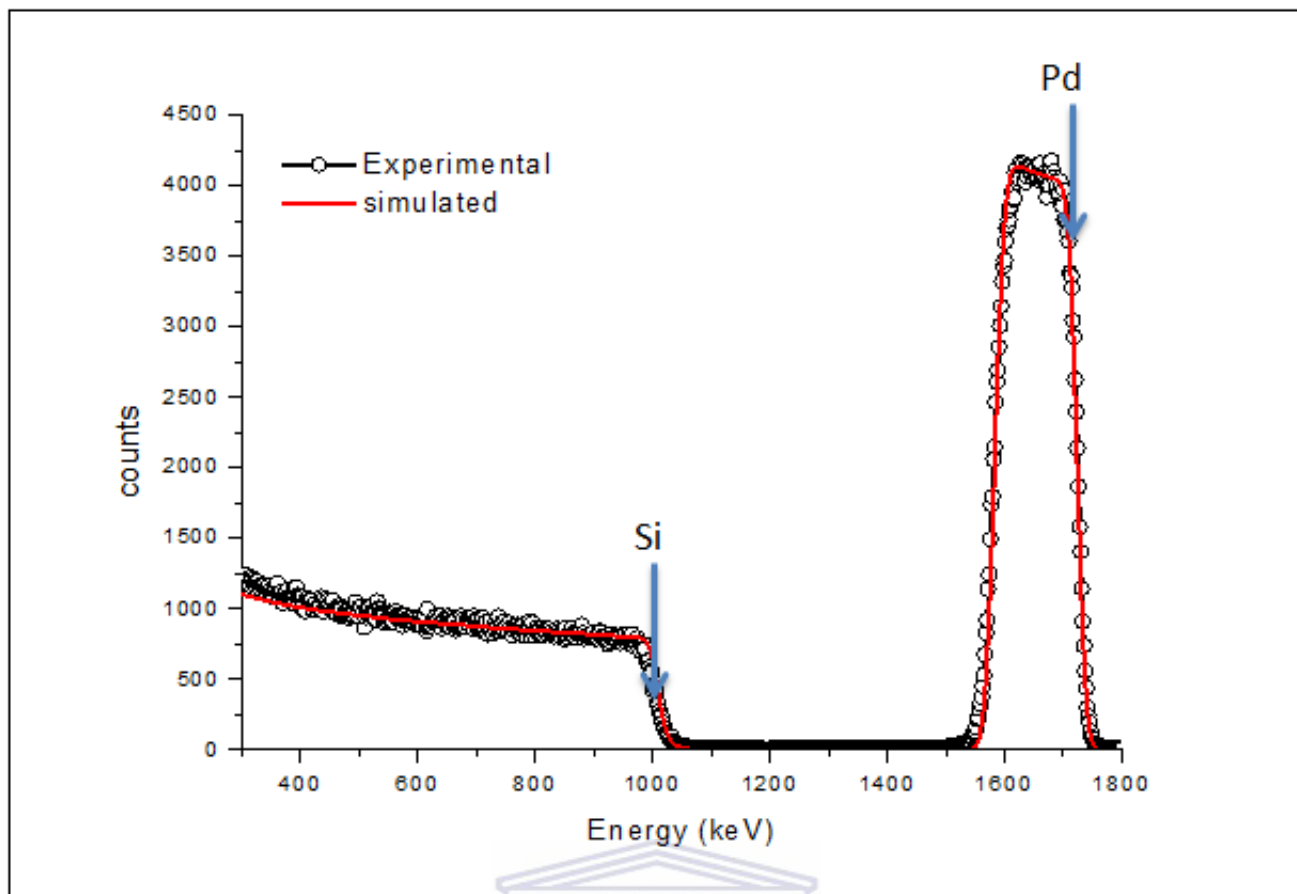
Figure 3.9: Simulated RBS spectrum of Pd deposited on Si substrate with a known thickness of Pd.

3.6 Gravimetric method for determine hydrogen concentration

3.6.1 Introduction

Gravimetric method is based on weight measurement. It is used to determine the change in mass of the material before and after hydrogenation. It is one of the most commonly used method to measure concentration of hydrogen in metals.

3.6.2 Experimental setup

The mass of the samples before and hydrogenation were measured using sensitive electric digital balance shown in Figure 3.10, which can measure up to 10^{-5} g. The weighing pan of the digital balance is covered with glass enclosure, to prevent dust and air from entering the balance. The change in mass was converted to hydrogen concentration, details of the calculations of hydrogen

concentration using gravimetric method are shown in appendix B.
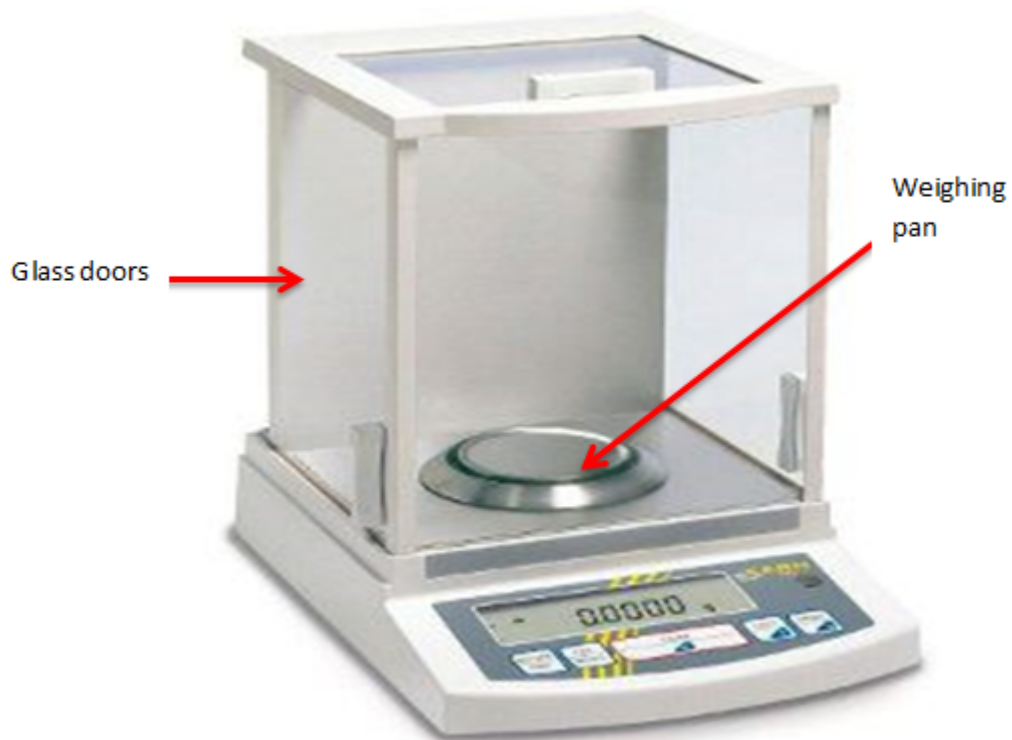
Figure 3.10: Electrical digital balance.

3.7 Optical Microscopy

Introduction

Optical microscopy is a widely used technique to investigate the microstructure of materials. Optical microscope uses visible light and series of lenses to produce a magnified image of the specimen. In this work optical microscope was used to investigate the microstructure of Ti and Ti6Al4V alloy before and after hydrogenation.

Image formation

The main components of an optical microscope include light source, objective lens, condenser lens and eyepiece. Consider a microscope consisting of two lenses (objective lens and eyepiece). Figure 3.11 is a ray diagram showing how an image is formed in a microscope. Light rays passing through the center of a lens are undeviated and those passing parallel to the axis of the lens pass through the conjugate focal point (f_o' and f_e') of the lens. The objective lens (OO) forms a real inverted image A'B', which acts as the object of the eyepiece. Eyepiece (EE) further magnifies the image, the eye observes a magnified virtual image A"B". In order to form a real magnified image of the specimen, the specimen must be between one and two focal length f_0.

Magnification of a single lens system is defined as ratio of image distance (distance over which the image is projected) to specimen distance (distance between the specimen and lens); $M = \frac{v}{u}$ where u, v is the specimen and image distance respectively. If a system contains more than one lens, then total magnification is the product of the magnification of all lenses.

$$M = M_1 \times M_2 \tag{3.15}$$

where M_1 is the magnification of the objective lens and M_2 is the magnification of the ocular.
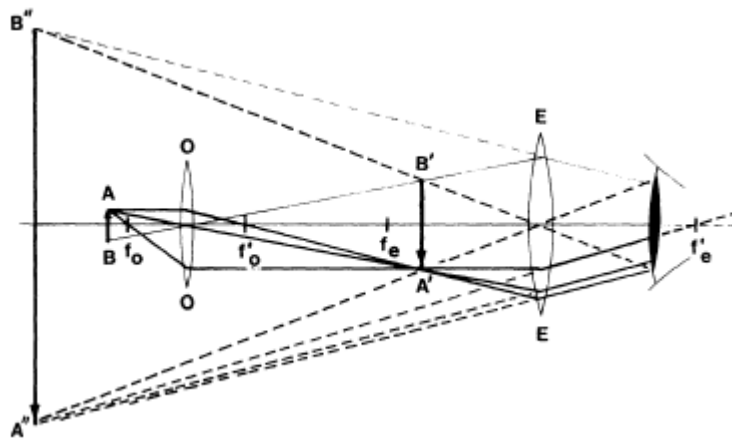
Figure 3.11: Ray diagram illustrating image formation in a compound microscope: f_o - focal point of the objective lens, $f'o$-conjugate focal point of the objective, f_e - focal point of the eyepiece, $f'e$-conjugate focal point of the eyepiece [3.7].

Illumination of the specimen

To get a high quality image in a microscope, the components of the microscope must be set correctly and the specimen must be properly illuminated. The method for specimen illumination in a microscope was first introduced in 1893 by August Kohler and is known as Kohler illumination. Kohler illumination is a standard illumination method used in modern light microscopes, it provides even illumination on the specimen. Figure 3.12 shows the schematic representation of Kohler illumination. The left hand diagram shows ray paths of illuminating light, the right hand side shows image formation light rays. Kohler lens known as the collector lens collects light from the light source and focuses it onto the diaphragm of the condenser lens. Light from the condenser lens passes through the object plane as pencils of parallel rays. Simultaneously the condenser lens forms the image of the field stop in the object plane.

Field stop controls the diameter of the cone of illumination light, thus limiting the resolution of the system, so that specimen is evenly illuminated by parallel light.

There are different types of modes including bright field, dark field, phase contrast microscopy and polarized light microscopy. Bright field and dark field microscopy are the most commonly used. In bright field microscopy specimen is evenly illuminated by a light source (specimen is placed on the sample stage and light is focused at a lens below the specimen), a dark image against a bright background is formed. In dark field microscopy specimen is illuminated by oblique light rays, usually a dark disk is placed below the condenser lens to produce a hallow cone of light.

Image is formed by light diffracted or reflected into the objective lens, and bright image against a dark background is formed.
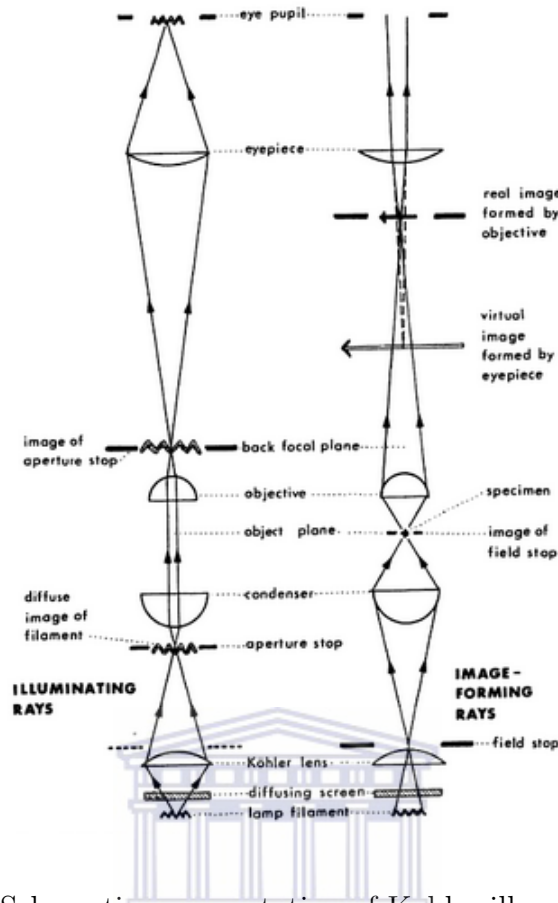
Figure 3.12: Schematic representation of Kohler illumination [3.8].

Resolution

Another important aspect in a microscope is its resolution, which is defined as the smallest separation of two points that are visible at distinct entities. Resolution can be presented mathematically by Abbe's equation.

$$d = \frac{0.612\lambda}{\mu \sin \alpha} \tag{3.16}$$

where d is limit of resolution resolution, λ is the wavelength of electrons, μ is the index of refraction of medium between point source and lens, relative to free space, α is the aperture angle [3.9].

Depth of field

Depth of field (h) of an optical system refers to the range of positions that are in focus in the specimen (no difference in the sharpness of the image). An image is in focus if an object lies in a plane with a certain distance from the objective lens. If an object is within the range h as shown in Figure 3.13, there is no difference in the sharpness of the image.
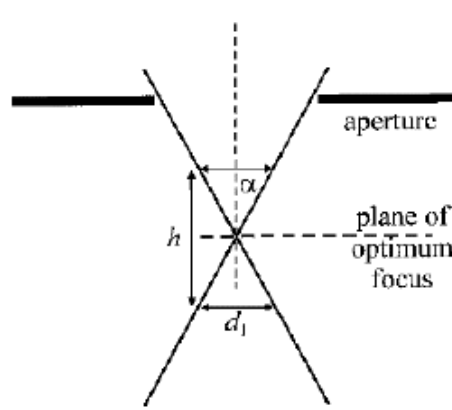
Figure 3.13: Rays converging at a specimen showing relation between depth of field h, convergence angle α and spot diameter d_1 [3.9].

Depth of field h can be calculated from Figure 3.13 as

$$h = \frac{0.61\lambda}{\mu \sin \alpha \tan \alpha} \qquad (3.17)$$

where μ is the index of refraction of medium between point source and lens, relative to free space, α is the convergence angle and λ is the wavelength of electrons. According to equation 3.17, to increase the depth field, the convergence angle α must be decreased. While increasing the depth of field leads to a worse resolution.

Experimental setup

A Reichert Me F3 light microscope was used to investigate the microstructure of Ti and Ti6Al4V samples before and after hydrogenation. Images were taken in a bright field mode at different magnifications.

3.7.1 High resolution scanning electron microscopy

Introduction

Scanning electron microscopy is one of the versatile methods for analysis of morphological characteristics and chemical composition of solid materials. A focused electron beam is used to scan the surface of the material to create an image. As the beam scans through the surface of the sample various signals are generated which are then used to obtain information about morphology and composition of the sample [3.9]. In this project scanning electron microscopy was used to investigate the effect of hydrogen on the morphology and composition of the phases formed in the Pd coated and bulk samples.

Components of a scanning electron microscope

Scanning electron microscope consists of four main parts: source of electrons (usually a tungsten filament emission type), column down by which electrons travel, electron detector and computer to display images. Electron column consists of a electron gun and electromagnetic lenses operating under vacuum. Figure 3.14 shows electron column of scanning electron microscope. Electron gun on top of the electron column thermionicaly emits electrons which are accelerated to an energy in the range of 1-30 keV.

The diameter of the electron beam emitted by electron gun is too large, so the electron lenses (condenser lenses) are used to reduce the diameter of the beam. The objective lens further de-magnifies and focuses the electron beam into the small area in the specimen. The focused electron beam is deflected by scanning coils so that it scans on the specimen across the x or y-axis and generate signals which are detected by the secondary electron detector.
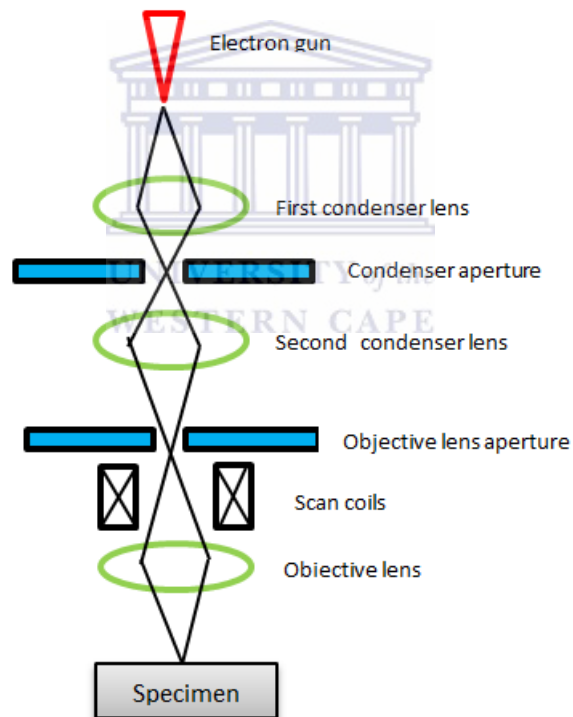
Figure 3.14: Schematic of scanning electron microscope column.

Interaction of electron beam with the specimen

Various types of signals are generated when the electron beam interacts with specimen. These signals are used to obtain information on morphology and composition of the sample. Generated signals include secondary electrons, X-rays, backscattered electrons and Auger electrons as shown schematically in Figure 3.15.
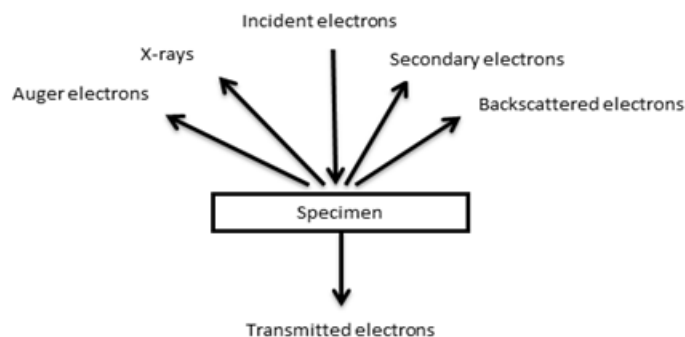
Figure 3.15: Specimen-beam interaction generating several types of signals [3.9].

Secondary electron signal is the most widely used signal in scanning electron microscopy to generate image. When the primary beam is incident on the sample surface causing ionization of the specimen atoms. Electrons emitted as a result of this ionization are called secondary electrons. They have energy less than 50 eV and escape from regions within few nm of the specimen. Secondary electron signal can resolve surface down to 10 nm and better, and provides information about the surface structure of the material

Backscattered electrons undergo single or multiple scattering events and escape from the surface with an energy greater than 50 eV. Its resolving power is about 1.0 μm. Backscattered electron signal provides information about composition and topography of the sample.

Auger electrons have low energy and escape only from regions within few nm of the specimen. The signal obtained can be used to determine the surface composition. Characteristics X-rays are used determine elemental composition of the specimen.

Resolution of scanning electron microscope

Since light has shorter wavelength than electron, the electron microscope has higher resolution that light microscope. Resolution is defined as the smallest separation of two points that are

46

visible at distinct entities. Limit resolution can be described mathematically by Abbe's equation (equation 3.16).

Depth of field (DOF)

Depth of field is the part of the SEM image that appears in focus. It is influenced by working distance which is defined as the distance between condenser lens and the specimen.

Effect of working distance on depth of field is shown in Figure 3.16. When a short working distance is used the specimen is scanned at wider angle α of electron producing an image with a small depth of field, at a longer working distance sample is scanned with a narrow angle of electrons resulting in an image with a large depth of field. In order to get an image with a large depth of field, the working distance must be increased or the aperture size decreased.
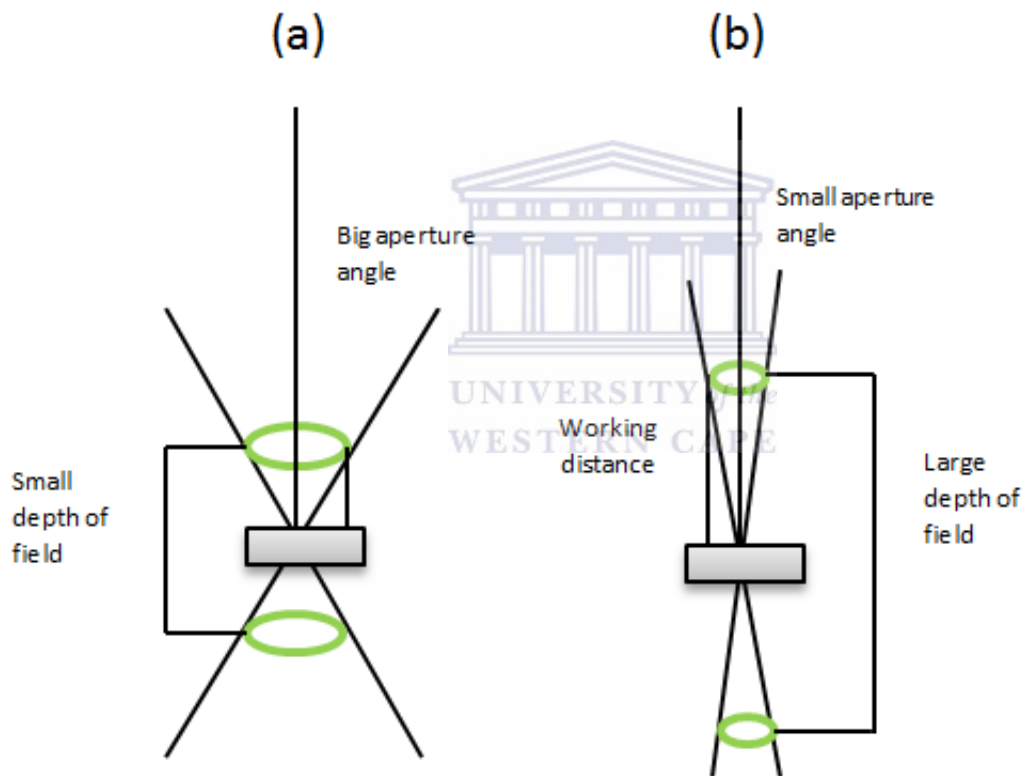
Figure 3.16: Influence of working distance on depth field: (a) short working distance causing little depth of field, (b) longer working distance causing larger depth of field [3.9].

Energy dispersive spectrometry

EDS is a technique used for determining elemental composition in the specimen. Figure 3.17 shows production of an X-ray by an atom. When the primary beam electron ejects the inner shell electron of an atom in the specimen, it leaves it in an excited state. If an electron from K shell is ejected, an electron from the outer shell electron L make transition to fill the vacancy in the inner shell K. An X-ray whose energy $(E_{K\alpha})$ is the difference between the energy of the outer shell electron and energy of the inner shell electron is emitted. X-rays emitted are characteristic of each element in the sample. EDS employs detection and separation of X-rays according to their energies. A silicon or germanium semiconductor detector is used for this purpose.
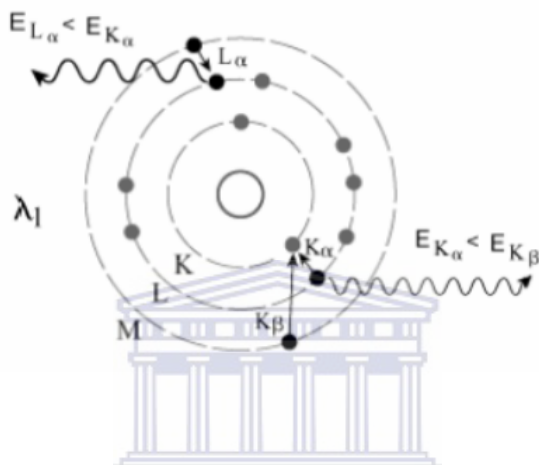
Figure 3.17: Emission of characteristic X-ray by an atom [3.9].

Each X-ray entering the detector excites a number of electrons into the conduction band of silicon, resulting in the equal number of positively charged holes in the outer shell electrons. The energy of the X-ray generated is proportional to the electron hole pairs generated. The detected X-rays produce a pulse which is amplified and passed to multichannel analyzer, which sort and count the number of X-rays received thus producing EDS spectra.

Experimental Setup

High resolution scanning electron microscopy was performed at the University of the Western Cape using Auriga Zeiss instrument with Gemini technology. An accelerating voltage of 1 kV was used at a working distance of between 4 mm and 6 mm. High resolution electron microscopy images were taken using secondary electrons. Energy dispersive spectrometry was conducted using Si semiconductor detector coupled to Auriga Zeiss instrument. This detector absorbs characteristic X-rays used to determine elemental composition of the material.

3.7.2 X-ray diffraction analysis

Introduction

X-ray diffraction technique is a versatile method used for determination of crystal structure, phase identification as well as measuring the particle size of the material. X-rays are electromagnetic radiation behaving the same way as light, but have shorter wavelength than that of light. Wavelength of X-rays varies between 0.5 and 2.5 $\mathring{A}$ and that of light varies between 4000 and 6000 $\mathring{A}$ [3.10]. In this work X-ray diffraction technique was used for phase identification of CP-Ti, Ti6Al4V and Pd deposited on Ti6Al4V before and after hydrogenation.

Theory of X-ray diffraction

Geometry of crystals

A crystalline material consists of atoms arranged in a period pattern in three dimensions. Consider a set of imaginary points with a fixed position in space relative to the atoms of a crystal. The set of points constitute a point lattice as shown in Figure 3.18 (a).
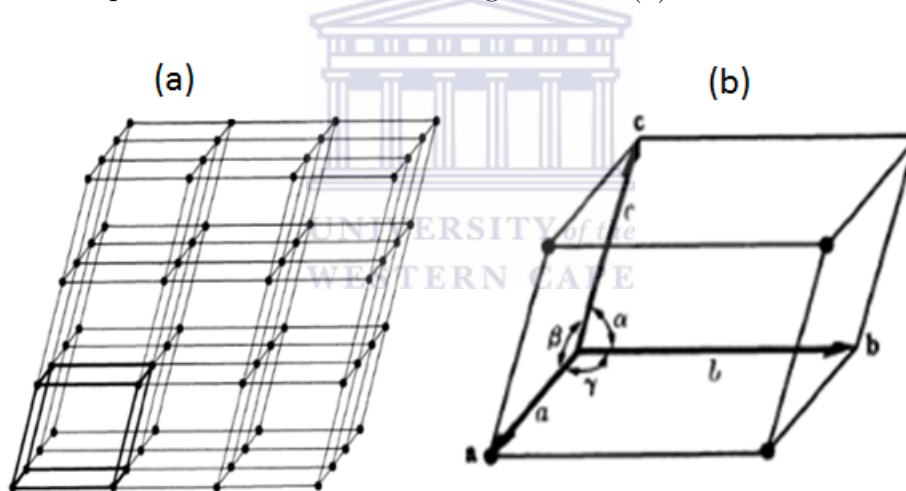
Figure 3.18: (a) Representative of a point lattice and (b) Representation of a unit cell [3.10].

A single cube in a point lattice forms a unit cell as shown in Figure 3.18 (b) where its size and shape can be described by three vectors a, b, c drawn from one corner of the unit cell taken as origin and three angles α, β, γ. The angles and vectors are called the lattice parameters.

Therefore the unit cell is the building block of the crystal structure. Unit cells with various shapes can be produced by giving special values to the vectors a, b, c and angles α, β, γ. There are 14 possible point lattices (Bravais lattices) as described in Table 3.6.

Table 3.6: Crystal system and Bravais lattices [3.10].

System	Axial lengths and angles	Bravais lattice	Lattice Symbol
Cubic	Three equal axes at right angles $a = b = c, \alpha = \beta = \gamma = 90^0$	Simple	P
		Body-centered	I
		Face centered	F
Tetragonal	Three equal axes at right angles, two equal $a = b \neq c, \alpha = \beta = \gamma = 90^0$	Simple	P
		Body-centered	I
Orthorombic	Three unequal axes at right angles $a \neq b \neq c, \alpha = \beta = \gamma = 90^0$	Simple	P
		Body-centered	I
		Base-centered	C
		Face-cenetered	F
Rhombohedral	Three equal axes at right angles, equally inclined $a = b = c, \alpha = \beta = \gamma \neq 90^0$	Simple	R
Hexagonal	Two equal coplanar axes at 120^0, third axis at right angles $a = b \neq c, \alpha = \beta = 90^0, \gamma = 120^0$	Simple	R
Monoclinic	Three unequal axes, one pair not at right angles $a \neq b \neq c, \alpha = \gamma = 90^0 \neq \beta$	Simple	P
		Base-centered	C
Triclinic	Three unequal axes, unequally inclined and none at right angles $a = b \neq c, \alpha \neq \beta \neq \gamma \neq 90^0$	Simple	F

Absorption of X-rays

Electromagnetic radiation can be considered as both a wave motion and a stream of particles called photons. As a wave, beam of X-rays carries energy and the rate of flow of this energy per unit area is called is called intensity. Looking at its particle nature, each photon has an energy $h\nu$, where h is Planck's constant and ν the frequency. X-rays are partly transmitted and absorbed upon interaction with the target material, thus causing a decrease in the intensity. A decrease in intensity of the X-ray beam as it penetrates through the material to a depth x can be represented by the following equation

$$\frac{-dI}{I} = \mu dx \qquad (3.18)$$

50

where μ is the linear absorption coefficient. By integrating equation 3.18 the intensity I_x of the transmitted beam through a thickness x can be written as

$$I_x = I_0 e^{-\mu x} \tag{3.19}$$

where I_0 is the intensity of the incident beam.

Bragg's law

When a beam of parallel, monochromatic X-rays with wavelength of λ is incident on crystal at an angle θ, as shown in Figure 3.19, scattered X-rays undergo interference. Diffraction of electromagnetic radiation occurs only when there is constructive interference.
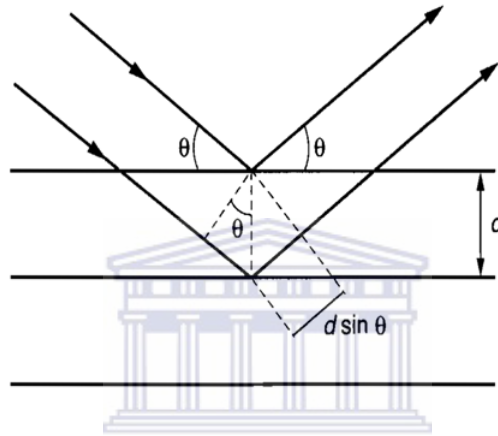
Figure 3.19: Illustration of Bragg's law, constructive interference of X-rays [3.10].

Constructive interference occurs when the path length in the crystal $(2d\sin\theta)$ is a multiple of the wavelength. This can be expressed mathematically by Bragg's equation:

$$n\lambda = 2d\sin\theta \tag{3.20}$$

where n is the order of reflection (n = 1,2,3..), λ is the wavelength, d is the distance between the lattice planes, θ is the angle between the incident beam and the lattice plane (interplaner spacing).

Experimental setup

In this project XRD was carried out using AX5 D8 advance X-rays diffractometer at iThemba LABS. The schematic of an X-ray diffractometer is shown in Figure 3.20. It consists of an X-ray source T, two circle ganiometer (θ and 2θ circles) and detector D
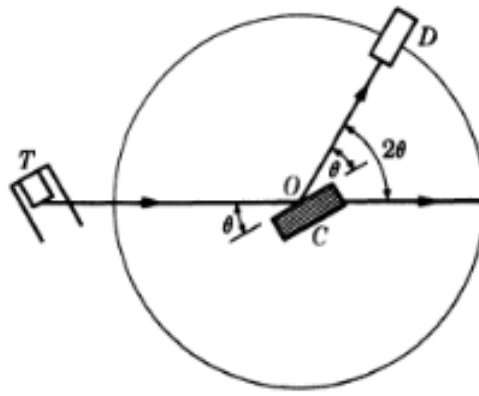
Figure 3.20: Schematic of X-ray diffractometer [3.10].

X-rays coming from the X-ray source T are incident on a target sample C. The sample can be rotated about an axis through O, the center of the diffractometer. The detector D is used to measure the intensity of the diffracted beam. During the measurement the sample is placed at angle θ and the detector is set to the corresponding angle 2θ. Table 3.7 gives a summary of experimental parameters used in the measurements performed in this study.

Table 3.7: Measurement details

voltage	40 kV
current	40 mA
scan range (2θ)	$0 - 90\,^\circ$
scanning rate	$2\,^\circ/\text{min}$
step size	3.2 seconds
source of x-rays	copper tube with CuK_α radiation

References

[3.1] G.F. Vander Voort, *Metallography principles and practice*, ASM International (1984).

[3.2] B.L. Doyle, D.K. Brice, The analysis of elastic recoil detection data, *Nuclear Instruments and Methods in Physics Research B*, **35**, 301-308 (1988).

[3.3] W.M.A. Bilk, F.H.P.M. Habraken, Elastic recoil detection, *Reports on Progress in Physics*, **56**, 859-902 (1993).

[3.4] M, Nastasi, J.W. Mayer, Y. Wang, *Ion bean analysis: Fundamentals and applications*, Taylor and Francis (2014).

[3.5] M, Mayer, *SIMNRA user's guide*, Max-Planck institute fur plasmaphysik (2011).

[3.6] W. Chu and J.W. Mayer, M. Nicolet, *Backscattering spectrometry*, Academic Press (1978).

[3.7] R. Haynes, *Optical microscopy of materials*, Blackie and Son (1984).

[3.8] M. Spencer, *Fundamentals of light microscopy*, Cambridge University Press (1982).

[3.9] P.J. Goodhew, F.J. Humphreys, *Electron microscopy and analysis*, Taylor and Francis (1988).

[3.10] B.D. Cullity, *Elements of X-ray diffraction*, Addison-Wesley Publishing Company (1965).

[3.11] M. Mayer, Ion beam analysis of rough films, *Nuclear Instruments and Methods in Physics Research B* **194**, 177-186 (2002).

Chapter 4

Results and Discussions

4.1 Introduction

The ability of metallic materials to absorb the hydrogen and to be used as potential materials for hydrogen storage was investigated in three systems: (i) commercially pure Titanium (CP-Ti), (ii) Ti6Al4V alloy, and (iii) Pd coated Ti6Al4V alloy. The samples were hydrogenated in 15 % H/Ar gas mixture at room and elevated temperatures (450 °C, 550 °C and 650 °C). The hydrogenation process was conducted at 1 bar pressure for a duration of 3 hours. The amount of absorbed hydrogen was measured using gravimetric method and elastic recoiled data analysis (ERDA). Hydrogen depth profile was determined using ERDA technique. The phase change and possible metallic hydrides formation were investigated by X-ray diffraction while the optical microscopy was used to study the changes in microstructure caused by hydrogen absorption. In addition, the changes in coating and its stoichiometry caused by hydrogenation treatment were investigated by Rutherford backscattering spectroscopy (RBS) while coating morphology was studied using scanning electron microscopy (HRSEM/EDS). The results obtained by these characterization techniques are presented for each system separately, as follows:

A) Section 4.2 presents the results and discussion for CP-Ti

B) In section 4.3 the results obtained from Ti6Al4V are presented and discussed

C) Section 4.4 focuses on the results and discussions for Pd coated Ti6Al4V system.

The comparison between three metallic systems hydrogenated under same conditions is given in terms of their hydrogen storage capacity. The advantages, limitations and recommendations are discussed for each of investigated systems.

4.2 Hydrogen storage in CP-Ti

4.2.1 Hydrogenation study by elastic recoil detection analysis

The hydrogen profile of CP-Ti before hydrogenation and after hydrogenation at room and elevated temperatures determined by ERDA is shown in Figures 4.1-4.2. Figure 4.1 presents the hydrogen spectra of CP-Ti before hydrogenation, and after hydrogenation at room temperature and 450 °C. In the as-received CP-Ti sample only the surface hydrogen was observed. Ti can adsorb water and hydrocarbons in the surface during sample preparation (polishing and cleaning with water), which accounts for the hydrogen on the surface before hydrogenation. The average hydrogen concentration detected in as-received samples was 0.19 at.%. The hydrogen profile of CP- Ti samples hydrogenated at room temperature and 450 °C are similar to that of as received sample, this shows that there was no significant hydrogen absorption at room temperature and at 450 °C. Hydrogen concentrations of 0.2 at% and 0.25 at.% of hydrogen were absorbed at room temperature and at 450 °C respectively. In both cases hydrogen is mainly detected in the near surface regions, as can be seen in Figure 4.1.
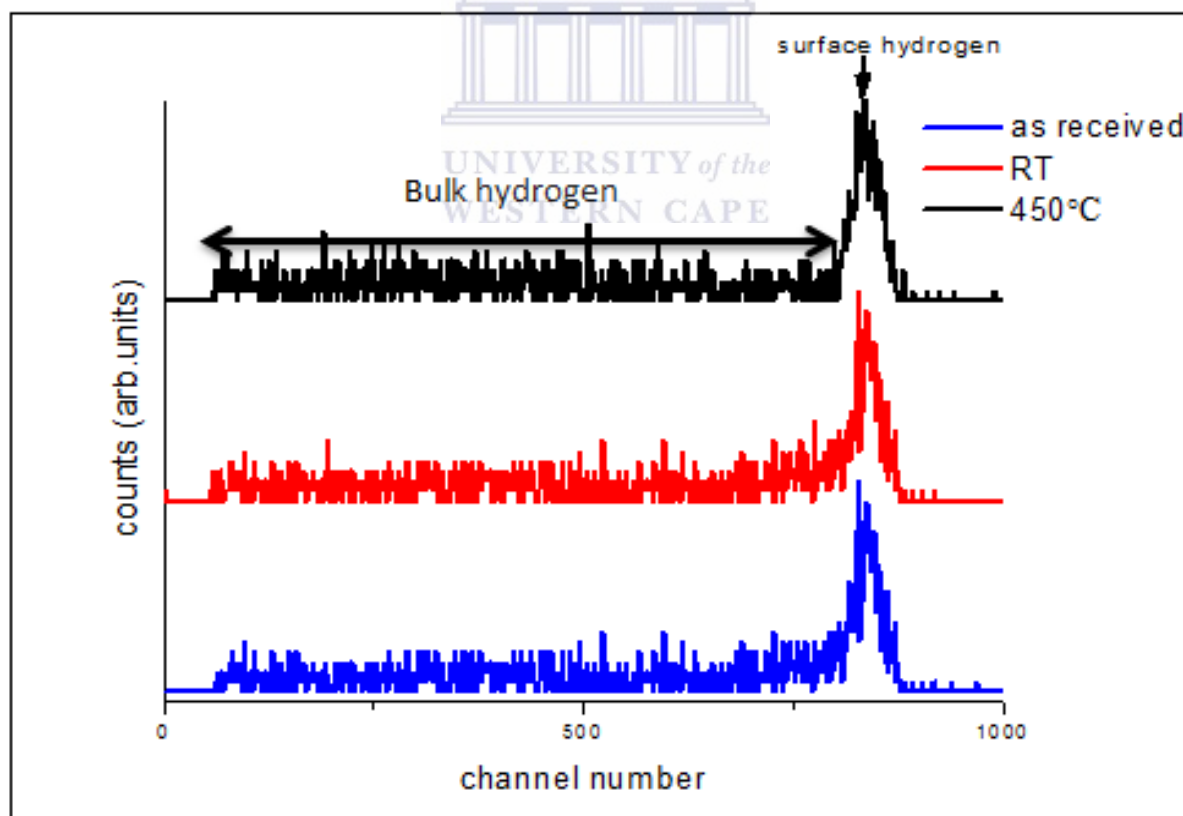
Figure 4.1: Hydrogen profile of CP-Ti before and after hydrogenation at room temperature and 450 °C for the duration of 3 hours each.

The amount of hydrogen absorbed at higher temperatures (550 °C and 650 °C) increased significantly, as seen Figure 4.2. The blue curve is a typical example of the simulated spectra. It was found that, an average concentration of 45.65 at.% of hydrogen was absorbed at 550 °C. This increase in absorbed hydrogen was observed in both the near-surface and the bulk regions. Higher temperature (650 °C) caused absorption of 37.53 at.% hydrogen. The presence of hydrogen was mainly detected in regions further down from surface.
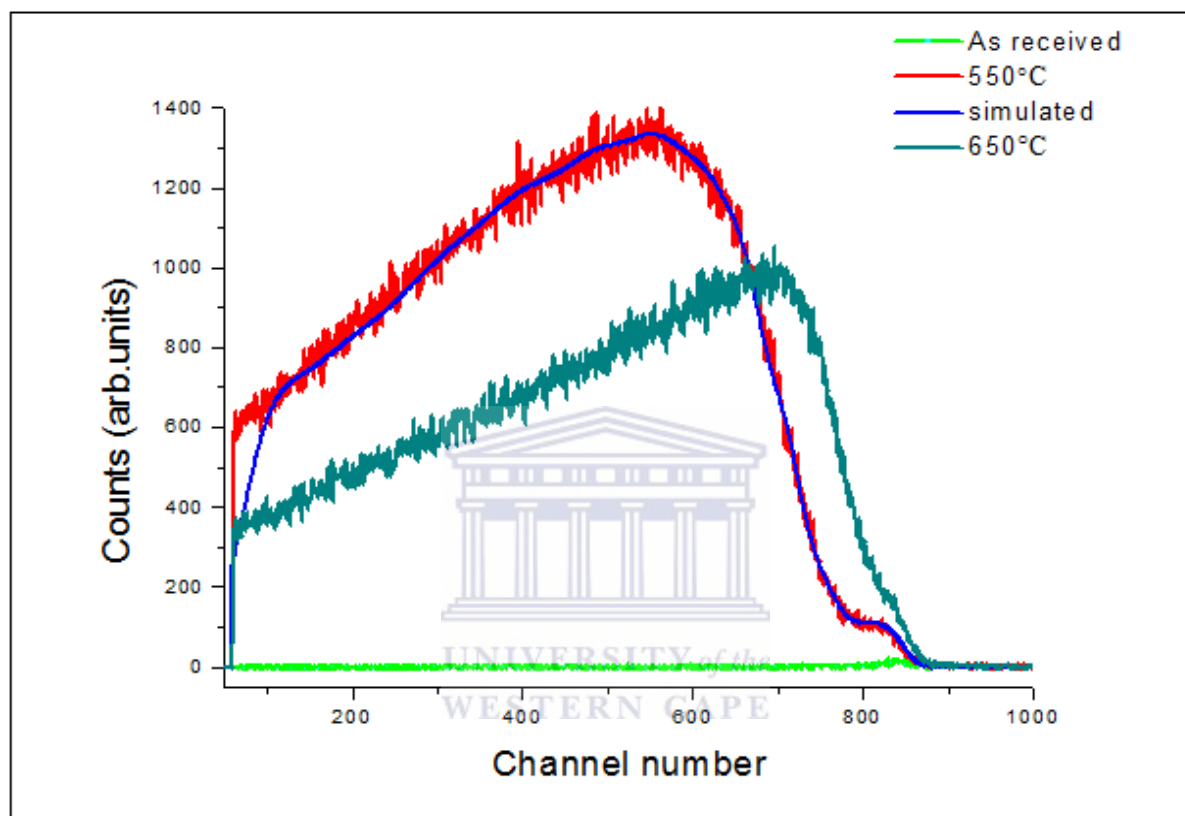
Figure 4.2: Hydrogen profile of CP-Ti before hydrogenation and after hydrogenation at 550 °C and 650 °C for a period of 3 hours.

Hydrogen depth profiles of as received CP-Ti and samples hydrogenated at 550 °C and 650 °C extracted from Figure 4.2 are shown in Figure 4.3. The surface hydrogen was profiled within a depth of 0.02 μm, but traces of hydrogen in the bulk region were recorded up to 0.68 μm. A concentration of 0.14 at.% of hydrogen is evenly distributed in bulk region (0.02 - 0.68 μm). Since the hydrogen profile of the as received sample, and sample hydrogenated at room temperature and 450 °C are almost the same, only the as received sample is presented. After hydrogenation at 550 °C and 650 °C hydrogen depth coverage was increased to 1.12 μm. In the sample hydrogenated at 550 °C, the hydrogen surface peak was simulated to be around 0.1 μm. The concentration of

hydrogen increases with increasing depth up to a thickness of 0.57 μm, whereas from 0.57 to 1.12 μm it is found evenly distributed. At 650 °C, below a surface region simulated to be around 0.01 μm. The amount of absorbed hydrogen increased up to a depth of 0.3 μm, thereafter the concentration of hydrogen is distributed uniformly. After considering the energy losses in the deepest layer reported in this thesis, we calculated at least more than 1000 keV left on exiting Ti layer. This means that, there would still be energy available for detection even if an extra foil was placed in front of ERD/RBS detector.
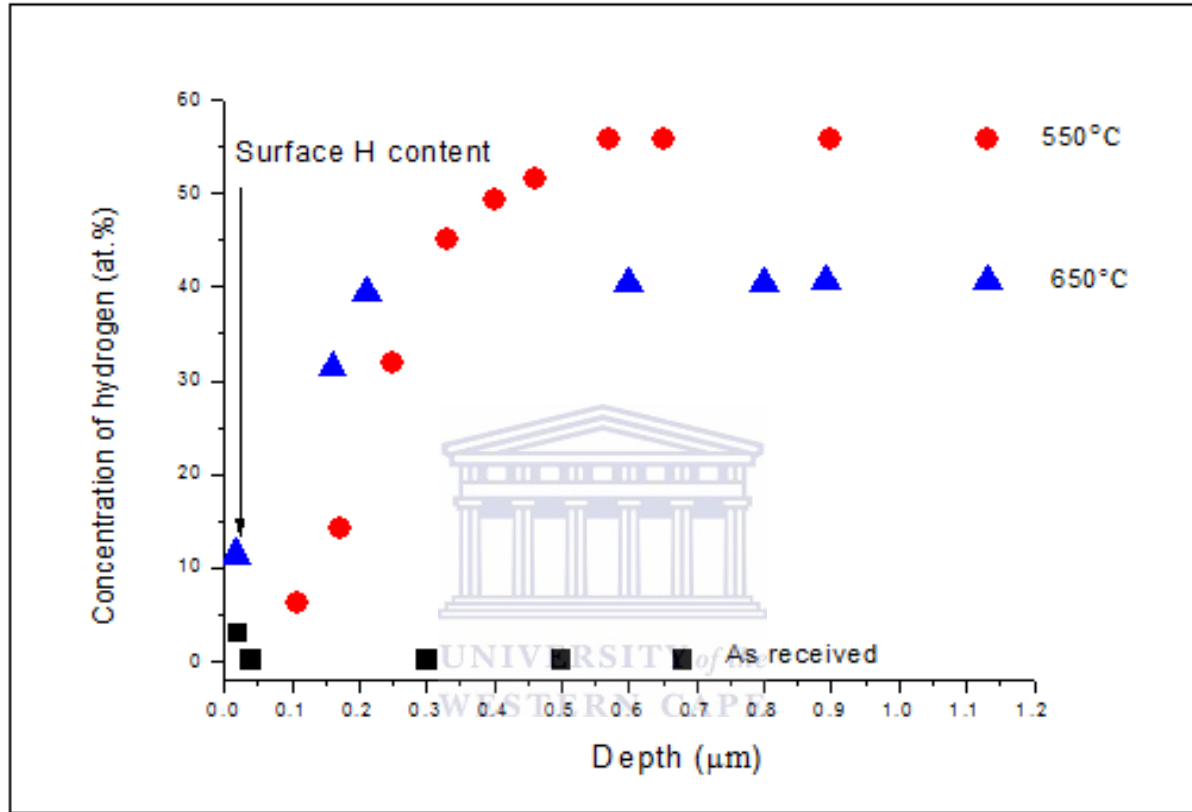
Figure 4.3: Depth profile of absorbed hydrogen in CP-Ti.

In summary, the hydrogen absorption by CP-Ti is very limited at room temperature hydrogenation conditions. Similar behavior was observed at 450 °C. The amount of absorbed hydrogen increased at 550 °C and then decreases at 650 °C, as shown in Figure 4.4.
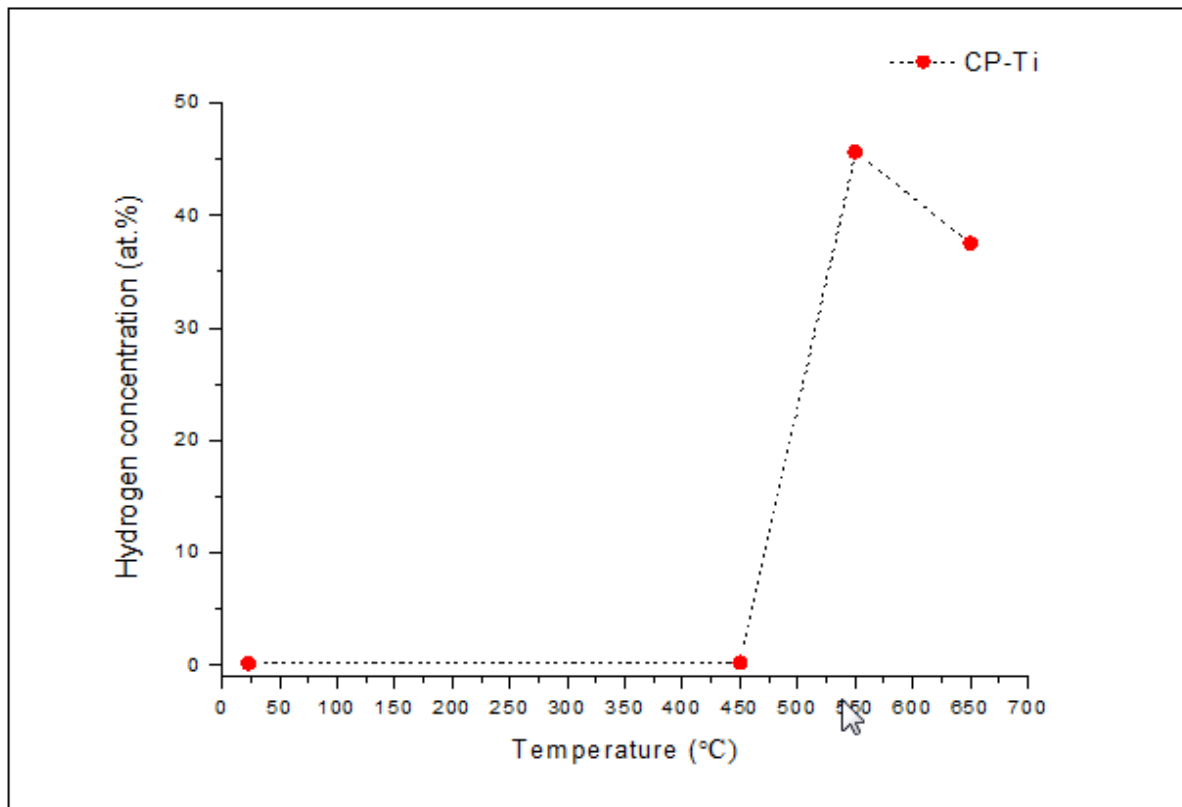
Figure 4.4: Concentration of hydrogen in CP-Ti as a function of hydrogenation temperature.

4.2.2 Hydrogenation study by mass gain measurements (gravimetric method)
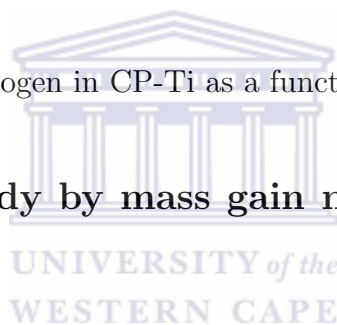
The weight changes caused by hydrogen absorption are measured using gravimetric method and the results are given in Table 4.1. Detailed calculations are presented in Appendix-B. The measurements show that there are no changes in the sample masses when they were hydrogenated at room temperature. This indicates that low solubility of hydrogen in CP-Ti at room temperature conditions. However, the concentration of hydrogen increased to 5.41 at.% a and 45.77 at.% for samples hydrogenated at 450 °C, 550 °C respectively. For hydrogenation at higher temperature of 650 °C, 38.60 at.% of hydrogen was determined. It should be pointed out that the mass gain measurements can be taken with certain degree of reservation, due to possible oxidation of the samples. The scale of oxidation affects the sample' s weight and thus, the mass measurements. In general, the gravimetric results show that hydrogenation temperature affects the hydrogen absorption in CP-Ti; the hydrogen absorption increased at temperatures of 550 °C while at higher temperature (650 °C) the hydrogen concentration decreases.

58

Table 4.1: Calculated hydrogen concentration of CP-Ti by gravimetric method.

Hydrogenation temperature (°C)	wt%H	at%H
As received (untreated)	0.00	0.00
Room temperature	0.00	0.00
450	0.13	5.41
550	1.75	45.77
650	1.31	38.59

The hydrogen concentration decrease at 650 °C might be due to the following reasons: (i) decrease in solubility of hydrogen at higher temperatures, (ii) formation of a thick oxide layer and its stoichiometry which could serve to block and prevent hydrogen absorption into the metal, (iii) release of hydrogen from the bulk caused by high temperature. Considering the integrity of oxide layer, the mechanical degradations such as cracking, delamination or spalling were not observed at any of investigated samples.

4.2.3 Comparison between hydrogen concentration determined by ERDA and gravimetric method

The results obtained by comparative study using gravimetric and ERDA methods are summarized in Table 4.2. The percentage error of gravimetric measurement is 0.5%, while that of ERDA measurements was calculated to be 7.5%. As seen, the hydrogen concentrations obtained by two methods do not agree with each other in the cases of low amount of absorbed hydrogen, such as in CP-Ti hydrogenated at room temperature and 450 °C. There was no mass gained in the sample hydrogenated at room temperature, which might indicate that no hydrogen absorption occurred. However hydrogen was detected by ERDA. At 450 °C the value measured by gravimetric method is higher than the value measured by ERDA, while the values obtained for 550 °C and 650 °C are in good agreement. Discrepancy in the hydrogen amount absorbed in CP-Ti samples treated under different conditions as obtained by two methods, is due to inability to measure small changes in the sample mass by gravimetric method. Also, the effects of the oxide layer on the total mass cannot be avoided when someone use gravimetric method.

Table 4.2: Concentration of hydrogen determined by gravimetric method and ERDA

Hydrogenation temperature (°C)	H conc (at.%) (gravimetric method)	H conc(at.%) (ERDA)
RT	0.00	0.20
450	5.41	0.25
550	45.77	45.65
650	38.59	37.53

The RBS results on thickness and chemical composition of oxide layer are shown in the following section.

4.2.4   Oxidation study by Rutherford Backscattering spectrometry

Rutherford backscattering spectrometry (RBS) was used to investigate the stoichiometry and the thickness of oxide layer which can possibly form during hydrogenation at elevated temperatures. It was of particular interest since it was observed that the samples changed their colour from metal silver to brownish, purple and blue after hydrogenation at, 450 °C, 550 °C, and 650 °C. It is widely published in the literature that titanium oxide layer can form naturally or be artificially induced high temperature exposition [4.2, 4.3]. The colour observed is related to oxide layer thickness. Velten et al [4.3] reported that purple and deep blue colours appear during thermal oxidation when the thickness of oxide layer was 25-40 nm and 40-50 nm respectively. RBS spectra of as-received (untreated sample) and hydrogenated at different temperatures for duration of 3 hours CP-Ti samples are shown in Figure 4.5.

The RBS results show no formation of oxide layer in the spectra of both as received and room temperature hydrogenated samples. However, it has been reported in literature that a thin oxide layer of approximately 2-7 nm naturally forms at room temperature [4.4]. This discrepancy might be explained by a formation of very thin oxide layer not detectable and/or by the fact that RBS is not the most appropriate technique for determination of thin oxide layers. RBS depth resolution is between 5 and 20 nm [4.5]. The possible option is to use another technique such as the oxygen resonant backscattering. However, RBS results show that oxide layers were formed at high temperatures (450 °C, 550 °C, and 650 °C) and their composition (TiO_2) and thickness of approximately (62 nm) were the same in all the cases. The thickness forms due to the oxygen present in gas mixture and possible deterioration of vacuum due to high temperature and/or vacuum leakage.
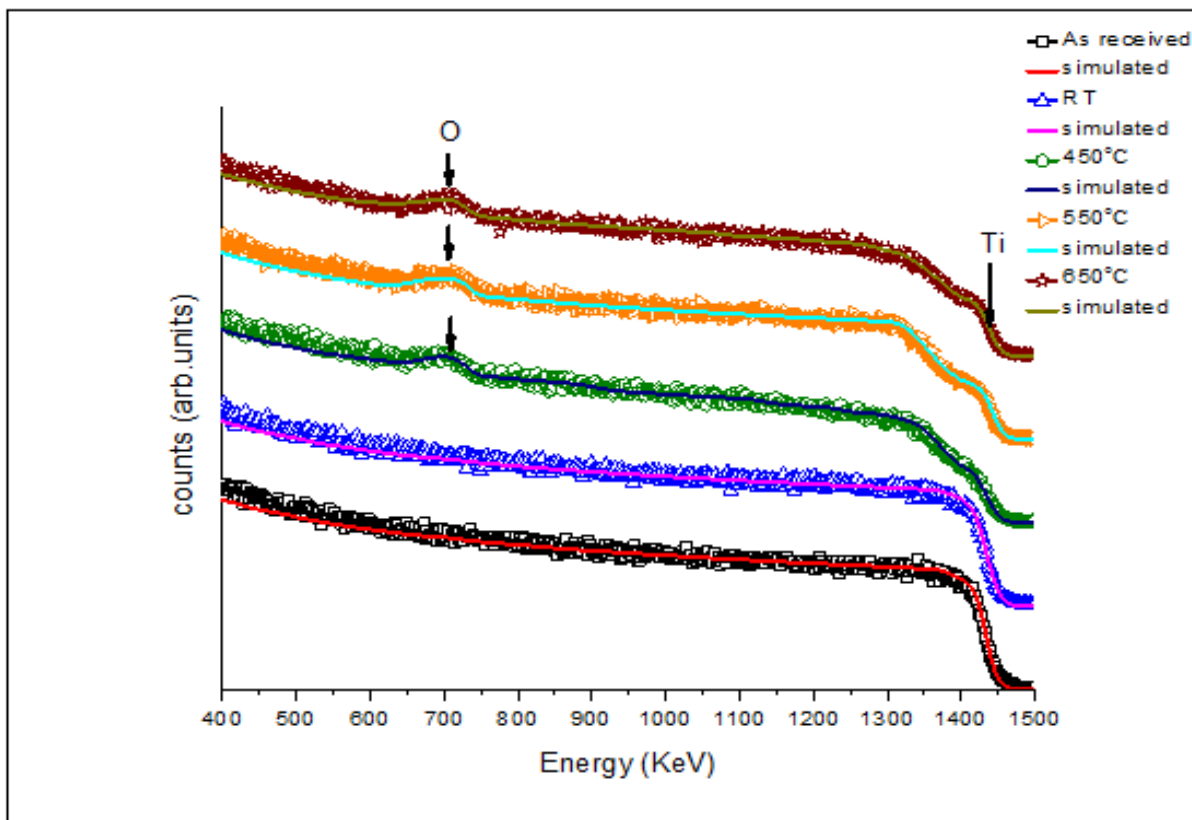
Figure 4.5: RBS spectra of CP-Ti samples investigated before and after hydrogenation at different temperatures for a period of 3 hours; the appended arrows indicate the positions of oxygen and titanium peaks.

Since the thickness of the oxide layer formed during hydrogenation was the same for all samples hydrogenated at 450 °C, 550 °C and 650 °C , it could be suggested that the oxide layer is not the reason for the decrease in hydrogen concentration at 650 °C. Based on this fact, it is reasonable to conclude that the solubility of hydrogen in CP-Ti decreases at high temperatures. Other factors such as hydrogen out diffusion, might contribute to the decrease in hydrogen solubility at high temperatures.

4.2.5 Microstructure of CP-Ti

The microstructural study was performed on as-received and the samples hydrogenated at room and elevated temperature. Particular attention was paid on the effect of hydrogen on the changes in grain size and possible formation of hydrides. Figure 4.6 shows the optical micrograph of as-received CP-Ti sample taken in cross-section. The microstructure consists of equaxed grains of α-phase with approximate size of 50 μm. An increase in annealing temperature gives rise to an increase in grain growth; the grain size increased to approximately 80 μm and 100 μm after

annealing at 550 °C and 650 °C respectively, as seen in Figure 4.7.
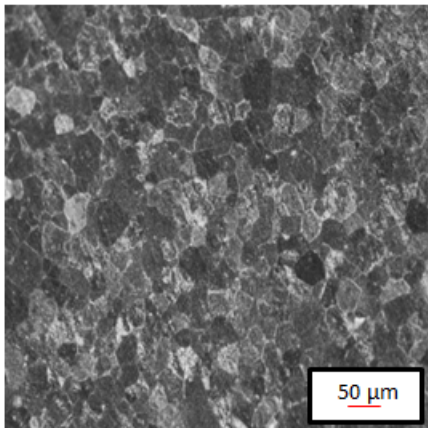
Figure 4.6: Optical microstructure of CP-Titanium as received (before hydrogenation) showing the presence of α-phase grains.
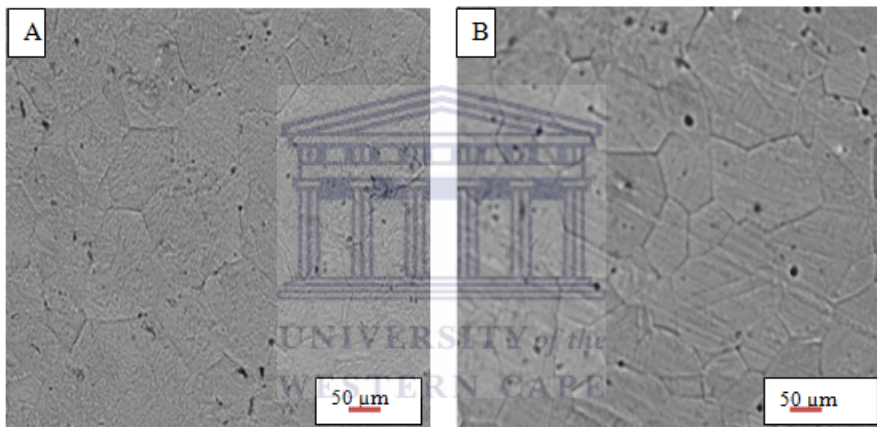
Figure 4.7: Optical micrographs of as-received CP-Ti samples annealed at high temperature for a period of 3 hours : (A) 550 °C and (B) 650 °C. Grain growth was observed at both temperatures.

The changes in microstructure caused by hydrogenation is shown in Figure 4.8-4.9. Figure 4.8 shows the micrographs of CP-Ti after hydrogenation at (A) room temperature, (B) 450 °C, (C) 550 °C, and (D) 650 °C. Comparison shows that the grain size did not changed by hydrogenation at room temperature and 450 °C, as illustrated by Figure 4.8 (A- B). This indicates that the amount of absorbed hydrogen or hydrogenation temperature (room temperature and 450 °C) was not sufficiently high to cause the changes in grain structure. However, the microstructure of CP-Ti samples hydrogenated at higher temperatures (550 °C and 650 °C) changed substantially. The needle like structure was observed as illustrated in Figure 4.8(C-D). The micrographs taken at higher magnification are shown in Figure 4.9.
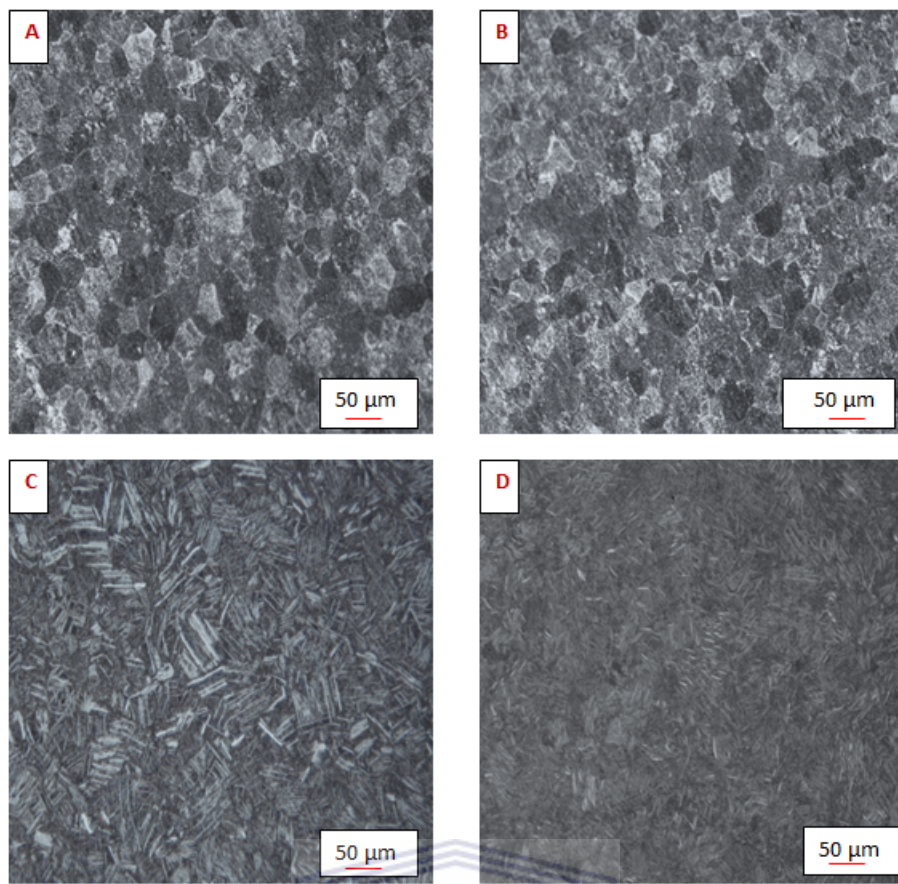
Figure 4.8: Optical micrographs showing the microstructural changes of CP-Ti hydrogenated at: (A) room temperature, (B) 450 °C, (C) 550 °C and (D) 650 °C.
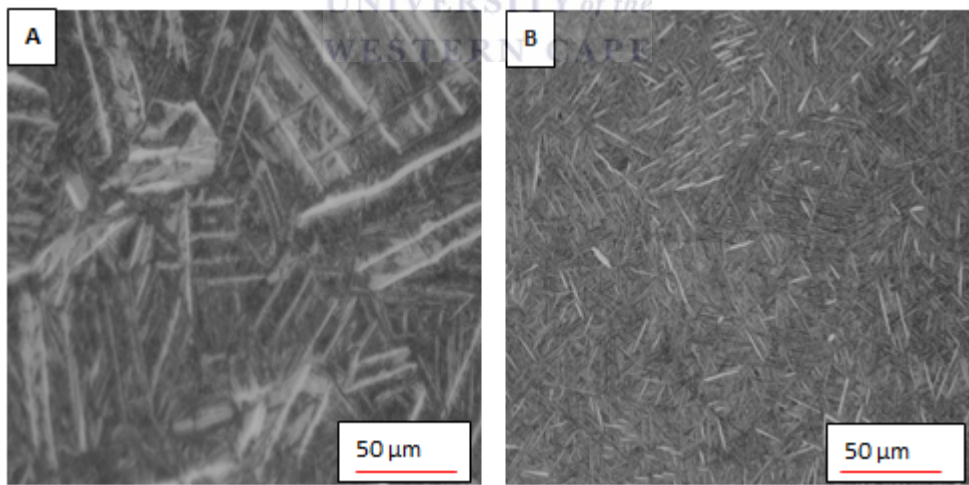
Figure 4.9: Optical micrographs of CP-Ti samples taken at higher magnification after hydrogenation at different temperatures : (A) 550 °C and (B) 650 °C showing needle like microstructure (α-lathes martensite).

63

The formation of large alpha needles is an indication that at some point in time during hydrogenation the CP-Ti became fully β-phase. Referring to the Ti-H binary phase diagram [4.6] the beta transus temperature is decreased from 800 to 300 °C when 40 at% hydrogen is added into the system. At 550 °C and 650 °C approximately 45.65 and 38 at.% hydrogen was absorbed, resulting in a decrease in beta phase transformation temperature. The CP-Ti was then furnace cooled to room temperature through/near eutectoid transition ($\beta \rightarrow \alpha + \delta$). Consequently, the microstructure that consists of large α lathes and δ (Titanium hydrates) forms. To confirm the presence of the titanium hydrides, the transmission electron microscopy (TEM) and/or EBSD (electron backscattering diffraction) should be conducted in future. A similar microstructure was reported by Shan et al [4.7], where they hydrogenated α-Ti alloy and the presence of the TiH_2 was confirmed in this study by TEM.

In summary, hydrogen absorption at 550 °C and 650 °C leads to formation of hydrides and needle α lathes martensite.

4.2.6 Phase transformation in CP-Ti

X-ray diffraction technique was used for phase analysis of hydrogenated samples. XRD patterns of CP-Ti before and after hydrogenation are presented in Figure 4.10. The XRD pattern of as-received sample shows the presence of α-Ti phase with lattice constants as: a, b= 2.95050 and c = 4.68260 Å. There was no change in the XRD patterns of the samples hydrogenated at room temperature and 450 °C. Only α- phase was observed. However, at high hydrogenation temperatures of 550 °C and 650 °C the formation of TiH_2 phase (δ hydride) was observed. The detected TiH_2 phase has an FCC structure and lattice constant a = 4.42 Å. The δ hydride phase forms in the composition range from $TiH_{1.15}$ to TiH_2 and has a CaF_2 type structure with titanium atoms randomly occupying tetrahedral interstitial sites [4.7]. It was also observed that the intensity of TiH_2 phase decreased in samples hydrogenated at 650 °C. This suggests that the volume fraction of TiH_2 phase decreases with increasing temperature. These results are in good agreement with ERDA results. This can be explained by the fact that hydrogen absorption decreases at high temperature or that hydrogen desorbed at this temperature and thus contributing to the decrease of the TiH_2 phase volume fraction.
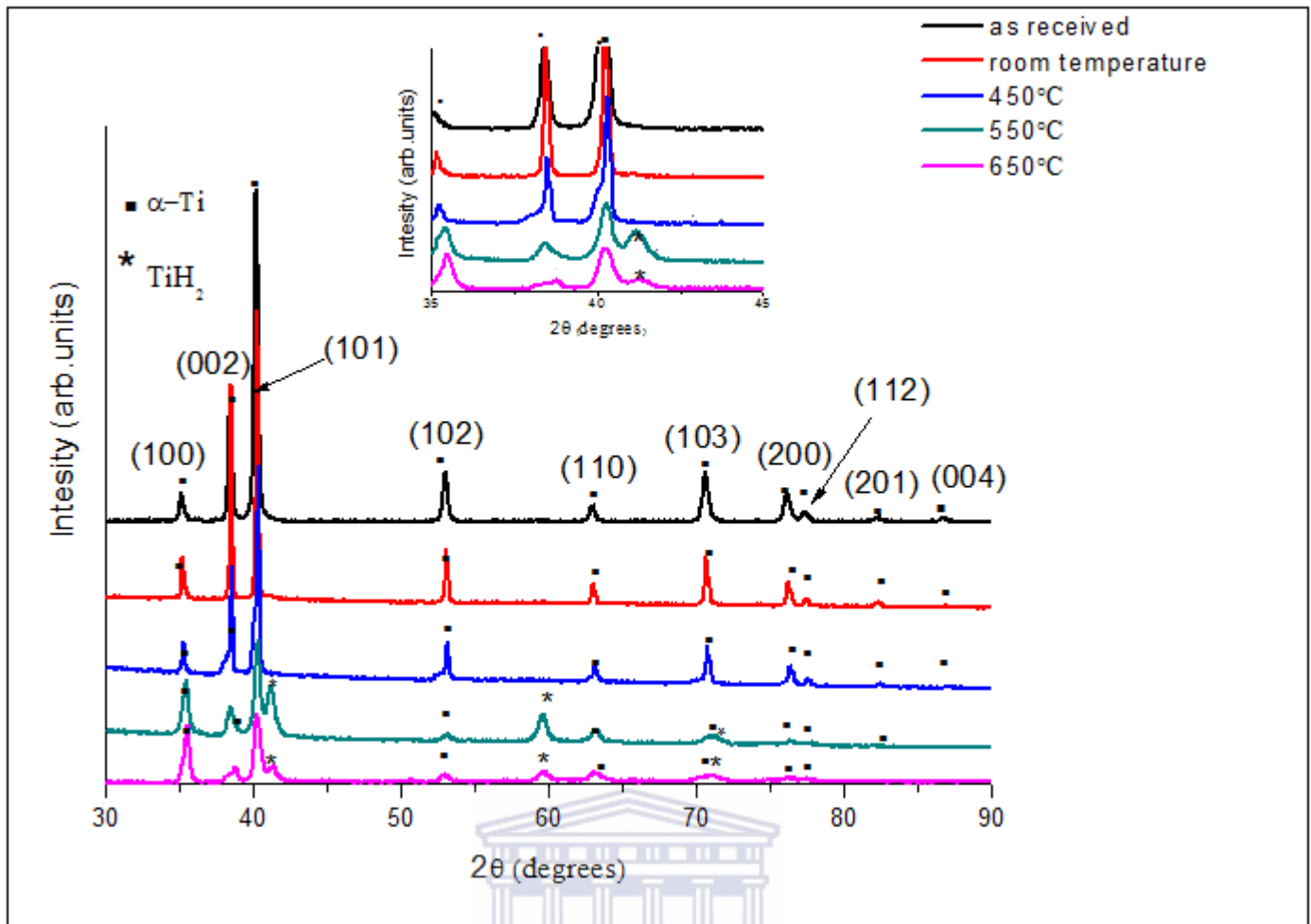
Figure 4.10: X-ray diffraction pattern of as received CP-Titanium and hydrogenated samples.

It was also observed that in samples hydrogenated at $550\,^{\circ}$C and $650\,^{\circ}$C, α-Ti peaks at $2\theta = 72\,^{\circ}$ and $76\,^{\circ}$ became broad (the peaks of α and δ-phases overlap with each other). Peak broadening can be caused by distortion of α-phase lattice [4.8]. The peaks of α-phase were shifted to high angles as it can be seen in Figure 4.10. This indicates the formation of tensile stresses induced by hydrogen absorption. The phases present and hydrogen concentration as a function of hydrogenation temperature are summarized in Table 4.3

In summary no hydride formation occurred at temperatures below $550\,^{\circ}$C. The TiH_2 phases were formed in the samples hydrogenated at $550\,^{\circ}$C and $650\,^{\circ}$C .

4.2.7   Discussion of results for CP-Ti

The results in this study show that hydrogenation temperature affects hydrogen storage capacity of CP-Ti. Based on the results obtained by ERDA and gravimetric method it was shown that no significant hydrogen absorption occurred during hydrogenation at room temperature and $450\,^{\circ}$C.

Table 4.3: Phases present after hydrogenation in CP-Ti at different temperatures

Temperature (°C)	concentration (at.%)	Phases present
room temperature	0.19	α
450	0.25	α
550	45.65	$\alpha + TiH_2$
650	37.53	$\alpha + TiH_2$

Hydrogen absorption began at temperatures of 550 °C, this result agrees with the result of Lopez et al. [4.9]. The concentration of hydrogen decreased when the sample was hydrogenated at 650 °C. The solubility of hydrogen in Ti decreases at higher temperatures. Similar observations have been reported by Murzinova et al [4.10] and Markelj et al [4.11]. In addition Murzinova et al [4.10] found that the solubility of hydrogen in the α- phase of titanium alloys decreases rapidly at temperatures above 750 °C in pure hydrogen environment. The reason for the decrease in solubility of hydrogen in Ti at high temperature is the nature of Ti-H reaction. The reaction between titanium and hydrogen is exothermic, during hydrogen absorption heat is released. As the temperature increases, the kinetic energy increases. The higher kinetic energy allows gas molecules to move freely and break the bonds between titanium and hydrogen atoms. Hydrogen atoms then diffuse from the bulk to the surface and desorb from the surface as molecules.

The microstructural evolution in the hydrogenated CP-Ti samples was investigated. There was no grain growth and no hydrides were formed in the samples hydrogenated at room temperature and 450 °C. Grain growth occurs by diffusion when temperature is high enough and time long enough. This implies that room temperature and 450 °C, as well as hydrogenation time of 3 hours are not high enough to cause grain growth. The absence of hydride formation at room temperature and 450 °C can be explained by the fact that no sufficient absorption of hydrogen occurred at these temperatures. Annealing at high temperatures (550 °C and 650 °C) lead to increase in the grain size. These results agree with the results of Gil et al [4.12]. After hydrogenation at 550 °C and 650 °C hydrogen lowered the β-transus temperature and α-β transformation occurred. During cooling from the β-phase, the α lathes were formed.

The δ-TiH$_2$ were detected by XRD in the samples hydrogenated at 550 °C and 650 °C. Hydrogen diffuse in CP-Ti and form a solid solution called α-phase when concentration of hydrogen is less than 0.12 at.%. With increase in the amount of hydrogen absorbed, hydride phase starts to form.

The δ- hydride forms in a mixture with α- phase up to 57 at.% H [4.6]. The results obtained in this study show that 45.65 and 37.53 at.% of hydrogen was absorbed at 550 °C and 650 °C, and thus hydride formation was expected.

4.2.8   Conclusion

The effects of hydrogenation on hydrogen storage capacity, the microstructure and phase transformation in CP-Ti samples as a function of temperature were investigated in this study. The results showed that hydrogen absorption was enhanced at hydrogenation temperature of 550 °C, while higher temperature of 650 °C caused a decrease in the amount of hydrogen. Hydrogenation of CP-Ti at elevated temperatures (550 °C and 650 °C) leads to formation of δ-TiH$_2$. Hydride formation did not take place after hydrogenation at room temperature and 450 °C.

The microstructure of CP-Ti was found to be dependent on the hydrogenation temperature. There was no change in the microstructure of the samples hydrogenated at room temperature and 450 °C. Hydrogen absorption at 550 °C and 650 °C caused formation of needle-like microstructure. The effect of annealing temperature on the microstructure of Ti was also investigated at high temperatures. The grain size increased to 80 μm and 100 μm at 550 °C and 650 °C, respectively. Under the experimental conditions used in this study (pressure $=$ 1 bar, hydrogen gas concentration $=$ 15%, and time of exposure to hydrogen environment$=$ 3 hours), the maximum amount of hydrogen stored in CP-Ti was found at 550 °C as quantified by both ERDA and gravimetric method to a value of approximately 46 at.%.

4.3 Hydrogen storage in Ti6Al4V

In order to compare the hydrogen storage capacities in different metallic systems used in this study, Ti6Al4V alloy was investigated under the same hydrogen conditions as described in previous sections for the commercially pure titanium (CP-Ti).

4.3.1 ERDA

Figure 4.11 shows ERDA spectrum of Ti6Al4V alloy before hydrogenation. The signal around channel number 800-900 is a result of hydrogen atoms recoiled from the surface (surface hydrogen), whereas the signal at lower channel number corresponds to recoiled hydrogen from deeper levels in the material (bulk hydrogen). The average hydrogen concentration in the as received sample is 0.6 at.%, and was calculated using equation 5.1. The near surface hydrogen accounts for 11 at.% whereas and bulk hydrogen accounts for 0.27 at.%. Hydrogen on the surface is due to sample preparation, where the surface can be contaminated with hydrocarbons and water vapor.
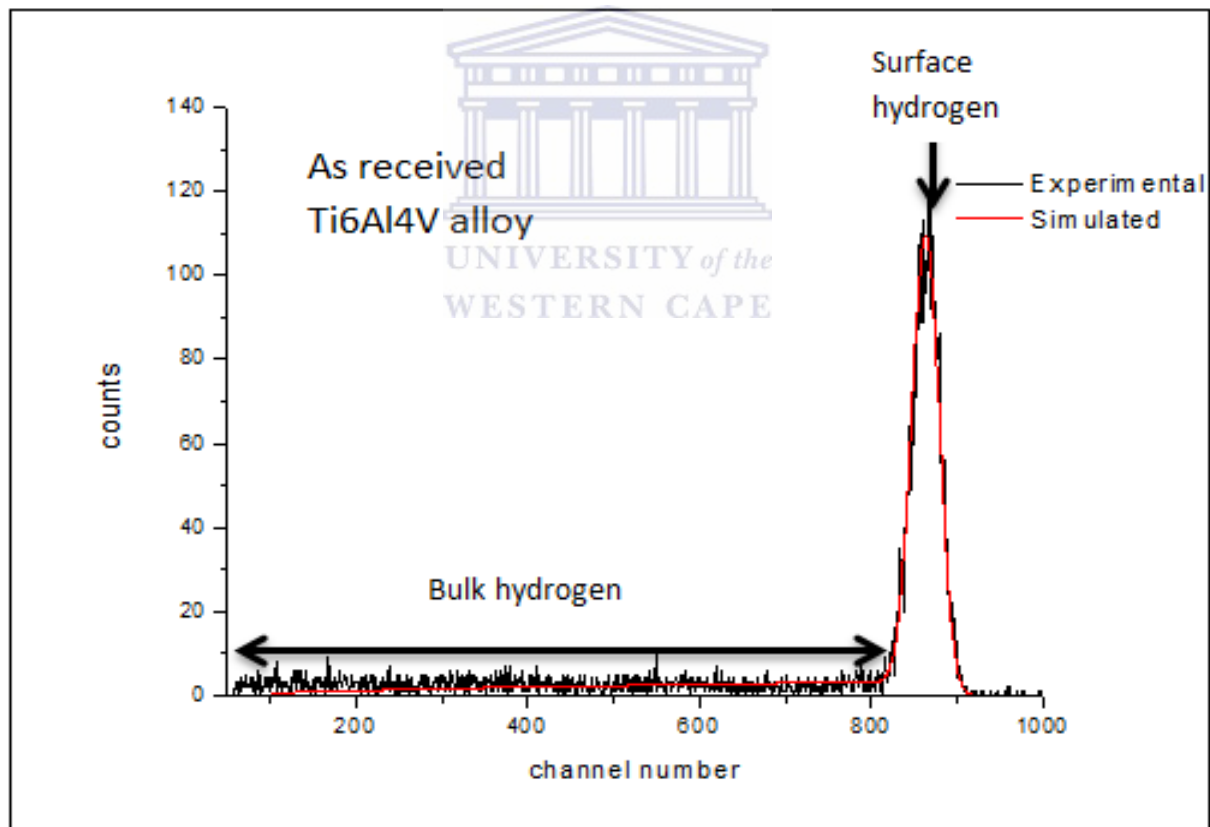
Figure 4.11: ERDA spectra of Ti6Al4V alloy before hydrogenation showing the hydrogen in the near surface region and hydrogen absorbed by bulk material.

In Figure 4.12 ERDA hydrogen spectra of Ti6Al4V alloy hydrogenated at room temperature,

450 °C, 550 °C and 650 °C are compared. An increase in the surface hydrogen at 450 °C is observed. It can be seen that there is a huge increase in the number of hydrogen atoms recoiled from the surface and bulk of Ti6Al4 alloy sample hydrogenated at 550 °C. The concentration of hydrogen in the surface and the bulk then decreased in the sample hydrogenated at 650 °C. It is also observed that surface hydrogen peak shifted to lower angles at 550 °C, this indicates diffusion of hydrogen into the bulk material.
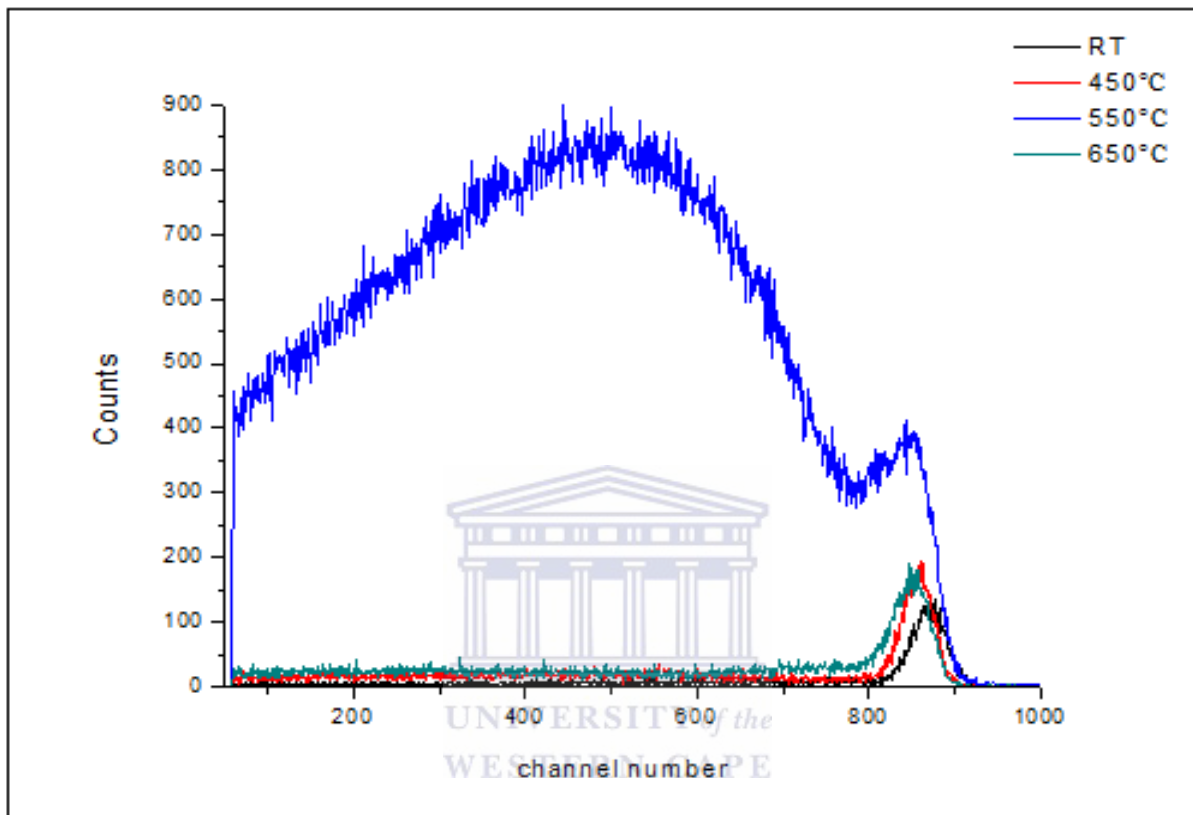
Figure 4.12: ERDA spectra of Ti6Al4V alloy hydrogenated at different temperatures for 3 hours.

The hydrogen concentration depth profiles calculated from ERDA spectra in Figure 4.12 are shown in Figure 4.13. Similarly to as received sample, the hydrogen was detected from the surface up to a depth of 0.62 μm, where the surface hydrogen peak was simulated to be around a depth 0.04 μm in room temperature hydrogenated samples. At 450 °C, the depth of hydrogen atoms in the surface region increased to 0.06 μm, whereas the average depth increased to 0.68 μm. In the samples hydrogenated at 550 °C the depth of hydrogen atoms in the surface region further increased to 0.14 μm. In the bulk region (from 0.14 μm) hydrogen concentration increased with increasing depth up to a depth of 0.4 μm. Further down, the hydrogen is then distributed uniformly up to a thickness of 0.84 μm. At 650 °C hydrogen was detected from the surface up to a depth of 0.71 μm.
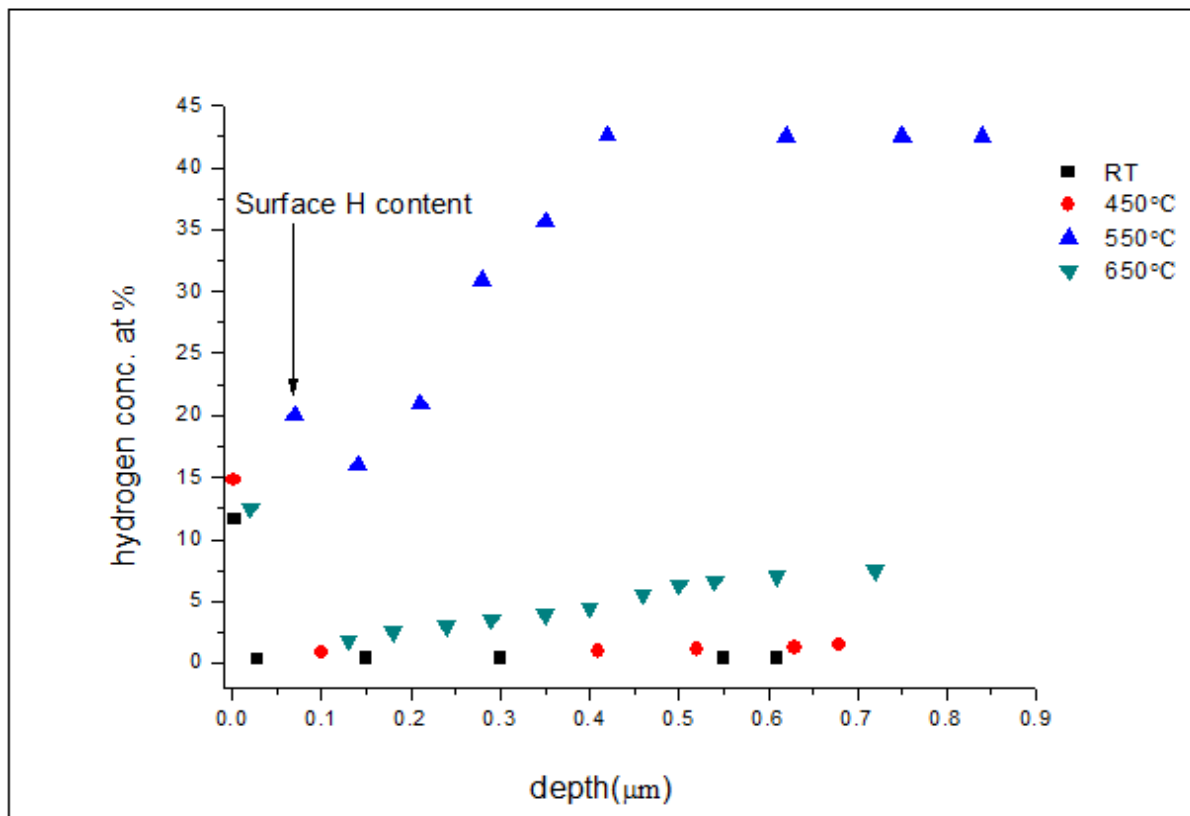
Figure 4.13: Depth profile of hydrogen in Ti6Al4V alloy as a function of hydrogenation temperature.
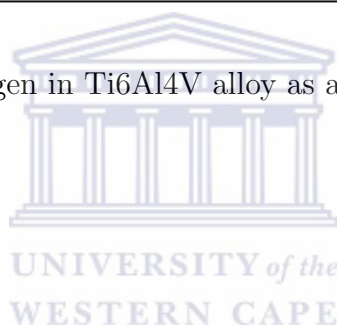
The relationship between concentration of hydrogen and hydrogenation temperature is presented Figure 4.14. At room temperature average hydrogen concentration is 1.1 at% and there is no significant change in the average hydrogen concentration at 450 °C. At 550 °C, concentration of hydrogen increased to 37.77 at.% H and then decreased drastically to 3.67 at% H at 650 °C. This decrease in the concentration of hydrogen at high temperatures might be caused by formation of thick surface oxide which prevents hydrogen absorption, and/ or decrease in solubility of hydrogen in the alloy at high temperatures or it may be caused by desorption of hydrogen from the sample due to exposure to high temperature.
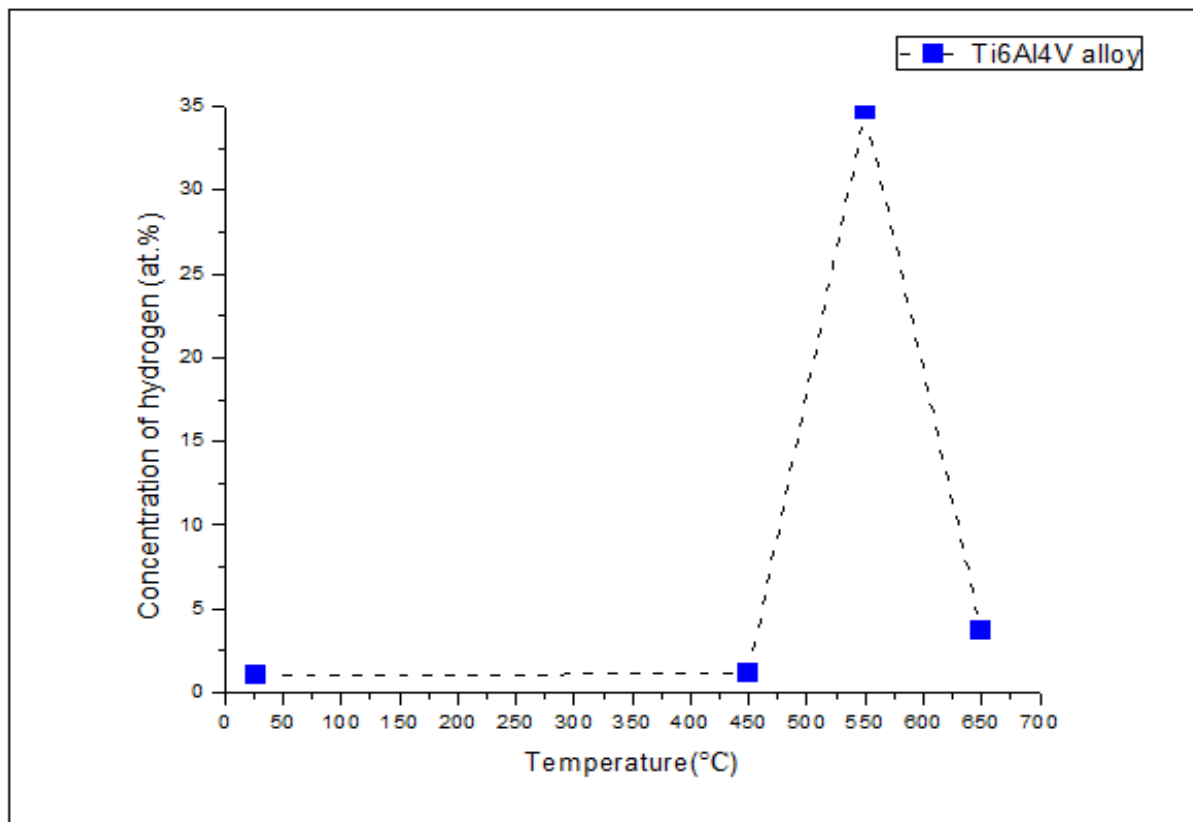
Figure 4.14: Concentration of hydrogen in Ti6Al4V alloy as a function of temperature.

4.3.2 Concentration of hydrogen in Ti6Al4V alloy determined by mass gain measurement (gravimetric method)

Table 4.4 presents the concentration of hydrogen measured by gravimetric method as a function of temperature. The amount of hydrogen absorbed at room temperature is 1.29 at.%, while after hydrogenation at $450\,°C$ amount of hydrogen increased to 9.53 at.%. The concentration of hydrogen further increased to 40.21 at.% at $550\,°C$ and then decreased to 26.52 at.% at $650\,°C$.

Table 4.4: Calculated hydrogen concentration of Ti6Al4V alloy using gravimetric method

Hydrogenation Temperature $°C$	wt%H	at%H
RT	0.03	1.29
450	0.24	9.53
550	1.46	40.21
650	0.78	26.52

The gravimetric measurements show that concentration of hydrogen in Ti6Al4V alloy is depending on hydrogenation temperature, it increases with temperature up to $550\,°C$ where more hydrogen

is absorbed and decreases at high temperatures ($650\,°C$). Concentration of hydrogen in Ti6Al4V alloy at different temperatures determined by ERDA and gravimetric method are compared in Table 4.5.

Table 4.5: Comparison between hydrogen concentration of Ti6Al4V determined by gravimetric method and ERDA.

Hydrogenation Temperature (°C)	H conc (at%H) by mass gain	H conc (at%H) by ERDA
RT	1.29	1.01
450	9.53	1.12
550	40.21	34.77
650	26.52	3.67

The comparison show that there is discrepancy between hydrogen concentration obtained by these two techniques. Concentration of hydrogen measured and calculated by mass gained is higher than the one calculated using ERDA technique. It is particularly shown for high temperature hydrogenated samples. It was suspected that the surface of the sample were oxidized due to color change after hydrogenation, as mentioned previously for CP-Ti. The effects of the oxide layer on the total mass of the sample cannot be avoided when someone use gravimetric method. Although the hydrogen concentration obtained by gravimetric method and ERDA is not the same, the trend of hydrogen absorption at $550\,°C$ and $650\,°C$ is similar.

4.3.3 Rutherford Backscattering Spectrometry (RBS)

The experimental and simulated RBS spectra of Ti6Al4V alloy are presented in Figure 4.15. The oxygen peak was observed for the sample hydrogenated from $450\,°C$ to $650\,°C$. The presence of the oxide peak indicates that the samples were oxidized during hydrogenation at elevated temperatures. The composition and thickness of oxide layers formed after hydrogenation at $450\,°C$, $550\,°C$ and $650\,°C$ are shown in Table 4.6. The oxide peak became wide with increase in hydrogenation temperature, see Table 4.6. The oxygen peaks were not observed in the as received and the sample hydrogenated at room temperature.
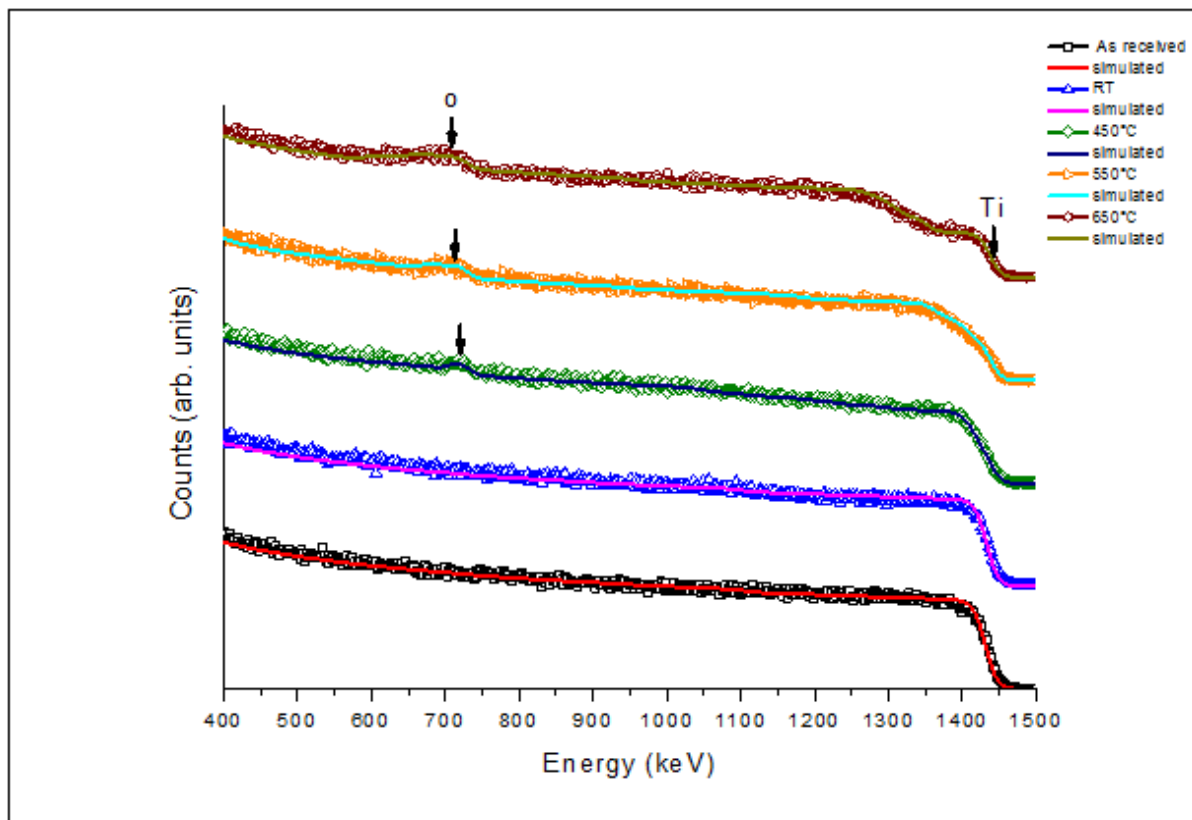
Figure 4.15: RBS spectra of Ti6Al4V alloy, before and after hydrogenation at RT, 450 °C, 550 °C and 650 °C. The hydrogenation time was 3 hours for all samples.

Table 4.6: Thickness and composition of the oxide layer of different stoichiometry formed during hydrogenation at different temperatures.

Temperature (°C)	composition (at.%)	Thickness (nm)
450	Ti = 35, O = 65	31.34
550	Ti = 33, O = 67	41.8
650	Ti = 31, O = 69	104.5

The oxide layer was incorporated due to insufficient vacuum in the system or leak in the vacuum and probably presence of oxygen gas in the system since H/Ar mixture was used during hydrogenation. The formed oxide layers during hydrogenation at high temperatures contributes to the total mass of the sample. This makes gravimetric method not a suitable method, for this type of study. It should be noted that for CP-Ti samples, the oxide layer observed at elevated temperatures was approximately 62 nm and was the same of all samples.

73

4.3.4 Microstructure of Ti6Al4V alloy

Optical microscope was used to investigate the effect hydrogen absorption on the microstructure of Ti6Al4V alloy. The micrograph in Fig 4.16 shows the microstructure of as-received Ti6Al4V alloy supplied in half annealed condition (not fully annealed). It is dual-phase alloy and consists of alpha and beta phases. The volume fraction of alpha phase is approximately 70%, determined using standard quantitative metallographic method. The depth penetration of optical microsope
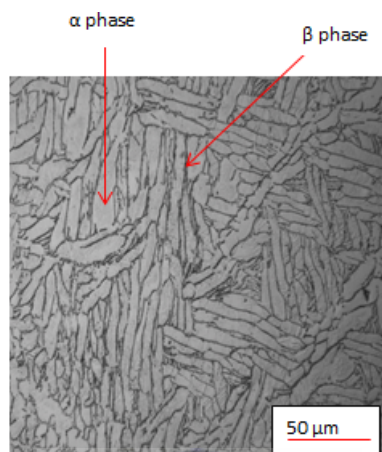
Figure 4.16: Optical micrographs of the microstructure of Ti6Al4V alloy in as-received condition. The images are taken in cross-section and arrows show the presence of α and β-phases.

is typically up 0.5 mm, depending on the type of material and microscopical analysis. In this case, microstructure is homogeneous throughout the whole cross section.

The microstructural changes caused only by thermal annealing are shown in Figures 4.17(A-B). It has been shown that annealing at 550 °C for 3 hours does not change the microstructure significantly (Figure 4.17A). However, the morphology of α-needles was slightly changed after annealing at 650 °C; they partially transformed into smaller needles and globules, as seen in Figure 4.17 B. The microstructural changes caused by hydrogenation at different temperatures were also investigated. The microstructure of Ti6Al4V samples hydrogenated at room temperature, 450 °C, 550 °C and 650 °C are shown in Figure 4.18. Samples hydrogenated at room temperature (Figure 4.18A) and 450 °C (Figure 4.18B) have similar microstructure as that of the sample before hydrogenation (only annealed at the same temperature and time). However, after hydrogenation at 550 °C (Figure 4.18C), fine needle structure was observed while the hydrogenation at 650 °C caused formation of course needles, as seen in Figure 4.18D.

In summary the microstructure of hydrogenated Ti6Al4V alloy samples depends on hydrogenation temperature. Hydrogen absorption at 550 °C and 650 °C caused formation of fine and course
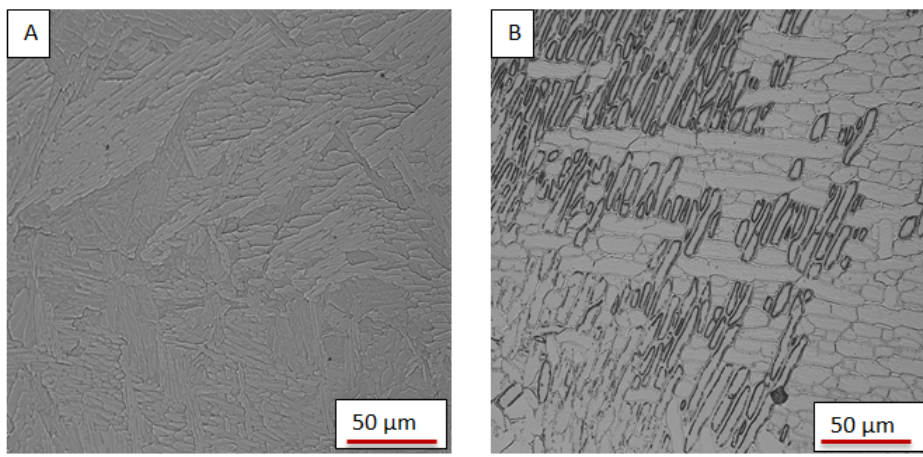
Figure 4.17: Optical micrographs of Ti6Al4V samples annealed at $550\,°C$ (A) and $650\,°C$ (B) for 3 hours. Showing the α-phase in a form of small broken needles and globules.
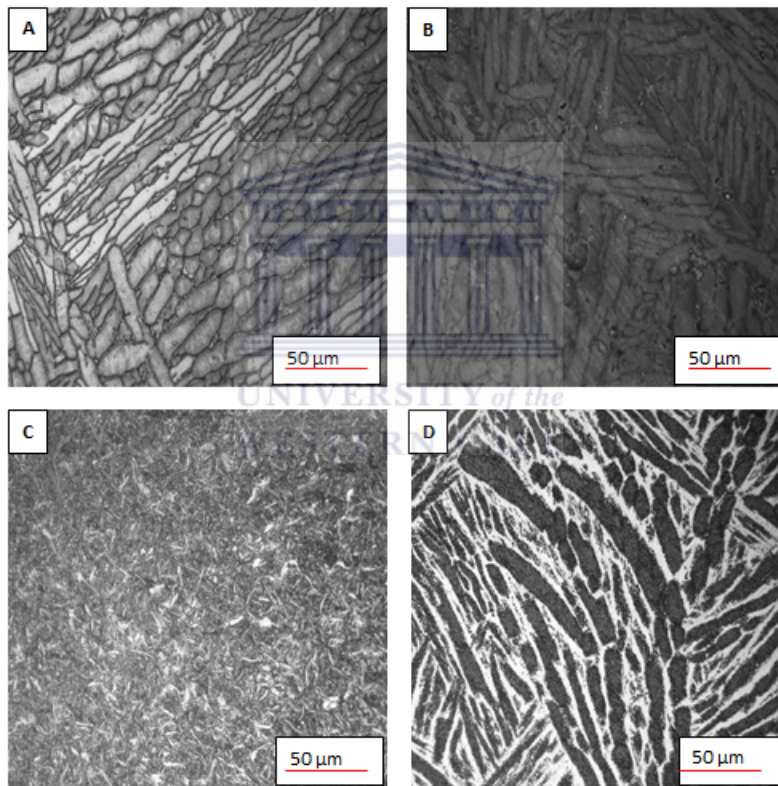
Figure 4.18: Optical microstructure of Ti6Al4V alloy: (A) hydrogenated at room temperature, (B) $450\,°C$, (C) $550\,°C$, (D) $650\,°C$ for a period of 3 hours.

needles, respectively. There was no significant changes in the microstructure of the samples hydrogenated at room temperature and $450\,°C$. Annealing at $550\,°C$ did not change the microstructure while annealing at higher temperatures ($650\,°C$) caused formation of small needles and globules.

4.3.5　Phase transformation

X-ray diffraction patterns of Ti6Al4V alloy before and after hydrogenation at different temperatures are presented in Figure 4.19. Before hydrogenation (as received) only the α-phase was detected by X-ray diffraction technique. The β-phase was not detected due to its low volume fraction. The α-phase has hexagonal close packed structure with constant a=b = 2.93 Å and c = 4.68 Å as determined by XRD. No phase change was observed in the X-ray diffraction pattern of the samples hydrogenated at room temperature and 450 °C. After hydrogenation at 550 °C the α phase and TiH_2 peaks were detected. The TiH_2 was determined to have face centered cubic structure (FCC) with lattice constant a= 4.42 Å, this value is in agreement with that reported in literature [4.13]. The ratio of Ti and hydrogen as calculated from ERDA suggests the formation of $TiH_{1.92}$ which is close to the titanium hydride phase detected by XRD. The X-ray diffraction pattern of the sample hydrogenated at temperature of 650 °C shows the presence of both α and β-phases. The α-phase with hexagonal close packed structure has lattice constant a=b = 2.95 Å and c = 4.63 Å, while the β-Ti was determined to have body centered cubic structure with lattice parameters a=b=c= 3.306 Å. The presence of β-phase in the XRD pattern of the sample hydrogenated at 650 °C shows that hydrogenation at high temperature increased the volume fraction of β-phase.
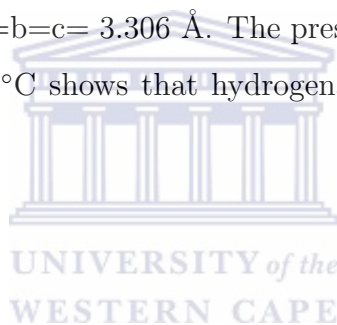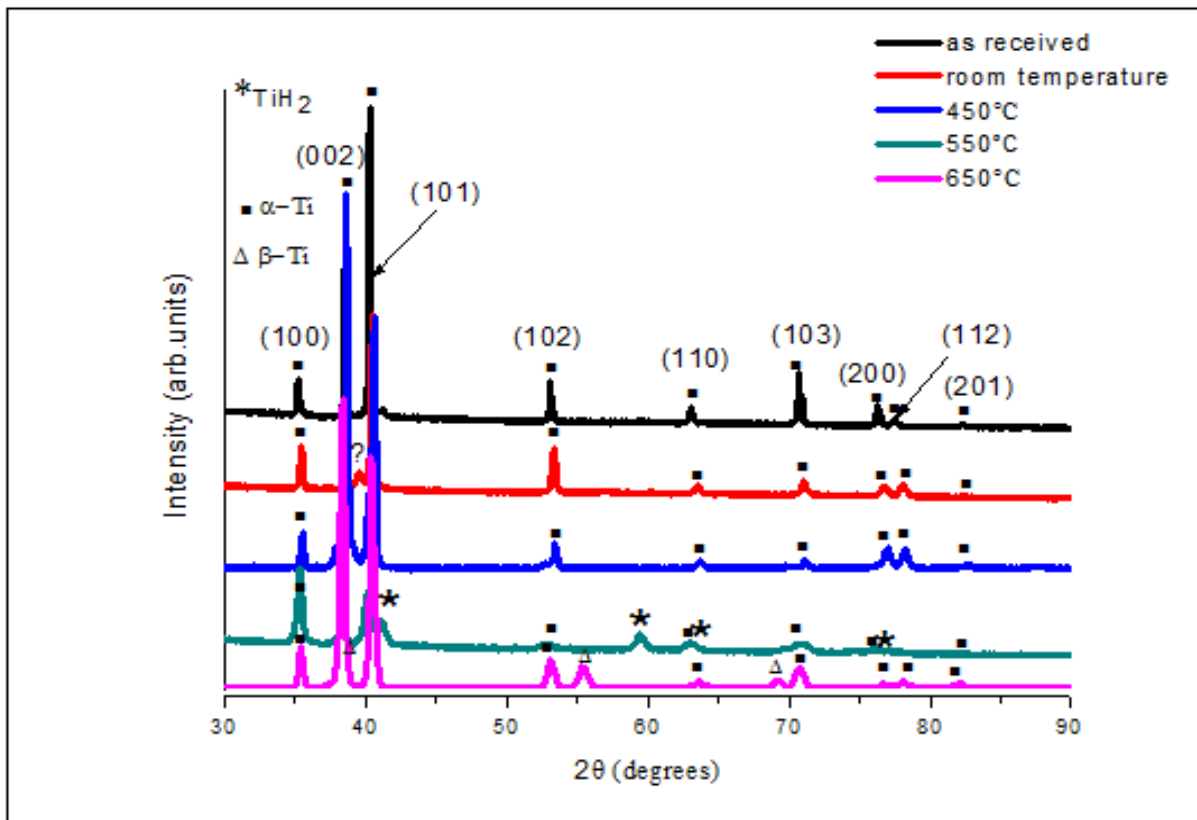
Figure 4.19: X-ray diffraction pattern of Ti6Al4V alloy: before hydrogenation, hydrogenated at room temperature, 450 °C, 550 °C and 650 °C.

In summary XRD results show that hydrogenation at room temperature, 450 °C and 650 °C did not cause formation of hydrides. At 550 °C, hydrogenation leads to formation of titanium hydrides. This means that more hydrogen was absorbed in the sample hydrogenated at 550 °C as compared to the samples hydrogenated at room temperature, 450 °C and 650 °C. XRD results agree well with the ERD findings plotted in Figure 4.14.

4.3.6 Discussion of results for Ti6Al4V alloy

The hydrogen storage capacity of Ti6Al4V alloy at different temperatures was investigated using three complimentary techniques: elastic recoil detection analysis, gravimetric method and X-ray diffraction. It was observed that concentration of hydrogen in Ti6Al4V alloy strongly depends on the hydrogenation temperature. No significant hydrogen absorption occurred at room temperature and 450 °C. The amount of hydrogen increased significantly at 550 °C and decreased at 650 °C. These results are in agreement with the results reported by Y.Zhang and S.Q. Zhang [4.8] who found that at hydrogenation temperatures above 600 °C, the concentration of hydrogen decreased as the temperature was increased. A decrease in hydrogen concentration at 650 °C is

believed to be caused by the thick oxide layer formed during hydrogenation. The oxide layer was formed at $450\,°C$, $550\,°C$ and $650\,°C$ which increased with increasing hydrogenation temperature, see Figure 4.15. The surface oxide layer prevents hydrogen to be absorbed by the material and ultimately decreases the hydrogen storage capacity in the alloy. Alternatively it can be argued that with increase in temperature, hydrogen atoms diffuse from the bulk and desorb from the surface as hydrogen molecules.

Hydrogen is a temporary alloying element to modify the microstructure of Ti6Al4V alloy [4.14]. The effect of hydrogen absorption on the microstructure of Ti6Al4V alloy at different hydrogenation temperatures were investigated. It was found that the microstructure of hydrogenated alloy strongly depends on the amount of hydrogen absorbed and temperature. After hydrogenation at room temperature and $450\,°C$ there was no significant change in microstructure, this can be explained by the fact that no significant hydrogen absorption occurred at these temperatures. During hydrogenation at $550\,°C$ fine needle like structure was formed and coarse needle structure was formed at $650\,°C$. The formation of α needles depends on the amount of hydrogen absorbed in the sample [4.7]. At $550\,°C$ addition of 34.77 at.% of hydrogen lowered the martensite start temperature, which increases with increasing hydrogen concentration. The critical cooling rate was then increased and thus resulting in the formation of fine needles.

Phase change in hydrogenated Ti6Al4V alloy at different hydrogenation temperatures has been studied using X-ray diffraction technique. During hydrogenation at room temperature and $450\,°C$ no hydrides were formed. In accordance to Qazi et al [4.15] hydride formation in Ti6Al4V alloy occurs when the amount hydrogen absorbed is greater or equal to 13 at.%. The amount of hydrogen absorbed at room temperature (1.01 at.%), $450\,°C$ (1.12 at.%) and $650\,°C$ (3.67 at.%) was not high enough to facilitate hydride formation. At low hydrogen concentration, hydrogen dissolves into the metal and form hydrogen solid solution (α_H). At hydrogenation temperatures of $550\,°C$, TiH_2 phase was detected. During hydrogenation at high temperatures, when alpha phase is saturated with hydrogen, the following reaction occurs: $\alpha \rightarrow \alpha_H + \beta_H$. During cooling of the hydrogenated Ti6Al4V alloy to a temperature below $319\,°C$, the following transformations occurs: $\alpha_H \rightarrow \alpha_H + \delta_H$ and $\beta_H \rightarrow \beta_H + \delta_H$ [4.7, 4.16]. In this study the hydrogenated samples were furnace cooled to room temperature. In the β-phase, the phase transformation $\beta_H \rightarrow \beta_H + \delta_H$ occurs when it is saturated with hydrogen. The β-phase can absorb up to 45 at.% of hydrogen [4.7].

4.3.7 Conclusion

The hydrogen storage capacity Ti6Al4V alloy at different temperatures was investigated in this work. The samples were hydrogenated at room temperature, $450\,°C$, $550\,°C$ and $650\,°C$ each for the duration of 3 hours. Hydrogenation temperature affects hydrogen absorption and the microstructure. Similarly to CP-Ti significant hydrogen absorption occurs at $550\,°C$ and decreases at $650\,°C$. The highest amount of hydrogen absorbed in Ti6Al4V alloy was 34.77 at.% at $550\,°C$.

The microstructure of hydrogenated samples was investigated and fine needle-like structure was observed in the sample hydrogenated at $550\,°C$. With increase in temperature to $650\,°C$ coarse needle-like structures were observed. XRD results showed that the δ-titanium hydride formed at hydrogenation temperature of $550\,°C$. No hydrides were formed at room temperature hydrogenation and hydrogenation at $450\,°C$ and $650\,°C$.

4.4 Hydrogen storage capacity of Ti6Al4V alloy coated with a thin layer of Pd

4.4.1 Introduction

In order to investigate the hydrogen absorption in bulk materials and coated systems, the Ti6Al4V alloy was coated with a thin layer of palladium and subjected to hydrogen atmosphere from RT to $650\,°C$ for 3 hours. Pd/Ti6Al4V samples were characterized using a variety of techniques such as ERDA, HRSEM/EDS, RBS and XRD.

4.4.2 Elastic recoil detection analysis

Figure 4.20 shows hydrogen profile of Ti6Al4V alloy coated with Pd after hydrogenation at room temperature, 450, 550 and $650\,°C$ for 3 hours. Since the counts are proportional to the amount hydrogen present in the material, it can be seen that the concentration of hydrogen on the surface and bulk increases with increase in temperature up to $550\,°C$. Thereafter hydrogen concentration decreases at $650\,°C$. It is very interesting to note that there was a huge increase in the surface and bulk hydrogen concentration of the sample hydrogenated at $450\,°C$. This means that hydrogen absorption took place unlike with the uncoated samples where no significant hydrogen absorption occurred at temperatures below $550\,°C$ (please refer to Figure 4.12).
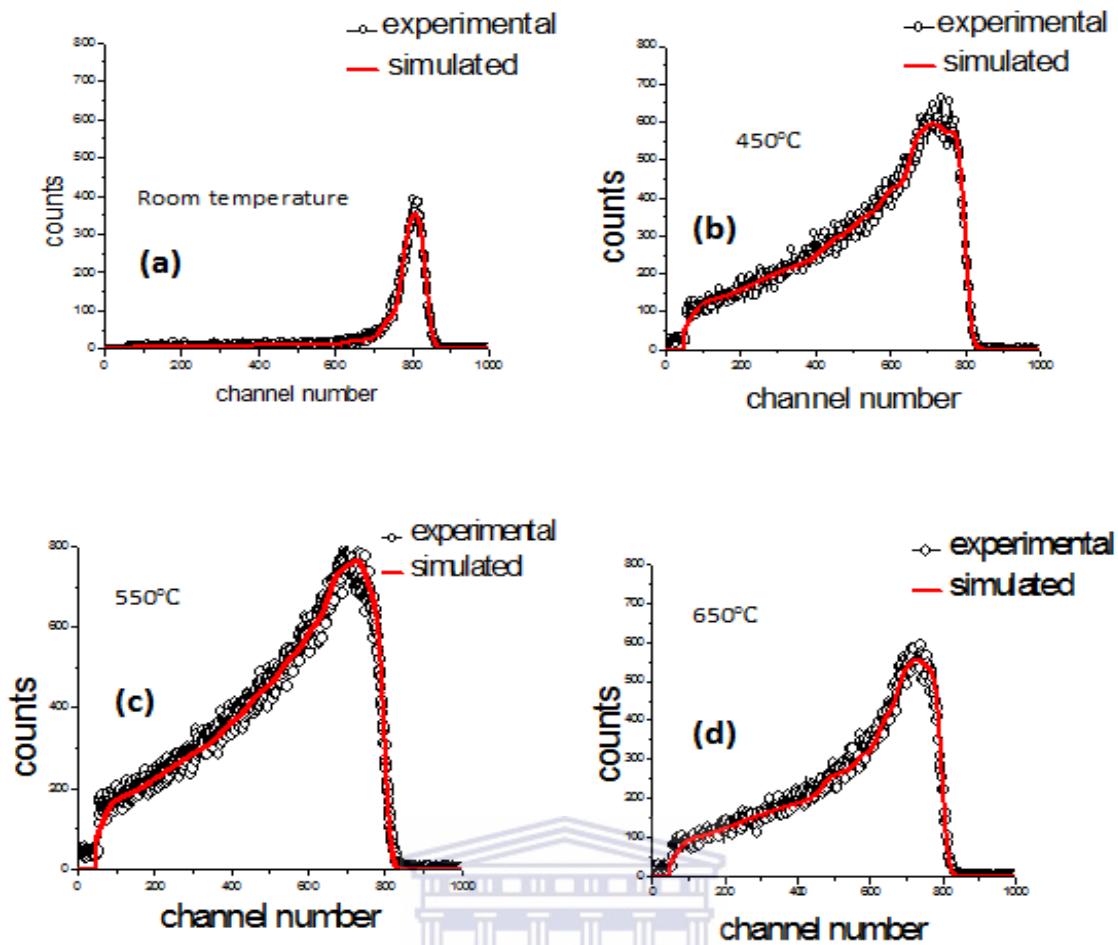
Figure 4.20: ERDA plots of Pd/Ti6Al4V coated system at various temperatures. (a) RT, (b) 450 °C, (c) 550 °C and (d) 650 °C.

The average hydrogen concentration was calculated from the simulated spectra and it is presented in Figure 4.21 as a function of temperature. At room temperature the amount of hydrogen in Pd/Ti6Al4V alloy was 4.76 at.% and increased to 30.24 at.% at 450 °C. The amount of hydrogen further increased to 36 at.% at 550 °C and then decreases down back to a concentration of 25.65 at.% at 650 °C.
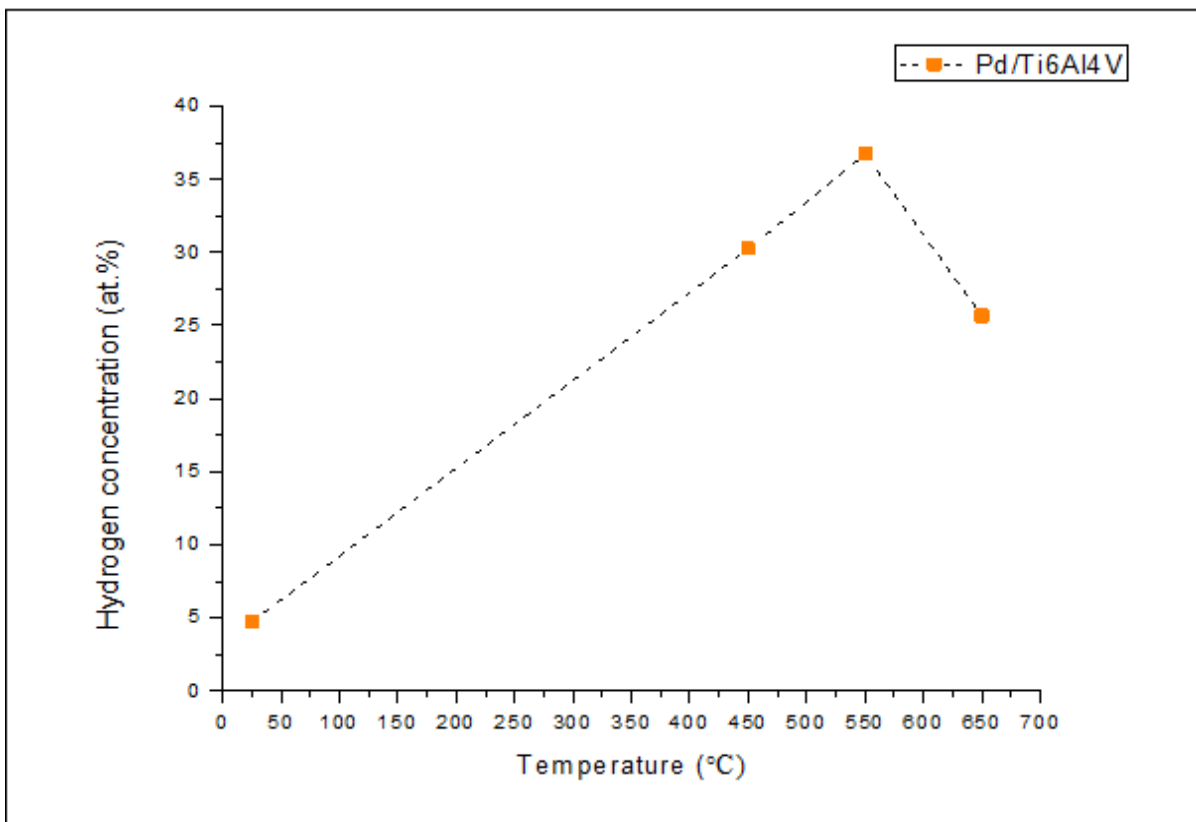
Figure 4.21: Concentration of hydrogen in Pd coated Ti6Al4V alloy as a function of hydrogenation temperature.

Depth profile of hydrogen in Pd/Ti6Al4V system obtained from ERD spectra in Figure 4.20 is shown in Figure 4.22. At room temperature hydrogen was detected from the surface down to a depth of 0.72 μm. Depth increased to 0.88 μm at 450 °C, and to 0.97 μm at 550 °C. At hydrogenation temperatures of 650 °C, hydrogen was detected from surface up to a depth of 0.83 μm. Sample hydrogenated at room temperature had less hydrogen diffused deeper into the metal as compared to samples hydrogenated at 450 °C, 550 °C and 650 °C. There is more hydrogen on the surface than in the bulk of the material.

Table 4.7: Comparison of hydrogen storage capacity in Pd/Ti6Al4V and Ti6Al4V

	Pd/Ti6Al4V		Ti6Al4V	
Temperature (°C)	at%H	depth (μm)	at%H	depth (μm)
RT	4.76	0.72	1.01	0.62
450	30.24	0.88	1.12	0.62
550	36.70	0.97	34.77	0.84
650	25.65	0.83	3.67	0.68
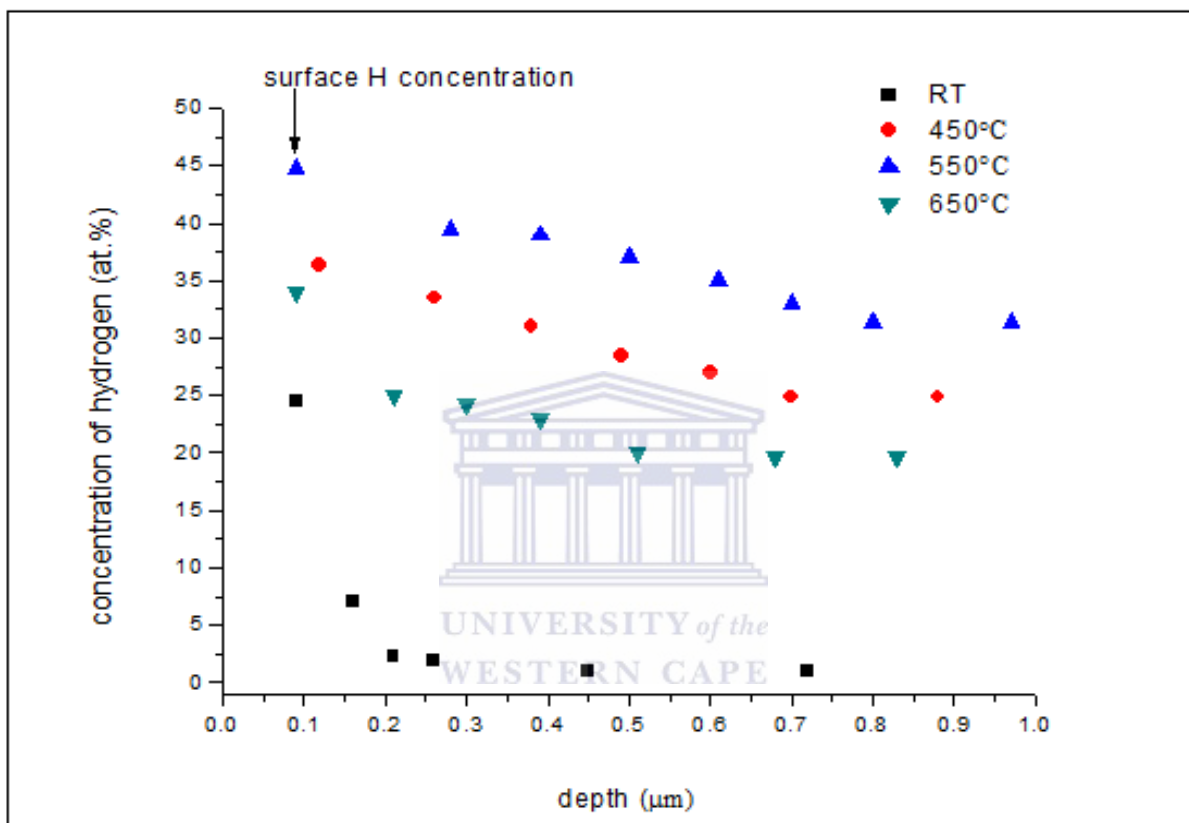
Figure 4.22: Depth profile of hydrogen in Pd/Ti6Al4V alloy.

.

The effects of temperature on hydrogen absorption of Pd coated and uncoated Ti6Al4V alloy are summarized in Table 4.7. The comparison shows that hydrogen concentration in Pd coated system is higher than that of uncoated system due to the fact that Pd layer acts a catalyst for dissociation of hydrogen molecules. In Ti6Al4V alloy, significant hydrogen absorption begins at 550 °C. However in Pd/Ti6Al4V alloy significant hydrogen absorption begins at 450 °C with 30.24 at.%H. In both Pd/Ti6Al4V and Ti6Al4V the concentration of hydrogen decreases at 650 °C.

4.4.3 High resolution scanning electron microscopy (HRSEM)

The scanning electron microscopy shows the morphology of continuous Pd layer deposited onto Ti6Al4V substrate, as illustrated in Figure 4.23. The depth of electrons was calculated using the following expression:

$$R = \frac{4120}{\rho} \times E^{(1.265-0.0954 ln E)} \; [4.17] \tag{4.1}$$

where R is the depth of electrons in microns, E is the primary electron energy in MeV and ρ is the density of Pd in $\frac{g}{cm^3}$. The penetration of electrons in Pd layer was determined to be approximately 30 nm at 5 keV.
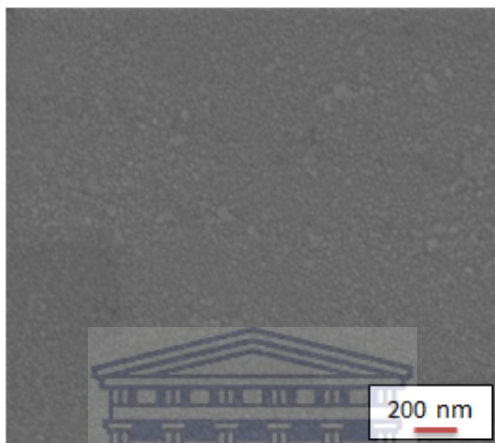
Figure 4.23: SEM micrograph of Pd coated layer (thickness of 200 nm) deposited on Ti6Al4V alloy substrate.

SEM images of Pd coated Ti6Al4V alloy after hydrogenation at different temperature are presented in Figure 4.24. The coating morphology of the sample hydrogenated at room temperature (Figure 4.24A) is not changed significantly in comparison to its as-deposited morphology (Figure 4.23) while the significant changes occurred in the samples hydrogenated at elevated temperatures. At 450 °C (Figure 4.24B), the coating became discontinuous indicating the consumption of Pd by reaction with substrate material and possible reaction with hydrogen. The formation of islands and cubic like structures were observed after hydrogenation at 550 °C (Figure 4.24C). After hydrogenation at even higher temperature (650 °C/ 3 hours), the coating morphology showed smoother appearance probably due to growth of cubic crystals (Figure 4.24D).

In order to understand the changes in coating morphology, the RBS and XRD measurements were performed.
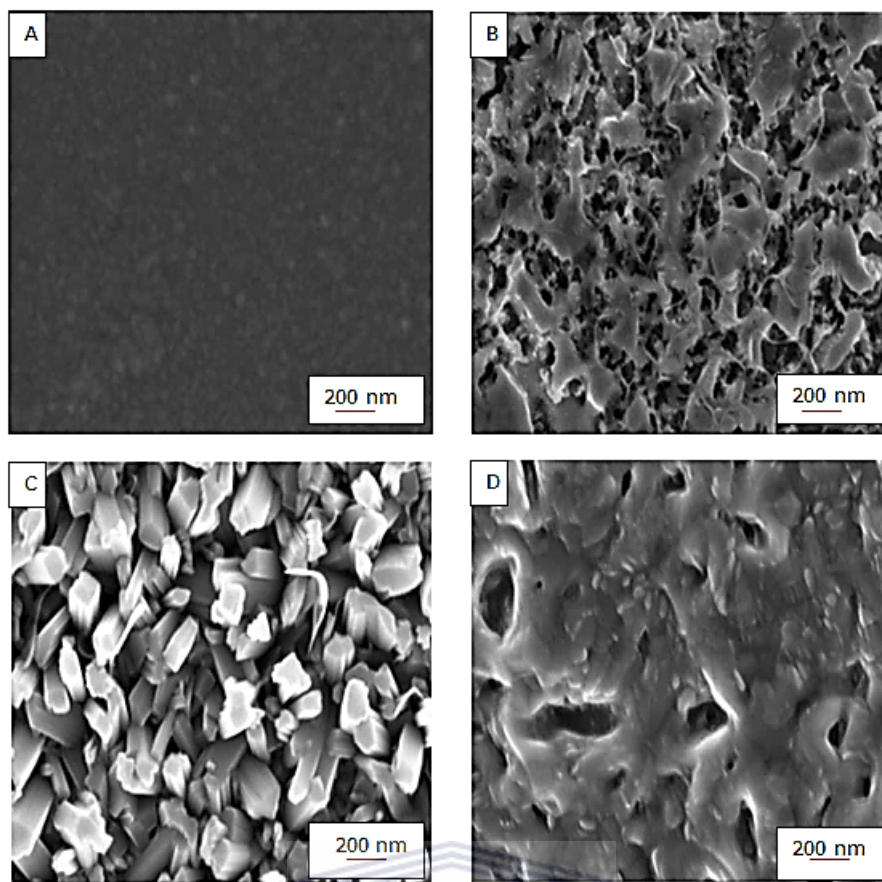
Figure 4.24: Morphology of Pd/Ti6Al4V system hydrogenated at room temperature, 450 °C, 550 °C and 650 °C for a period of 3 hours.

4.4.4 Rutherford Backscattering Spectrometry

RBS was used to determine the changes in Pd coating thickness and its stoichiometry caused by high temperature hydrogenation process. Experimental and simulated RBS spectra of Pd/Ti6Al4V system, Figure 4.25, shows the thickness of Pd layer of 204 nm which is in good agreement with thickness measured by quartz crystal (201 nm). The RBS results also show that no reaction occurred during coating deposition of Pd on Ti6Al4V substrate. The thickness of Pd layer deposited on Ti6Al4V alloy was approximately 200 nm in all samples used in this study.

Figure 4.26 shows RBS spectra of Pd coated Ti6Al4V alloy after hydrogenation. There is no significant change in the RBS spectra of Pd/Ti6Al4V hydrogenated at room temperature and 450 °C in comparison to the as-deposited sample (Figure 4.25). As opposed to the RBS spectrum of uncoated Ti6Al4V alloy, the oxygen peak was not detected after hydrogenation at 450 °C. This shows Pd layer protected the Ti6Al4V alloy against oxidation at 450 °C . After hydrogenation at 550 °C and 650 °C there was a significant change in the RBS spectrum due to reaction between coating and substrate materials.

84
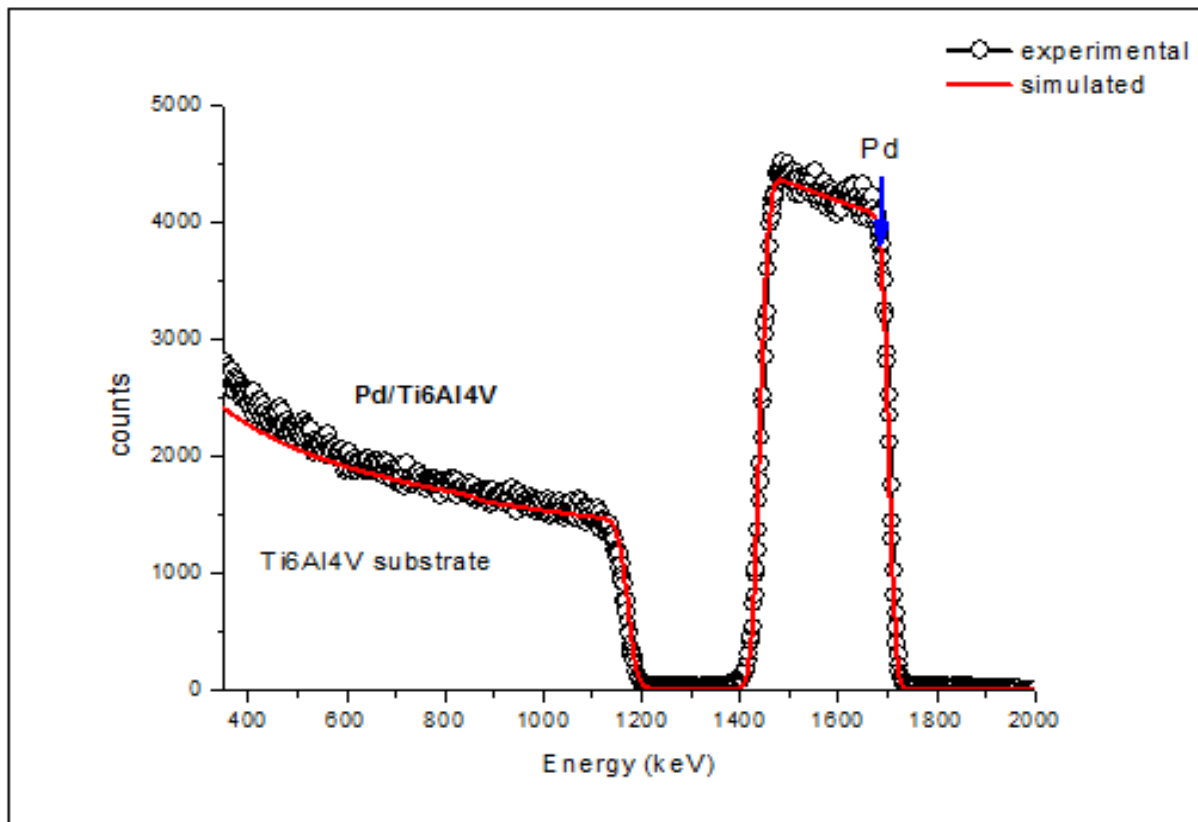
Figure 4.25: RBS spectra Pd film with thickness of 200 nm deposited on Ti6Al4V, the arrow indicate Pd edge.

The RBS spectrum of Pd/Ti6Al4V alloy after hydrogenation at 550 °C can be divided into 3 regions, the first region (1) is the near surface region only a small amount of Pd was detected (2.51 at.%). In region 2 concentration of Pd increased to 11.75 at.% and then decreased (region 3) where the concentration of Pd was 3.55 at%. Similarly RBS spectra of the sample hydrogenated at 650 °C can be divided into three different regions, on the surface (region 1) amount of Pd detected was 1.43 at%, in region 2 about 3 at.% of Pd was detected. In region 3 concentration of Pd increased to 17.58 at.%. In addition, the oxygen peak was observed in the sample hydrogenated at 650 °C.
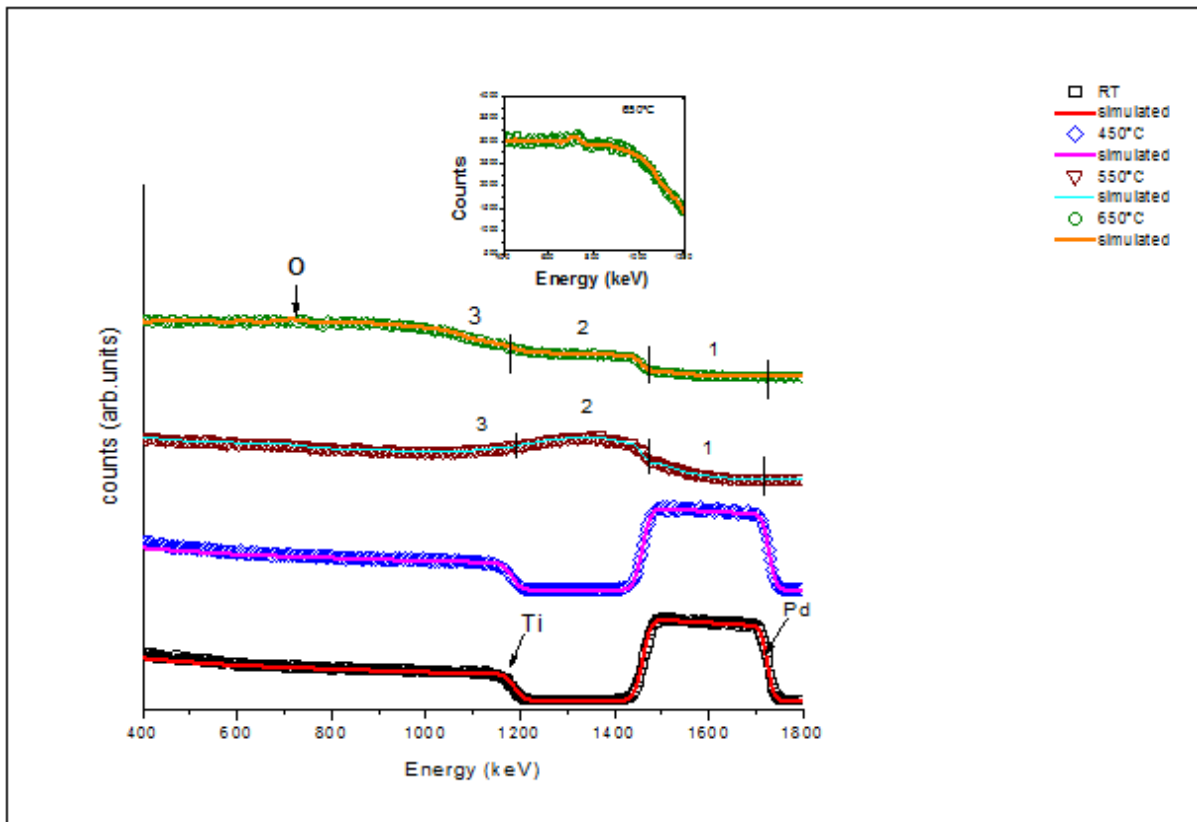
Figure 4.26: RBS spectra showing Pd coated Ti6Al4V alloy after hydrogenation at room temperature, 450 °C, 550 °C and 650 °C. The numbers indicate the regions relative to Pd concentration.

In summary, the variation in Pd concentration after hydrogenation at 550 °C and 650 °C indicate diffusion of Pd into the substrate material. In order to investigate the formation of phases, the X-ray diffraction experiments were performed.

4.4.5   X-ray diffraction

The X-ray diffraction of Pd/Ti6Al4V before hydrogenation (as deposited) and after hydrogenation at different temperature is shown in Figure 4.27. Palladium peaks and α-Ti peaks in the as deposited samples are observed as expected. After hydrogenation at room temperature the XRD pattern remained unchanged. At 450 °C in addition to the Pd and Ti peaks, the hydride peaks were identified, TiH_2 and $TiH_{1.924}$. It was also observed that the peaks shifted to lower diffraction angles indicating the presence of compressed stress in the material. When hydrogen is absorbed into the material, the formation of hydrides induces stress at the grain boundaries [4.18]. XRD pattern of Pd/Ti6Al4V after hydrogenation at 550 °C shows the presence of α-Ti, TiH_2, Pd_3Ti and Pd_5Ti_3 phases. The Pd peaks were not observed at 550 °C and 650 °C and it is an indication that Pd was consumed by reaction with substrate material. This result is in agreement with RBS

86

results which showed diffusion of Pd into the Ti6Al4V substrate. XRD pattern of the sample hydrogenated at 650 °C exhibited peaks corresponding to TiO, α-Ti and Ti_2Pd_3. In addition, at high temperatures (550 °C and 650 °C) XRD pattern shows evidence of reaction between Pd and Ti which lead to the formation of Pd_3Ti and Pd_5Ti_3 at 550 °C and Ti_2Pd_3 at 650 °C.
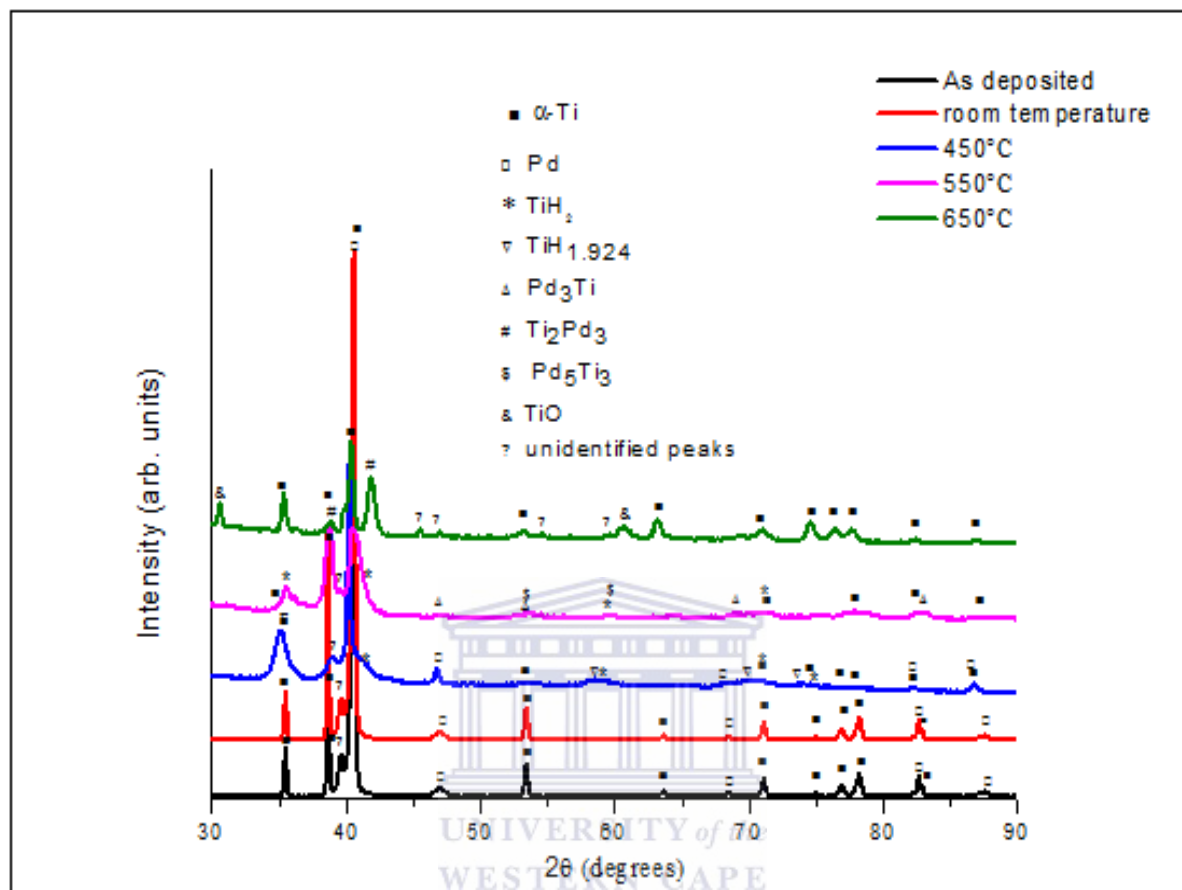
Figure 4.27: XRD patterns of Pd/Ti6Al4V before hydrogenation and after hydrogenation at room temperature, 450 °C, 550 °C and 650 °C.

In summary XRD results indicate that hydrogenation at 450 °C and 550 °C leads to formation of titanium hydrides. At room temperature and higher temperature of 650 °C hydride formation did not take place. After hydrogenation at high temperatures, alloying of Pd layer with Ti in the form of Pd_5Ti_3, Pd_3Ti at 550 °C and in the form of Ti_2Pd_3 at 650 °C was observed.

4.4.6   Discussions of results on Pd coated Ti6Al4V alloy

In the previous section it was shown that significant hydrogen uptake in CP-Ti and Ti6Al4V alloy begins at temperatures of 550 °C. No significant amount of hydrogen was observed at temperatures below 550 °C. The metal surface of the hydrogen storage materials needs to be activated

before they can absorb hydrogen. This can be achieved by hydrogenating at high temperature and pressure or by coating the surface with a catalytic layer. In this work Ti6Al4V alloy samples were coated with thin layer of Pd . The hydrogen storage capacity of Pd/Ti6Al4V at different temperatures was investigated using ERDA. The results showed that concentration of hydrogen in Pd/Ti6Al4V alloy is temperature dependent. The concentration increases with increasing temperature up to $550\,°C$ and decreases at high temperatures ($650\,°C$). The hydrogen absorption trend in Pd coated Ti6Al4V alloy samples is similar to that of uncoated Ti6Al4V but the difference is in the amount of hydrogen absorbed. The hydrogen storage capacity of Pd coated and uncoated Ti6Al4V alloy at different temperatures were compared in Table 4.7 (page 79). It was found that Pd coated Ti6Al4V alloy absorbs more hydrogen than the uncoated Ti6Al4V alloy samples. It can be concluded hydrogen Pd layer improved the hydrogen storage capacity of Ti6Al4V alloy. Significant hydrogen absorption took place at lower temperature ($450\,°C$) in Pd coated Ti6Al4V alloy in comparison to the uncoated Ti6Al4V alloy samples. This shows that Pd layer lowers hydrogen absorption start temperature in Ti. These observations agree with the observations of Shugard et al [4.19]. The authors showed that 180 nm Pd layer deposited on Ti allows hydrogen absorption at low temperatures. The maximum depth of hydrogen diffusion in Pd/Ti6Al4V alloy was greater than that of Ti6Al4V. Pd promotes dissociation of hydrogen molecules onto the Ti surface and hydrogen atoms diffuse easily in the bulk of the metal.

According to RBS results the oxygen peak was not detected in Pd/Ti6Al4V alloy samples hydrogenated at room temperature, $450\,°C$ and $550\,°C$. It should be noted that in the uncoated Ti6Al4V alloy thick oxide layer was formed after hydrogenation at $450\,°C$ and $550\,°C$. This implies that Pd protected Ti6Al4V alloy samples against oxidation during hydrogenation at $450\,°C$) and $550\,°C$. At $650\,°C$ Ti6Al4V alloy was oxidized. Heller et al [4.20] reported on the effect of Pd as a protective layer against oxidation, and it was shown that with increase in temperature thicker layer is required to prevent oxidation of Ti. It can be concluded that at 200 nm layer was not thick enough to prevent surface oxidation in Ti6Al4V alloy hydrogenated at $650\,°C$.

After hydrogenation at room temperature no hydride formation occurred. TiH_2 were formed at $450\,°C$ and $550\,°C$. Pd coating lowered hydride formation temperature in Ti6Al4V alloy to $450\,°C$, which was $550\,°C$ in the case of uncoated Ti6Al4V. alloy. Hydrogenation at high temperatures of $650\,°C$, did not lead to formation of hydrides. High temperature hydrogenation caused Pd layer to diffuse into the Ti6Al4V alloy substrate, as a result Pd_3Ti and Pd_5Ti_3 at $550\,°C$ and

Ti$_2$Pd$_3$ at 650 °C were formed.

4.4.7 Conclusion

It was observed that hydrogen absorption in Pd/Ti6Al4V alloy samples is temperature dependent. The amount of hydrogen increased with increasing temperature up to 550 °C and decreased at higher temperature of 650 °C. At room temperature Pd protects the surface against oxidation and dissociates hydrogen atoms into the surface. Generally at high temperatures Pd protects the surface against oxidation and Pd is incorporated on Ti, forming different phases. The increase in hydrogen at 450 °C and 550 °C is caused by formation of hydrides, whereas at the concentration of hydrogen decreased and hydrides are not formed. Comparing Ti6Al4V alloys with and without Pd coating on the surface, it shows significantly that low hydrogen content was absorbed, indicating the effect of Pd on dissociation of hydrogen. The maximum amount of hydrogen (36.71 at.%) was absorbed at 550 °C. Increased hydrogen storage capacity and lower hydride formation start temperature was found in Pd coated alloy in comparison to the uncoated Ti6Al4V alloy samples. Pd layer also acts as a protective layer against oxidation in Ti6Al4V alloy. Hydride formation did not occur in Pd/Ti6Al4V when hydrogenation was carried out at room temperature and 650 °C. TiH$_{1.92}$ and TiH$_2$ were formed in the samples hydrogenated at 450 °C, while only the TiH$_2$ was observed in the sample hydrogenated at 550 °C.
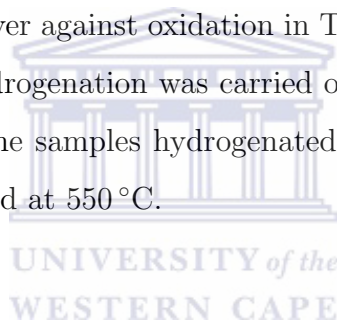
References

[4.1] B. Fenf, J. Wrng, B.C. Yang, J.Y. Chen, J.Z. Zhao, L. He, S.K. Qi, X.D. Zhang, Surface characterization of titanium and adsoption of bovine serum albumin, *Materials Characterization*, **49**, 129-137 (2003).

[4.2] E. Gemelli, N.H.A. Camargo, Oxidation kinetics of commercially pure titanium, *Revista Matéria*, **12**, 525-531 (2007).

[4.3] D. Velten, V. Biehl, F. Aubertin, B. Valeske, W. Possart, J. Breme, Preparation of TiO2 layers on CP-Ti and Ti6Al4V by thermal and anodic oxidation and by sol-gel coating techniques and their characterization, *Journal of Biomedical Materials Research*, **59**, 18-28 (2002).

[4.4] T.Yoneyama, S. Mayazaki, Editors, *Shape memory alloys for biomedical applications*, Woodhead Publishing Limited (2009).

[4.5] J.C. Rivière, S. Myhra, Editors, *Handbook of surface and interface analysis: methods for problem-solving*, *CRC press (2009)*.

[4.6] A. San-Martin, F.D. Manchester, The H-Ti (Hydrogen-Titanium) system, *Bulletin of Alloy Phase Diagrams*, **8**, 30-42 (1987).

[4.7] D.B. Shan, Y.Y. Zong, T.F. Lu, Y. Lv, Microstructural evolution and formation mechanism of FCC titanium hydride in Ti–6Al–4V–xH alloys, *Journal of Alloys and Compounds*, **427**, 229-234 (2007).

[4.8] Y. Zhang, S.Q. Zhang, Hydrogenation Characteristics of Ti-6Al4V cast alloy and its microstructural modification by hydrogen treatment, *International Journal of Hydrogen Energy*, **22**, 161-168 (1997).

[4.9] A. Lopez-Suarez, J. Rickards, R.Trejo-Luna, Analysis of hydrogen absorption by Ti and Ti-6Al-4V using the ERDA technique, *International Journal of Hydrogen Energy*, **28**, 1107-1113 (2003).

[4.10] A. Murzinova, Effect of hydrogen on microstructure of α-Ti alloys deformed at 600 °C, *Letters on Materials*, **4**, 214-217 (2014).

[4.11] S. Markelj, I. Čadež, P. Pelicon and Z. Rupnik, Studying processes of hydrogen interaction with metallic surfaces in situ and in real-time by ERDA, *Nuclear Instruments and Methods in Physics Research Section B: Beam Interactions with Materials and Atoms*, **259**, 989-996 (2007).

[4.12] F.X. Gil, D. Rodriguez, J.A. Planell, Grain growth kinetics of pure titanium, *Scripta Metallurgica et Materialla*, **33**, 1361-1366 (1995).

[4.13] T. Zhu, M. Li, Effect of 0.770 wt % H addition on the microstructure of Ti–6Al–4V alloy and mechanism of σ-hydride formation, *Journal of Alloys and Compounds*, **481**, 480-485 (2009).

[4.14] J.I. Qazi, and O.N. Senkov, F.H. Froes, Phase transformations in the Ti-6Al-4V-H system, *The Journal of The Minerals, Metals and Materials Society* , **54**, 68 - 71 (2002).

[4.15] F.H. Froes, O.N. Senkov, J.I Qazi, Hydrogen as a temporary alloying element in titanium alloys : thermohydrogen processing, *International Materials Reviews*, **49**, 227-245 (2004),

[4.16] H.J. Liu, L. Zhou, P. Liu, Q.W. Liu, Microstructural evolution and hydride precipitation mechanism in hydrogenated Ti–6Al–4V alloy, *International Journal of Hydrogen Energy*, **34**, 9596 – 9602 (2009).

[4.17] P.J. Goodhew, F.J. Humphreys, *Electron microscopy and analysis*, Taylor and Francis (1988).

[4.18] A. López-Suárez, Influence of surface roughness on consecutively hydrogen absorption cycles in Ti–6Al–4V alloy, *International Journal of Hydrogen Energy*, **35**, 10404-10411 (2010).

[4.19] A.D. Shugard, R.T. Walters, P.V. Blarigan, Titanium tritide radioisotope heat source development: Palladium-coated titanium hydriding kinetics and tritium loading tests, *Energy Conversion and Management*, **64**, 371-377 (2012).

[4.20] E.M.B. Heller, J.F. Suyver, A.M. Vredenberg, D.O. Boerma, Oxidation and annealing of thin FeTi layers covered with Pd, *Applied Surface Science*, **150**, 227-234 (1999).

Chapter 5

Conclusions

The aim and the scope of this work were to investigate the hydrogen storage capacity of CP-Ti, Ti6Al4V alloy and Pd coated Ti6Al4V alloy (Pd/Ti6Al4V), the effects of hydrogen on the microstructure and phase transformation. Hydrogenation was carried out in a vacuum furnace under 15% H/ Ar atmosphere at a pressure of 1 bar. Samples were hydrogenated at room temperature, $450\,°C$, $550\,°C$ and $650\,°C$ each for a period of 3 hours. The concentration of hydrogen in Ti6Al4V alloy and Pd/Ti6Al4V alloy were compared to understand the effect of Pd on hydrogen storage capacity of Ti6Al4V alloy. ERDA and gravimetric method were used to determine their hydrogen storage capacity. The surface composition, the microstructure and phase analysis were studied using RBS, optical microscope, scanning electron microscopy and X-ray diffraction, respectively. The results obtained from this study were presented and discussed in chapter 4 and the following conclusions were drawn for each material under investigation:

5.1   CP-Ti

RBS results showed that the samples were oxidized during hydrogenation at $450\,°C$, $550\,°C$ and $650\,°C$ leading to the formation of TiO_2 layer with thickness of 60 nm. ERDA and gravimetric method showed that hydrogen absorption depends on hydrogenation temperature. A huge amount of hydrogen was absorbed at $550\,°C$ (45.65 at.%H) and it decreased to 37.53 at.%H at $650\,°C$ as determined by ERDA. Hydrogen absorption leads to formation of hydrides (in some cases results show formation of TiH_2) in samples hydrogenated at $550\,°C$ and $650\,°C$. No hydride formation occurred in the samples hydrogenated at room temperature and $450\,°C$. The optical microscopy results showed that at high hydrogenation temperatures ($550\,°C$ and $650\,°C$), the needle-like martensite structure was formed. Comparison was made with microstructures of

as-received and annealed samples. The microstructure of as-received samples was composed of equiaxed alpha grains which increased with increasing temperature; at 550 °C the grain size was 103 μm and increased to 108 μm at 650 °C.

5.2   Ti6Al4V alloy

Similar to CP-Ti significant hydrogen absorption began at 550 °C, and average hydrogen concentration was 34.77 at.%. After hydrogenation at 650 °C the concentration of hydrogen decreased. Hydrogen absorption at 550 °C and 650 °C caused formation of fine and course needle-like structures, respectively. Titanium hydrides were not detected in the samples hydrogenated at room temperature, 450 °C and 650 °C, however formation of TiH_2 was observed at 550 °C.

5.3   Pd/Ti6Al4V system

In Pd/Ti6Al4V significant hydrogen absorption began at lower temperatures (450 °C) as compared to Ti6Al4V alloy. The amount of hydrogen increased at 450 °C and 550 °C and decreased to 650 °C. At 450 °C the amount of hydrogen absorbed was 30.24 at.% and increased to 36.70 at.% H at 550 °C and decreased to 25.65 at.%H at 650 °C. It is shown that Pd enhances hydrogen increases hydrogen concentration in Ti6Al4V alloy and act as a protective layer against oxidation. It was found that Pd coated Ti6Al4V alloy absorbs more hydrogen that the uncoated Ti6Al4V alloy. TiH_2 phase were formed after hydrogenation at 450 °C and 550 °C. No hydride phase were detected by XRD in the samples hydrogenated at room temperature and 650 °C. Ti-Pd intermetallic phases were formed in the samples hydrogenated at 550 °C and 650 °C. $PdTi_3$ and Pd_5Ti_3 phases were observed at 550 °C, whereas Ti_2Pd_3 phase was formed at 650 °C.

Scanning electron microscopy showed that room temperature hydrogenation does not affect the coating morphology, while at high hydrogenation temperatures the morphology changed significantly. Cubic-like structures and small "islands" formed in the sample hydrogenated at 550 °C.

5.4 General conclusion

The hydrogen storage capacity of the three different systems is summarised in Table 5.1.

Table 5.1: Comparison of hydrogen storage capacity in CP-Ti, Ti6Al4V and Pd/Ti6Al4V

	CP-Ti	Ti6Al4V	Pd/Ti6Al4V
Temperature (°C)	at%H	at.%H	at%H
RT	0.19	1.01	4.76
450	0.25	1.12	30.24
550	45.65	34.77	36.70
650	37.53	3.67	25.65

In general, the comparison between the three types of materials investigated in study shows that CP-Ti absorbs more hydrogen than Pd/Ti6Al4V and Ti6Al4V alloy at high temperatures (550 °C and 650 °C). However for energy storage applications it is best for hydrogen to be absorbed at lower temperatures. Therefore based on this fact, Pd/Ti6Al4V alloy system is the best candidate for hydrogen storage, because it absorbs hydrogen and forms hydrides at lower temperature of 450 °C (no hydrogen absorption occurred in the uncoated Ti6Al4V alloy and CP-Ti samples at temperatures below 550 °C).
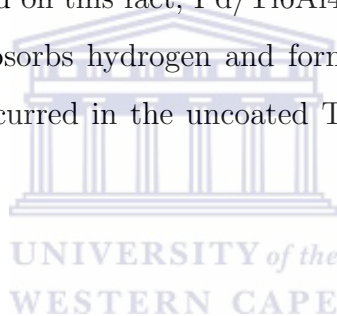
Appendix A

Thickness conversion from monolayers to nm

For TiO_2 layer with thickness of 600×10^{15}atoms/cm^2 with a density of 4.23 g/cm^3.
First find the atomic density:

$$\rho_{\text{atomic}} = \frac{\rho_{\text{mass}}(\text{g/cm}^3) \times \text{N(atoms/mol)} \times \text{a(a.u)}}{\text{Mr}} \tag{A.1}$$

Avogrado's number $N = 6.022 \times 10^{23}$ atoms/mol, number of atoms a $= 1 + 2 = 3$, molar mass Mr $= 79.866$ g/mol

$$\rho_{atomic} = \frac{(4.23\text{g/cm}^3)(3)(\text{N} = 6.022 \times 10^{23} \text{ atoms/mol})}{79.866 \text{ g/mol}} \tag{A.2}$$

$$= 9.57 \times 10^{22} \text{ atoms/cm}^3 \tag{A.3}$$

secondly find thickness Th in cm

$$Th(cm) = \frac{\text{Th(atoms/cm}^2)}{\rho_{\text{atomic}}} \tag{A.4}$$

$$= \frac{600 \times 10^{15} \text{ atoms/cm2}}{9.57 \times 10^{22} \text{ atoms/cm}^3} \tag{A.5}$$

$$= 62.69 \times 10^{-7} \text{ cm} \tag{A.6}$$

Finally convert from cm to nm :

Th(nm) $= 62.69 \times 10^{-7}$cm $\times 10^7 = 62.69$ nm

Appendix B

Detailed calculation for mass gain measurements

Suppose the mass before and after hydrogenation is m1 and m2, respectively. The change in mass after hydrogenation is given by m2-m1. As an example, for the Ti6Al4V alloy sample hydrogenated at 550, m1 = 0.471 g and m2 = 0.478 g

Table B.1: Formula used to calculate wt.% and at.% of hydrogen by gravimetric method

	Ti	Al	V	H
Molar Mass (g/mol)	47.87	26.98	50.94	1.01 (wt%)
Mass of elements (g)	(m1 * 0.9)	(m1 * 0.06)	(m1 * 0.04)	m2-m1
wt.% = (row3/sum of row 3)*100	87.5	6.25	4.16	2.08
$\frac{wt.\%}{MolarMass}$	1.83	0.23	0.08	2.06
at.% =(row 4/sum of row 4)*100	43.57	5.47	1.9	49.04

Table B.2: wt.% and at.% of hydrogen in Ti6Al4V alloy at different temperatures obtained by gravimetric method

Temperature	m1	m2	mass gain	wt.%	at.%
RT	0.8907	0.8910	0.0003	0.03	1.29
450	0.838	0.840	0.002	0.24	9.78
550	0.471	0.478	0.01	2.08	49.04
650	0.887	0.894	0.01	0.78	26.52

For CP-Ti hydrogenated at 550 °C, m1 = 0.844 and m2 = 0.858 g

Table B.3: Formula used to calculate wt.% and at.% of hydrogen in CP-Ti using mass gain

	Ti	H
Molar Mass (g/mol)	47.87	1.01 (wt%)
Mass of elements (g)	m1	m2-m1
wt.% = (row3/sum of row 3)*100	98.25	1.75
$\frac{wt.\%}{Molar\,Mass}$	2.053	1.732
at.% =(row 4/sum of row 4)*100	54.231	45.769

Table B.4: wt.% and at.% of hydrogen in CP-Ti at different temperatures obtained by gravimetric method

Temperature	m1	m2	mass gain	wt.%	at.%
RT	0.844	0.844	—	—	—
450	0.796	0.797	0.001	0.13	5.26
550	0.844	0.859	0.02	1.75	45.46
650	1.058	1.072	0.01	1.306	38.59